

An Evaluation of Turbulence Models for the Numerical Study of Forced and Natural Convective Flow in Atria

by

MATT CABLE

A thesis submitted to the Department of Mechanical and Materials Engineering in conformity with the requirements for the degree of
Master of Science (Engineering)

Queen's University
Kingston, Ontario, Canada
May 2009

Copyright © Matt Cable, 2009

Abstract

A demand for methods that can be used in the numerical analysis of three dimensional air flow in large buildings has developed as more buildings are being designed with large atriums using a solar loading that leads to complex flow. The flow in such buildings is almost always turbulent which means that turbulence models that are accurate but which do not require undue computer resources have to be selected. As a result, a numerical study of natural convective heat transfer and turbulent flows in large atria, specifically part of the Atria in the EV building at Concordia University, has been completed. Experimental work on turbulence modeling and atria design has been studied and compared with the numerical results obtained here to gain confidence in the modeling techniques used in the study. The flow has been assumed to be steady, and the Boussinesq approximation has been used. The governing equations have been numerically solved using the CFD solver FLUENT.

The three-dimensional air flow in the Concordia-like atria used the following parameters: forced flow vent inlet angle; forced flow vent velocity; date and time (for solar radiation purposes). The case with adiabatic floor and ceiling conditions was examined and compared to the case with isothermal floor and ceiling conditions. Several models were studied to compare the effect of turbulent modeling in the atria, including the following: (1) K-Epsilon; (2) K-Omega; (3) Detached Eddy Simulation (DES) model; (4) Large Eddy Simulation (LES) model. Further study was completed after it was noted the flow was completely based on natural convection when the velocity of the inlet flow was set to zero.

In addition, experimental results were available and this situation was modeled using similar parameters to the work explained above. Comparing these results supported the accuracy of the work done on the Concordia Atrium. Experimental work on the Annex 26 Atrium in Yokohama Japan was also compared to numerical results to gain confidence in techniques used in the present study and results were obtained that were in good agreement.

Acknowledgements

There are a number of people to whom I would like to express my gratitude, as they have contributed to my success.

I am greatly appreciative to my research supervisor Dr. Patrick Oosthuizen of the Department of Mechanical Engineering at Queen's University for his continuous support and generosity.

I would also like to thank Dr. M. Lightstone of McMaster University, and Dr. A. Athienitis and Patagiota Karava from Concordia University for their assistance and involvement in this project.

This work was supported by the Natural Sciences and Engineering Research Council of Canada (NSERC) through the Solar Buildings Research Network and the Department of Mechanical Engineering at Queen's University;

Many thanks to the main office staff and to Jane, Gayle and Etta;

Finally, I would like to thank my friends and family for their love and understanding.

Table of Contents

Abstract.....	i
Acknowledgements	iii
Table of Contents	iv
List of Tables	vi
List of Figures.....	vii
Nomenclature	x
Chapter 1 – Introduction.....	1
1.1 Background.....	1
1.2 Literature Review	3
1.2.1 CFD Analysis of Air Flow in Buildings.....	3
1.2.2 Ventilation and Air Flow.....	4
1.2.3 Natural Convection and Radiation	7
1.2.4 Thermal Comfort – Air Velocity.....	13
1.2.5 Thermal Comfort – Air Temperature	16
1.2.6 Turbulent Flow and Modeling Turbulence	18
1.3 Present Study	21
1.4 Methodology.....	22
Chapter 2 – Numerical Models	24
2.1 Introduction	24
2.2 Basic Model and Assumptions	24
2.2.1 Assumptions.....	24
Governing Equations.....	25
2.3 Turbulence Models.....	28
2.3.1 K-Epsilon Turbulence Model.....	32
2.3.1.1 Standard K-Epsilon Turbulence Model.....	33
2.3.1.2 RNG K-Epsilon Turbulence Model.....	35
2.3.1.3 Realizable K-Epsilon Turbulence Model	36
2.3.2 K-Omega Turbulence Model	39
2.3.2.1 Standard K-Omega Turbulence Model.....	39
2.3.2.2 SST K-Omega Turbulence Model.....	41
2.3.3 Detached Eddy Simulation (DES) Model	43
2.3.4 Large Eddy Simulation (LES) Model	46
2.4 Radiation Model	48
2.4.1 P1 Radiation Model.....	50
2.4.1.1 Solar Load Model.....	53
Chapter 3 – Computational Fluid Dynamics.....	54
3.1.1 CFD Background.....	54
3.1.2 Finite Volume Method	57
3.1.3 Solution Method.....	57
3.1.4 Discretization	61
Chapter 4 – Physical Models and Boundary Conditions.....	67
4.1.1 Atrium in EV Building, Concordia University	68
4.1.1.1 Grid Generation	69
4.1.1.2 Walls.....	77
4.1.1.3 Forced Flow Inlet and Pressure Outlet	78

4.1.1.4	Solar Loading	79
4.1.2	IEA Annex 26 Atrium.....	79
4.1.3	1m Cubic Cavity.....	82
Chapter 5	– Results and Discussions	85
5.1	Introduction	85
5.2	1m Cubic Cavity Results	85
5.2.1	Temperature and Velocity Fields	86
5.2.2	Heat Transfer at Walls.....	92
5.3	Concordia Atrium Results	93
5.3.1	Results with Different Turbulence Models	93
5.3.2	Effect of Inlet Velocity.....	96
5.3.3	Effect of Flow Inlet Angle	101
5.3.4	Natural Convection	107
5.4	Annex 26 Atrium Results	112
5.4.1	Comparing Results given by Various Turbulence Models.....	113
5.5	Summary of Results.....	114
Chapter 6	– Conclusions and Recommendations.....	117
6.1	Conclusions	117
6.2	Recommendations	120
References.....		122
Appendix A	– Further Numerical Results	126
Cubic Cavity Results		126
Concordia Results.....		132
Appendix B	- Use of FLUENT in Present Study	134
Input values for FLUENT.....		134
Concordia Atrium.....		134
1m Cubic Cavity.....		135
Annex 26 Atrium.....		136

List of Tables

Table 4-1 Mesh densities of Grids 1 to 4	70
Table 4-2 Percentage difference between horizontal temperature profiles for grids 1 to 4	73
Table 4-3 Percentage difference between horizontal velocity profiles for grids 1-4	74
Table 4-4 Percentage difference between vertical temperature profiles for grids 1-4	75
Table 4-5 Difference between vertical velocity profiles for grids 1-4	76
Table 5-1 Comparison of average Nusselt number along the hot wall median line for several turbulence models.....	92
Table 5-2 Temperature and velocity at H=1m for several turbulence models and flow situations	111
Table 5-3 Average Air Temperatures for several turbulence models	113
Table 5-4 Wall temperatures compared for several turbulence models	114
Table 0-1 Properties of Air	134
Table 0-2 Thermal and radiative properties of walls	134
Table 0-3 Thermal and radiative properties of glass wall	135
Table 0-4 Thermal properties for outer glass walls	135
Table 0-5 Thermal properties for Lexan®	135
Table 0-6 Thermal properties for walls (polyurethane)	136
Table 0-7 Thermal and radiative properties for glass walls.....	136
Table 0-8 Thermal and radiative properties for floor and north wall (polystyrene)	136

List of Figures

Figure 1-1 Example of corner atrium at entrance	2
Figure 1-2 View inside an atrium with glazed roof	2
Figure 1-3 Velocity decay along the floor at different Archimedes numbers for diffuser type B ...	5
Figure 1-4 Maximum velocity close to the floor vs. distance x	6
Figure 1-5 Length scale δ in the flow vs. distance from diffuser G (h=0.56m)	7
Figure 1-6 Schematic of heat and fluid flow paths in a cavity	8
Figure 1-7 Temperature profiles on lower and upper insulated walls for several Ra-numbers and emissivity values	9
Figure 1-8 Isotherms (a), velocity fields (b) and streamlines (c) without emissivity for Ra-numbers of 2.1×10^6 , 10^7 and 5×10^7	11
Figure 1-9 Isotherms (a), velocity fields (b) and streamlines (c) for $\varepsilon=0.5$ for Ra-numbers of 2.1×10^6 , 10^7 and 5×10^7	12
Figure 1-10 Percentage of people dissatisfied as a function of mean air velocity	14
Figure 1-11 Draft conditions dissatisfying 15% of the population	15
Figure 1-12 Percentage of seated people dissatisfied as a function of air temperature difference between head and ankles	17
Figure 2-1 Coordinate system and control volume used in present study	26
Figure 2-2 Radiative Heat Transfer	50
Figure 3-1 Flowchart of method used for CFD application	56
Figure 3-2 Overview of segregated solution method	59
Figure 3-3 Temperature Profile at mid-height in the median plane	64
Figure 3-4 Velocity Profile at mid-height in the median plane	64
Figure 3-5 Temperature Profile at mid-width in the median plane	65
Figure 3-6 Velocity Profile at mid-width in the median plane	65
Figure 4-1 Outside view of EV building at Concordia University	68
Figure 4-2 Three-Dimensional domain	69
Figure 4-3 Concordia Mesh 1 with 232,524 nodes	70
Figure 4-4 Concordia Mesh 2 with 392,877 nodes	71
Figure 4-5 Concordia Mesh 3 with 583,234 nodes	71
Figure 4-6 Concordia Mesh 4 with 1,130,395 nodes	72
Figure 4-7 Horizontal temperature profile for several grid densities	73
Figure 4-8 Horizontal velocity profile for several grid densities	74
Figure 4-9 Vertical temperature profile for several grid densities	75
Figure 4-10 Vertical velocity profile for several grid densities	76
Figure 4-11 Dimensions of Concordia Atrium	78
Figure 4-12 IEA Annex 26 Atrium, Yokohama, Japan	80
Figure 4-13 Dimensions of Annex 26 Atrium	80
Figure 4-14 Annex 26 Atrium Mesh	81
Figure 4-15 Dimensional domain of air filled cavity	82
Figure 4-16 Mesh for air-filled cavity	83
Figure 5-1 (Dimensionless) Temperature distribution on the cavity horizontal walls (from hot wall, x=0m to cold wall, x=1m)	86
Figure 5-2 Dimensionless temperature profile at mid-height in the median plane in meters	88
Figure 5-3 Dimensionless velocity profile at mid-height in the median plane in meters	89
Figure 5-4 Dimensionless temperature profile at mid-width in the median plane in meters	89

Figure 5-5 Dimensionless velocity profile at mid-width in the median plane in meters	90
Figure 5-6 Horizontal temperature profile at mid-height of the Concordia Atrium using several turbulence models.....	94
Figure 5-7 Horizontal velocity profile at mid-height of the Concordia Atrium using several turbulence models.....	95
Figure 5-8 Vertical temperature profile at center of the Concordia Atrium using several turbulence models.....	95
Figure 5-9 Vertical velocity profile at center of the Concordia Atrium using several turbulence models	96
Figure 5-10 Horizontal temperature profile in the Concordia Atrium for several inlet velocities	97
Figure 5-11 Horizontal velocity profile in the Concordia Atrium for several inlet velocities	97
Figure 5-12 Vertical temperature profile in the Concordia Atrium for several inlet velocities	98
Figure 5-13 Vertical velocity profile in the Concordia Atrium for several inlet velocities	98
Figure 5-14 Temperature contours on multiple planes in the Concordia Atrium for inlet velocities of 1, 2, 3 and 4m/s respectively	99
Figure 5-15 Velocity contours in the middle ($z=3\text{m}$) of the Concordia atrium parallel to the glazing for inlet velocities of 1, 2, 3 and 4m/s respectively	100
Figure 5-16 Temperature (K) contours on multiple planes in the Concordia atrium for inlet angles of 26, 45, 63 and 90 degrees respectively	101
Figure 5-17 Velocity contours in the middle of the Concordia atrium parallel to the glazing for inlet angles of 26, 45, 63 and 90 degrees respectively	102
Figure 5-18 Horizontal temperature profile for inlet velocity of 0.5m/s and inlet temperature of 293K.....	103
Figure 5-19 Horizontal velocity profile for inlet velocity of 0.5m/s and inlet temperature of 293K	104
Figure 5-20 Vertical temperature profile for inlet velocity of 0.5m/s and inlet temperature of 293K.....	104
Figure 5-21 Vertical velocity profile for inlet velocity of 0.5m/s and inlet temperature of 293K	105
Figure 5-22 Velocity (m/s) contour at mid width in the x-y plane for inlet velocity of 0.5m/s and inlet temperature of 293K.....	106
Figure 5-23 Temperature contour for inlet velocity of 0.5m/s and inlet temperature of 293K...	107
Figure 5-24 Horizontal temperature profile using the k-epsilon realizable model for different times of year.....	108
Figure 5-25 Horizontal velocity profile using the k-epsilon realizable model for different times of year	108
Figure 5-26 Vertical temperature profile using the k-epsilon realizable model for different times of year.....	109
Figure 5-27 Vertical velocity profile using the k-epsilon realizable model for different times of year	109
Figure 5-28 Geometry showing dashed lines where temperature and velocity profiles are calculated.....	111
Figure 5-29 Vertical Profiles for different times of year	113
Figure 0-1 Temperature profile at mid-height in the median plane	126
Figure 0-2 Temperature profile at mid-height in the median plane	127
Figure 0-3 Velocity profile at mid-width in the median plane.....	127
Figure 0-4 Temperature profile at mid-width in the median plane.....	128
Figure 0-5 Temperature profile at mid-height in the median plane	128
Figure 0-6 Velocity profile at mid-height in the median plane.....	129
Figure 0-7 Temperature profile at mid-width in the median plane	129

Figure 0-8 Velocity profile at mid-width in the median plane.....	130
Figure 0-9 Temperature profile at mid-height in the median plane	130
Figure 0-10 Velocity profile at mid-height in the median plane.....	131
Figure 0-11 Temperature profile at mid-width in the median plane.....	131
Figure 0-12 Velocity profile at mid-width in the median plane.....	132
Figure 0-13 Vertical temperature profile of Concordia atrium for four turbulence models	133
Figure 0-14 Horizontal velocity profile of Concordia atrium at height $y=1.2\text{m}$ for four turbulence models	133

Nomenclature

a	absorption coefficient
Ar	Archimedes Number
C	linear-anisotropic phase function coefficient
C_p	specific heat
d	distance
D_ω	cross diffusion term
$F_{1,2}$	blending function constant
g	gravitational acceleration
G	incident radiation
G_b	generation of turbulent kinetic energy that arises due to buoyancy
G_k	generation of turbulent kinetic energy the arises due to mean velocity gradients
Gr	Grashof number
I	radiation intensity, (energy per area of emitting surface per unit solid angle)
k	kinetic energy
k_{eff}	effective thermal conductivity
K	thermal conductivity
κ	von Karman constant
L	characteristic dimension
L_s	mixing length for subgrid scales
n	refractive coefficient
Nu	mean Nusselt number
P	pressure
\vec{r}	position vector
Re	Reynolds Number
Ra	Rayleigh Number
s	path length
\vec{s}	direction vector
\vec{s}'	scattering direction vector
S	strain rate magnitude
S	user defined constant
t	time
T	absolute temperature
Tu	turbulence intensity in percent
u	velocity component in the x direction
v	velocity component in the y direction
v_s	mean fluid velocity
\vec{v}	velocity vector
V	velocity
V_{sd}	standard deviation of the velocity from the mean
w	velocity component in the z direction

x	horizontal coordinate normal to plate
y	horizontal coordinate along plate
Y_k	dissipation of turbulent kinetic energy due to turbulence
Y_M	fluctuating dilation in compressible turbulence
z	vertical coordinate

Greek Symbols

β	thermal expansion coefficient
ρ	mass density
ρ_w	wall reflectivity
θ	temperature difference
μ	dynamic fluid viscosity
μ_t	eddy viscosity
δ_{ji}	Kronecker delta
Γ	turbulent diffusivity of heat
ϕ	scalar variable
α^*	damping coefficient
σ	Stefan-Boltzmann Constant ($5.672 \times 10^{-8} \text{ W/m}^2 \text{ -K}^4$)
σ_s	scattering coefficient
Φ	phase function
Ω'	solid angle
σ_t	turbulent Prandtl number ($\frac{\mu_t}{\Gamma}$)
ε	rate of dissipation of kinetic energy
ν	kinematic fluid viscosity ($\frac{\rho}{\mu}$)
ω	specific dissipation rate of turbulent kinetic energy, k

Chapter 1 – Introduction

1.1 Background

Air flow in buildings significantly affects comfort levels, energy efficiency and heating, cooling and ventilation effectiveness. Energy use in buildings in Canada account for approximately 30% of our total energy consumption, roughly 50% of our electricity consumption, and around 28% of our total green house gas emissions. Advancements in computational fluid dynamics (CFD) have the potential to noticeably affect building design strategies as it allows the air stratification, the heat transfer, the radiation exchange and other aspects of the building environment to be relatively easily and rapidly calculated.

The present work was motivated by the lack of information about the combination of turbulence modeling, solar radiation and natural convection in CFD building simulation. There are very few experimental or theoretical results available in the literature concerning flow simulation in atria and therefore the development of an accurate computer model is necessary in order to obtain a better understanding of energy efficient building design incorporating these aspects.

This study will specifically investigate turbulent flow in atria. An atria is defined as a large open space, often several stories high, that have glazed roof and/or large windows. It is often situated close to the main entrance offering natural and comfortable lighting (daylighting), warmth and natural air circulation. Daylighting is the use of various design techniques to enhance the use of natural light in a building. The main

problem with modeling such a large open space is in obtaining accurate results (especially in the near-wall regions) without creating excessive computational demands. Most existing atria have been designed with day-lighting, natural circulation and aesthetic consideration in mind. Atria have the potential to improve overall energy efficiency and this is a major consideration in this study. Figure 1-1 and Figure 1-2 show examples of two types of atria with glazed facades on the side walls or roof.



Figure 1-1 Example of corner atrium at entrance



Figure 1-2 View inside an atrium with glazed roof

1.2 Literature Review

When investigating the CFD analysis of airflow in atria there are several aspects that must be considered to fully evaluate the problem;

- turbulence modeling
- natural convection
- building simulation
- thermal radiation exchange
- indoor thermal comfort

Previous research related to the topic of the present study is reviewed in the following four sections.

1.2.1 CFD Analysis of Air Flow in Buildings

Because of the cost and level of expertise required to use building simulation software (such as FLUENT), computer modeling is currently not widely used in the design of buildings. This type of modeling is much more useful in research labs and universities where the results can be used to aid building design. Computation Fluid Dynamics (CFD) is the most recent and when modeled properly can be the most accurate means of predicting airflow in a building, however, not all geometries or models require it. Depending on the complexity and type of situation that is being analyzed, there are several approaches to predicting environments inside and outside buildings.

One of the first numerical investigations of air flow and heat transfer in buildings using computational fluid dynamics is described by P.V. Nielsen (1974). This study numerically modeled turbulent, recirculating flow in 2 dimensional cases using an

approach developed at Imperial College and reported by Gosman et al. (1969). Nielsen used the k-epsilon model for predicting turbulence. Air movement at low Archimedes number was calculated by essentially neglecting buoyancy. Archimedes number is a ratio of buoyancy to inertia defined by the following formula.

$$Ar = \frac{Lg\theta}{TV^2} \quad (1.1)$$

where L is the characteristic dimension, g is the gravitational acceleration, V is the velocity, T is the absolute temperature, and θ is the temperature difference. Results for velocity profiles in the room and velocity decay in the supply air jet area were compared to experimental results. The agreement achieved were considered to be acceptable.

1.2.2 Ventilation and Air Flow

Nielsen (2000) studied the effects of wall mounted air diffusers in terms of how air flow from these devices influences the thermal comfort of occupants in a room. Several types of diffusers were tested to determine the velocity and temperature distributions in a large room. The velocity at the inlet of the diffuser was measured for changes in the Archimedes number. Using one of the diffusers, the Archimedes number was altered and produced results shown in Figure 1-3.

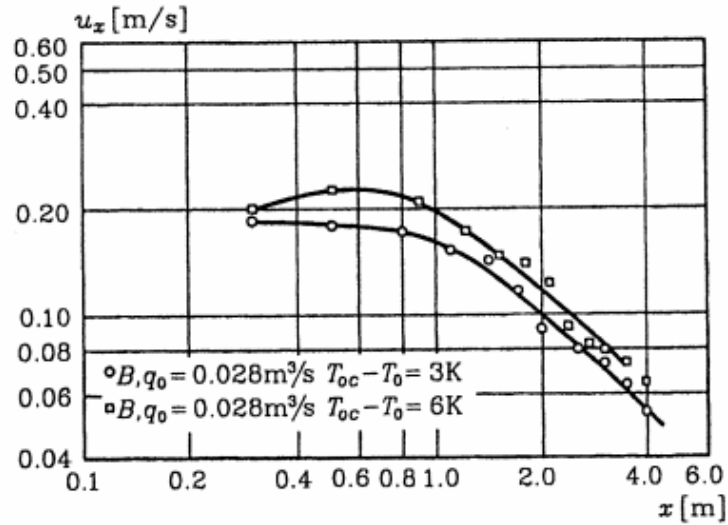


Figure 1-3 Velocity decay along the floor at different Archimedes numbers for diffuser type B

Multiple diffuser types were tested. It was observed that, for diffuser type B with flow rate $0.028\text{m}^3/\text{s}$ the velocity profiles were quite different for temperature differences of 3K and 6K suggesting that the Archimedes number can be an important parameter. The 3K difference in temperature increased the velocity from 0.1m/s to 0.12m/s at a distance of 2m from the diffuser. Nielsen also tested the effects of diffusers having different flow rates and types of flow (i.e. exit flows from different diffusers). Figure 1-4 shows the results for three diffusers with different flow orientations but similar flow rates and heat loads.

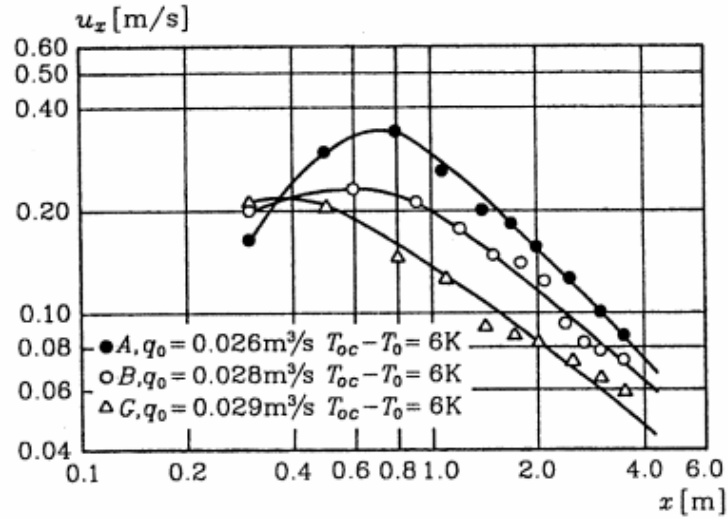


Figure 1-4 Maximum velocity close to the floor vs. distance x

Figure 1-4 shows that buoyant forces play a large role again in the velocities of flow with different Archimedes numbers shown by the difference in velocities. Nielsen found that different diffuser designs generate different velocity levels at the same flow rate and heat load. In general, it was determined from the study that the velocity at the floor is influenced by the air supply flow rate, the type of diffuser at the supply to the room, and the difference between the air supply temperature and room temperature. It was also determined that the velocity level is inversely proportional to the distance from the diffuser. This is shown by the results given in Figure 1-5 where the development of δ along the floor is plotted for several Archimedes numbers. δ is defined as the distance from the floor to the height where the velocity has a level which is half of the maximum velocity close to the floor.

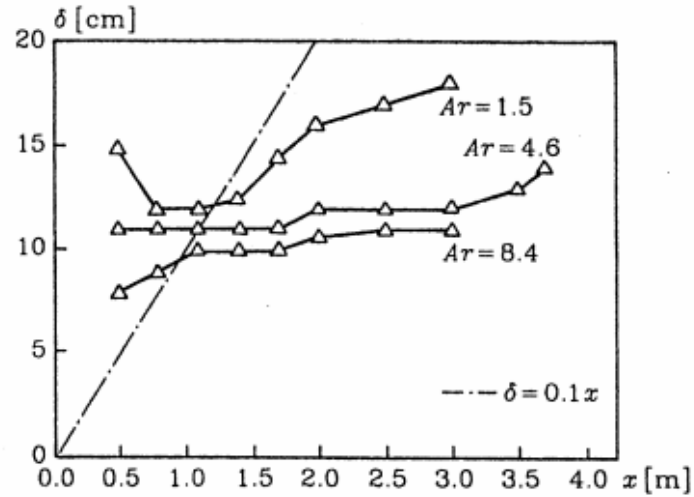


Figure 1-5 Length scale δ in the flow vs. distance from diffuser G ($h=0.56\text{m}$)

It can be seen that the height of the flow region is still much smaller than the height of the diffuser. Cold air from the diffuser moves towards the floor due to gravity before it begins to behave as stratified flow further along the floor. The length scale δ decreases as the Archimedes number is increased.

1.2.3 Natural Convection and Radiation

A numerical study of heat transfer in a 2-D square enclosure (shown in Figure 1-6) was undertaken by Jaballah et al. (2007). The effect of radiation on the flow field and temperature distribution was investigated.

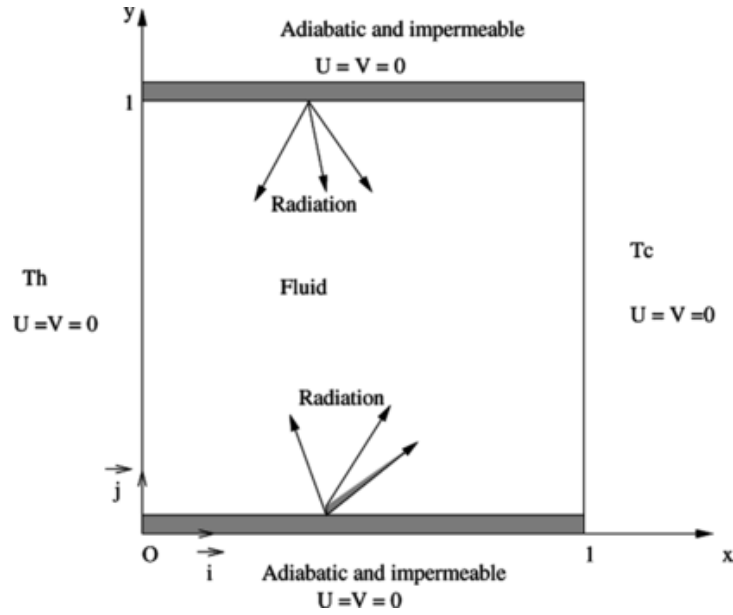


Figure 1-6 Schematic of heat and fluid flow paths in a cavity

To examine the effects of radiation on the flow field, the temperature profiles along the horizontal axis of the lower (a) and upper (b) insulated floor and ceiling were calculated. Figure 1-7 shows the profiles for Rayleigh (Ra) numbers of 10^7 and 2.1×10^6 . The Ra number for a fluid is a dimensionless number associated with buoyancy driven flow. It can be seen as a ratio of buoyancy forces and thermal and momentum diffusivities and defined by the following formula

$$Ra = Gr \times Pr = \frac{g\beta}{\nu\alpha}(T_s - T_\infty)x^3 \quad (1.2)$$

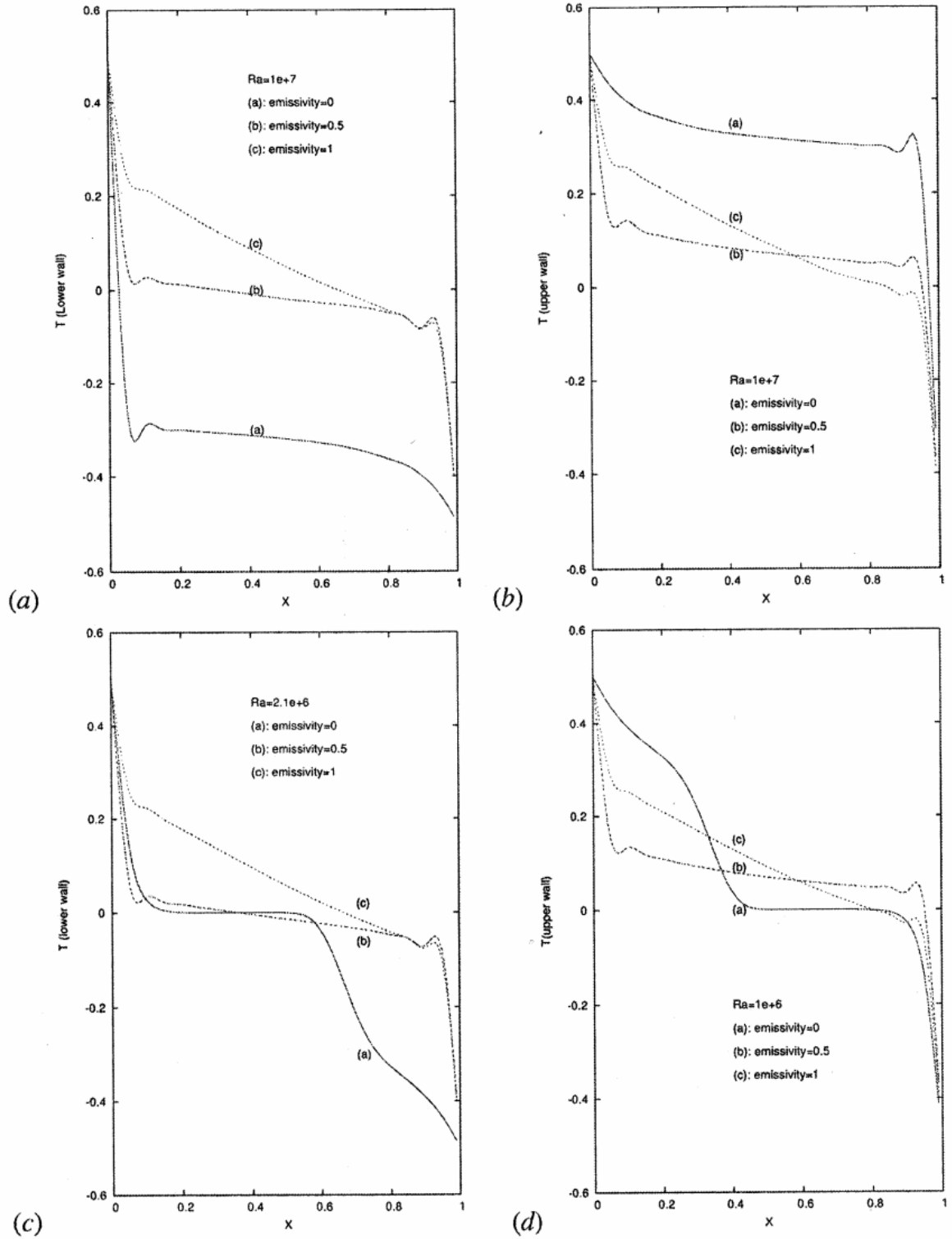


Figure 1-7 Temperature profiles on lower and upper insulated walls for several Ra-numbers and emissivity values

Jaballah et al. (2007) reported that the temperature increases from the mean towards the lower wall whereas it decreases towards the upper wall, and in general the surface radiation had an effect on the surface temperatures and consequently on the flow characteristics. To further show the effects of the surface radiation, the temperature field (isotherms), velocity field and streamlines were compared for several Ra numbers with different emissivity values. Figure 1-8 shows the steady state solutions for (a) $Ra = 2.1 \times 10^6$, (b) $Ra = 10^7$, (c) $Ra = 5 \times 10^7$ without taking into consideration emissivity of the surfaces. Figure 1-9 shows the steady state solutions considering an emissivity value of 0.5 for all surfaces.

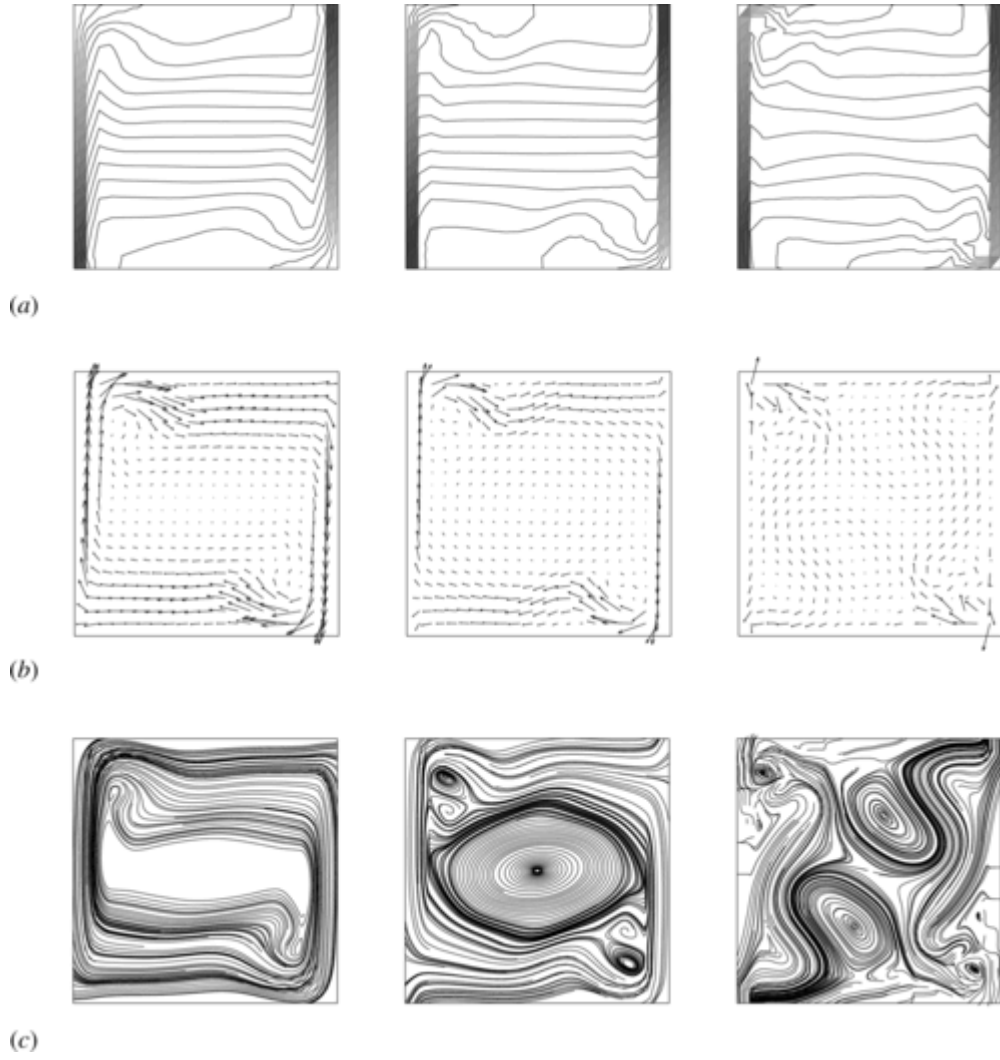


Figure 1-8 Isotherms (a), velocity fields (b) and streamlines (c) without emissivity for Ra-numbers of 2.1×10^6 , 10^7 and 5×10^7

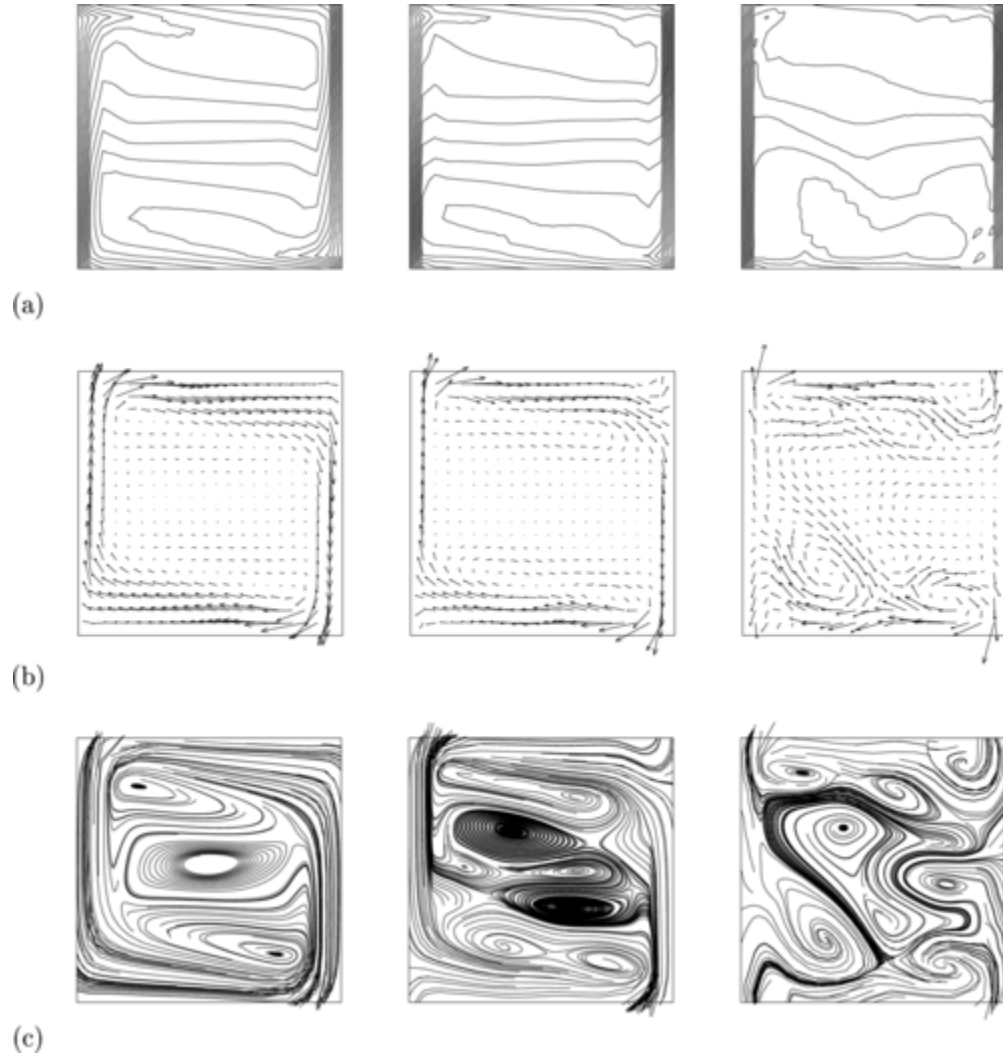


Figure 1-9 Isotherms (a), velocity fields (b) and streamlines (c) for $\varepsilon=0.5$ for Ra-numbers of 2.1×10^6 , 10^7 and 5×10^7

Further work in this study involved calculating the Nusselt number at a point on the hot wall for increasing Ra numbers and emissivity values of 0 and 0.5. Jaballah et al. (2007) reported that heat transfer between the wall and air increased with the Ra number and that the average convective and radiative Nusselt numbers are affected by the radiation relative to the value of the Ra number.

1.2.4 Thermal Comfort – Air Velocity

Air velocities in atria are typically higher than in other spaces because in order to get sufficient air circulation in such a large space, velocities outside the comfort range of occupants are needed to distribute the air. Air temperatures typically fluctuate more because of the large amount of glazing in the area and both of these variables greatly affect human comfort. Jones et al. (1992) published a paper reviewing the applications of CFD in building design and examined the current capabilities of CFD in this area. It was reported that thermal comfort (including air velocity, temperature and humidity levels), the effectiveness and efficiency of energy balance and the effectiveness of the ventilation system were three major aspects to consider when modeling air flow in buildings. Jones stated that mean velocity in the occupied zone should not exceed 0.15m/s in the winter, and 0.25m/s in the summer. This is consistent to the results published in the ASHRAE Handbook (2005). Figure 1-10 shows the percentage of dissatisfied subjects who felt a draft in the upper part of the body (head, neck, shoulders and back) as a function of air velocity in a study done by Fanger et al. (1986).

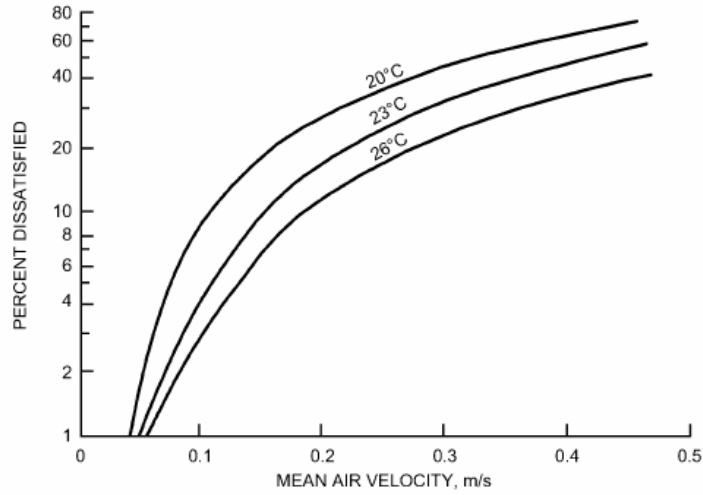


Figure 1-10 Percentage of people dissatisfied as a function of mean air velocity

Fanger et al. (1986) found that air temperature played a significant role in those who were dissatisfied, however no difference between male and females was noticed. Furthermore, Berglund et al. (1987) studied the effect of air velocity over the whole body and found no thermal comfort issues in neutral environments for air velocities of 0.25m/s or less. Fanger et al. (1989) continued work on thermal comfort investigating the effect of thermal comfort on sensation of draft. A model for predicting the percentage of dissatisfied occupants (PD) for specific turbulence intensities was created and used the following equations:

$$PD = (34 - t_a)(V - 0.05)^{0.62}(0.37V \cdot Tu + 3.14) \quad (1.3)$$

where Tu is the turbulence intensity in percent defined as

$$Tu = \frac{V_{sd}}{V} \quad (1.4)$$

where V_{sd} is the standard deviation of the velocity from the mean. This model can be used to identify the risk of high drafts in spaces or to develop air distribution systems requiring low drafts for human comfort. Using this model and a percentage of dissatisfied occupants equal to 15%, Fanger et al. (1989) produced results shown in Figure 1-11 that relate the turbulent intensity and temperature.

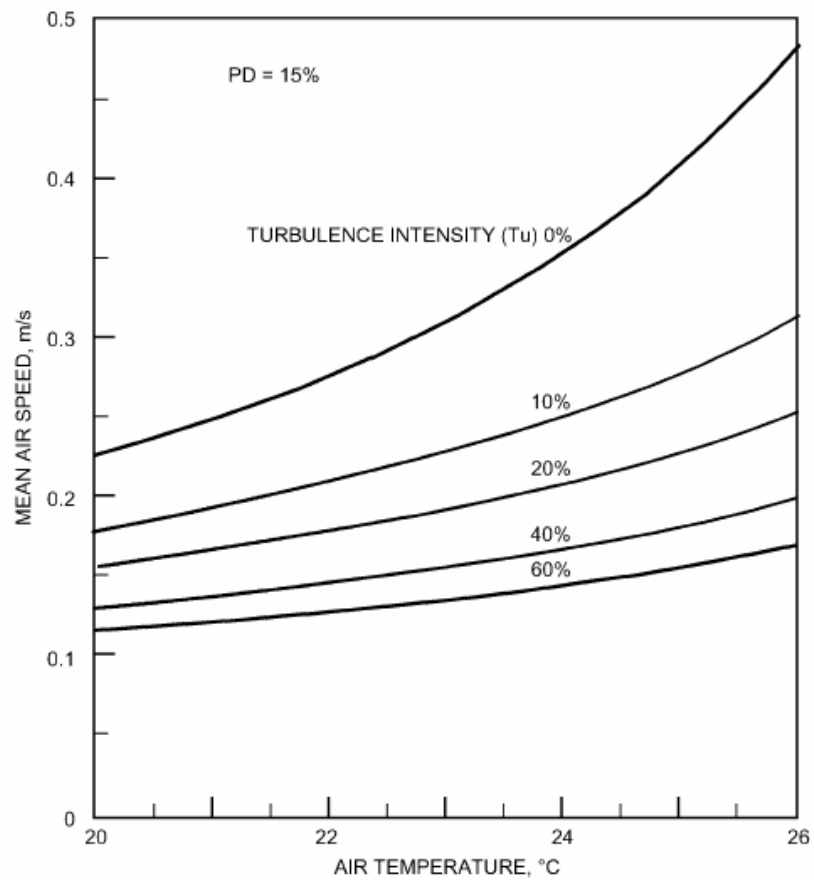


Figure 1-11 Draft conditions dissatisfying 15% of the population

1.2.5 Thermal Comfort – Air Temperature

In order to assure human comfort in large spaces, it is important to consider the effect of changes in air temperature. As previously mentioned, Jones et al. (1992) reported that thermal comfort (including air velocity and temperature and humidity levels) is a crucial aspect of building design when considering air flow. The paper by Jones et al. (1992) reported that for proper comfort levels, the mean air temperatures should range from 16°C to 26°C. The value also depends on the activity level and clothing level, but regardless the difference in temperature should not exceed 3°C. Articles published in the ASHRAE Handbook (2005) support these results stating that if a temperature gradient is sufficiently large, local discomfort (too much warmth) can occur at the head and/or local discomfort (too much cold) can occur at the feet even if the body as a whole is thermally neutral. Olesen et al. (1979) tested subjects sitting in a chamber exposed to different air temperature differences between the head and ankles. Results are given in Figure 1-12 where percentage of dissatisfied occupants is plotted as a function of the vertical temperature difference between the head and ankles (head = 1.1m from floor, ankles = 0.1m from floor).

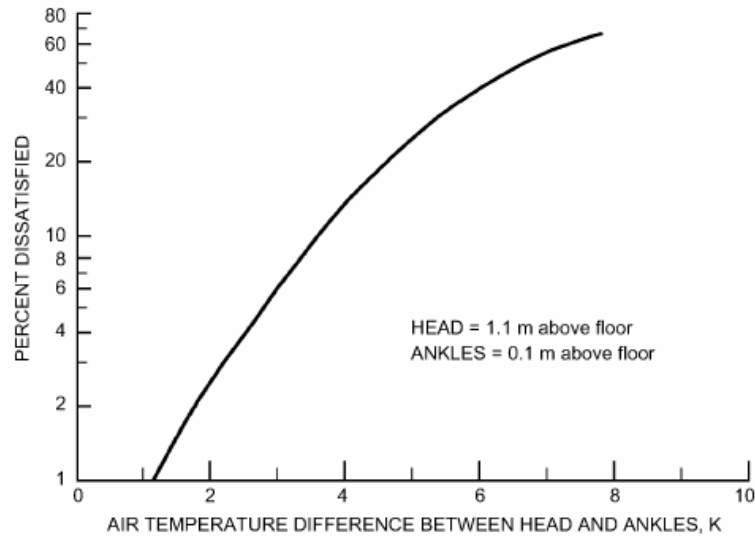


Figure 1-12 Percentage of seated people dissatisfied as a function of air temperature difference between head and ankles

It was also reported that thermal discomfort was not an issue when ankle level temperatures exceeded head level temperature. Eriksson (1975) and others reported that occupants tolerated much larger differences in temperatures when the head level temperature was cooler.

Solar radiation has an impact on the comfort of occupants in a room. High amounts of direct solar radiation entering through large glazed walls in atria can cause discomfort to occupants as it is a source of an immediate increase in surface temperature. The effect of solar radiation was considered in the modeling of the atria, however an investigation into the shading of the façade is not within the scope of this project and therefore will not be discussed in this report.

1.2.6 Turbulent Flow and Modeling Turbulence

In fluid dynamics turbulent flow is characterized by chaotic property changes or by random motion of fluid within a flow domain. Non-turbulent flow is laminar or streamline flow where the fluid flows in parallel layers with no disruption between the layers. The Reynolds number is used to indicate whether a flow is considered laminar or turbulent. It is defined as the ratio of inertial forces to viscous forces and given in equation 1.5

$$\text{Re} = \frac{\rho v_s^2 / L}{\mu v_s / L^2} = \frac{v_s L}{\nu} \quad (1.5)$$

where v_s is the mean fluid velocity (m/s), L is the characteristic dimension (m), μ is the dynamic fluid viscosity (N s / m²), ν is the kinematic fluid viscosity (m²/s) also defined as $\frac{\mu}{\rho}$, and ρ is the fluid density (Kg/m³). The transition from laminar to turbulent flow depends on the flow configuration. For flow over a flat plate, the transition occurs at a Reynolds number of the order 10⁵ to 10⁶. Flows in circular pipes typically have a generally accepted critical Reynolds number of between 2000 and 3000. When buoyancy becomes significant in flows, the Rayleigh number becomes an indicator of the character of the flow. The Rayleigh number (Ra) is defined by equation 1.6.

$$\text{Ra} = \frac{\beta g \rho^2 L^3 \theta C_p}{\mu K} \quad (1.6)$$

where C_p is the specific heat, g is gravitational acceleration, K is the thermal conductivity, β is the expansion coefficient, and θ is the temperature difference. The transition to turbulence generally occurs at Rayleigh numbers between 10⁶ and 10¹⁰.

There are two methods of solving the Navier Stokes equations without directly simulating the small scale turbulent fluctuations: Reynolds Averaging (ensemble averaging) and filtering. The Reynolds-averaged Navier Stokes (RANS) based modeling approach reduces the computational efforts and resources by time averaging the flow quantities for a whole range of scales of turbulence being modeled. Two RANS based turbulence models were compared: (1) K-Epsilon; (2) K-Omega. Large Eddy Simulation (LES) is an alternative approach to modeling turbulence where a time dependant simulation using the “filtered” Navier Stokes equations explicitly computes large eddies. The filtered or mathematically altered equations essentially remove eddies that are smaller than the size of the filter or mesh size. LES requires large computational resources for high Reynolds number flows and since the flow in the current study is mostly low Reynolds numbers, LES turbulence modeling was still investigated. Finally a Detached Eddy Simulation (DES) model was investigated. This method combines an unsteady RANS version of the Spalart Allmaras model with a filtered version of the same model creating two separate zones in the flow domain. The near wall regions are modeled using the RANS-based approach and the core flow that is usually dominated by large scale turbulence, is modeled using the LES-based approach. The FLUENT literature recommends that the Reynolds Averaged approach be used for practical applications.

Sodja et al (2007) did studies on the difference between using RANS modeling techniques and LES modeling techniques. It was stated in this reference that using RANS, the computational costs can be reduced by solving the statistically averaged equation system, which requires closure assumptions for the higher moments. LES aims to reduce the dependence on the turbulence model. Hence the major portion of the flow is simulated without any models, and must be resolved by the grid. Only scales smaller than the resolution of the

grid need a model. Consequently LES approach is computationally more demanding than RANS. RANS models have a computing time of only about 5% of the LES.

Jones et al. (1992) describe in detail the current capabilities of CFD in building simulation highlighting several advantages and disadvantages of turbulence modeling techniques. It was noted that the eddy viscosity method is robust and simple but when used with care can compute acceptable results. The k-epsilon model is the most widely used turbulence model as it is a compromise between level of sophistication and computational efficiency. One assumption in the k-epsilon model is that the flow is isotropic which is why the Reynolds stress model was introduced. The Reynolds stress model uses five differential equations in each cell of the domain making it able to better deal with swirling flows, but also making it much more computationally expensive. Clarke et al. (1988) gave an increase in computational time between 50% and 100% when using the Reynolds stress model. Jones et al. (2002) stated that Large Eddy Simulation is an even more sophisticated type of turbulence modeling requiring very fine meshes. The LES model is still at the research stage and therefore not ready for use within engineering design. The final approach mentioned by Jones et al. (1992) is the direct simulation or direct numerical simulation (DNS) approach which is being studied by few research groups around the world including. DNS solves the turbulence equations directly, with no simplification and requires large computational expense especially for large flow fields such as building simulations. Further explanation of turbulence models is given in section 2.3.

In conclusion Jones et al. (1992) pointed out that when modeling building air flow, if approximations need to be made, implementing careful engineering judgment results in a reduction of accuracy rather than the inability to obtain a solution.

1.3 Present Study

The goal of the present study was to select a numerical model that accurately predicts the turbulent flow in a large atrium similar to the Concordia Atrium described later in this section. Since there were essentially no experimental data available for the Concordia-like atrium, other cases for which experimental results were available (work done by Salat et al. (2004) and work done by Heiselburg et al. (1998)) were investigated in order to gain confidence in the modeling techniques used in the modeling of a Concordia-like atrium. Once a model was chosen for the Concordia-like atrium, the effects of the forced flow inlet angle and velocity, as well as, the effects of natural ventilation with several external conditions was investigated.

The specific objectives of the Concordia-like atrium study are therefore as follows:

- (1) Create a 3-dimensional computational grid with a mesh dense enough to accurately predict air flow in large spaces without creating excessive computational demands;
- (2) Develop the physical model and boundary conditions for this type of geometry;
- (3) Compare results given by several turbulence models for this situation;
- (4) Choose one model to investigate the effects of flow inlet vent angle and velocity as well as the effects of natural convection for several external conditions.

The objective for studying the 1m cubic cavity by Salat et al. (2004) is as follows:

- (5) Create a 3-dimensional model similar to the geometry in the literature. Compare the results of several turbulence models to the experimental results produced by Salat et al. (2004).

The objective of the study on the Annex 26 Atrium by Heiselburg et al. (1998) is as follows:

- (6) Create a 3-dimensional model comparable to the geometry used by Heiselburg et al. (1998). Again compare the results of several turbulence models to the experimental results produced by Heiselburg et al.

1.4 Methodology

The grid was generated using a commercial CADD software package (Gambit 2.3.16) and the numerical computation was accomplished using a commercial Finite Volume Method software package (FLUENT 6.2.16). The laws of conservation of mass (continuity) and momentum, the continuity, and energy equations were established and solved creating a model for the specific problem. The model has been used to determine the temperature and velocity profiles and local dimensionless heat transfer coefficients with different input parameters and boundary conditions. The results were used to compare the effects of several turbulence models, as well as, flow inlet angle and velocity.

The modeling techniques used in the present study were used to model similar situations presented by Salat et al. (2004) and Heiselburg et al. (1998). The numerical and experimental results were compared in order to justify the modeling techniques used

in this study and have shown that it is possible to accurately predict the air flow using these techniques.

Chapter 2 – Numerical Models

2.1 Introduction

This chapter explains the turbulent and heat transfer numerical models used in the present study. The governing equations and boundary conditions for all studies are presented in this section. The domain is separated into small cells to form a volume mesh (or grid) using the program GAMBIT and algorithms in FLUENT are used to solve the governing equations for viscous flow, i.e. the Navier Stokes equations.

2.2 Basic Model and Assumptions

2.2.1 Assumptions

The numerical model is based on the following assumptions:

- the flow is steady, turbulent and three-dimensional;
- the flow is single phase, i.e., the effects of dust particles and/or water vapour have been neglected;
- the velocity is uniform over the vent inlet
- the air properties are constant, except for the density change with temperature, which has been treated using the Boussinesq Approximation.

Governing Equations

The flows being considered involve mechanically induced flow (air entering through a vent) and buoyant forces that drive the air motion in the domain considered. An important factor in the flow calculations is taking into consideration the buoyant forces (natural convective flow) that arise due to differences in fluid density due to temperature difference. The air flow can be considered incompressible as the velocities are low (air flows can usually be considered incompressible if the Mach number is less than roughly 0.3 or about 100m/s). Also air being a Newtonian fluid displays a linear relationship between shear and strain rate. The laws of conservation of mass (continuity) and momentum are used to describe the flow based on the assumptions discussed. Equations (2.1), (2.2), (2.3), and (2.4) below are Navier Stokes equations in the x, y and z directions and the continuity equation which describes the flow.

Momentum in x-direction

$$\frac{\partial}{\partial t}(\rho u) + \frac{\partial}{\partial x}(\rho uu) + \frac{\partial}{\partial y}(\rho uv) + \frac{\partial}{\partial z}(\rho wu) = -\frac{\partial P}{\partial x} + \mu \left(\frac{\partial^2 u}{\partial x^2} + \frac{\partial^2 u}{\partial y^2} + \frac{\partial^2 u}{\partial z^2} \right) \quad (2.1)$$

Momentum in y-direction

$$\begin{aligned} \frac{\partial}{\partial t}(\rho v) + \frac{\partial}{\partial x}(\rho uv) + \frac{\partial}{\partial y}(\rho vv) + \frac{\partial}{\partial z}(\rho wv) = \\ -\frac{\partial P}{\partial y} + \mu \left(\frac{\partial^2 v}{\partial x^2} + \frac{\partial^2 v}{\partial y^2} + \frac{\partial^2 v}{\partial z^2} \right) - \rho g \beta (T_{\infty} - T) \end{aligned} \quad (2.2)$$

Momentum in z-direction

$$\frac{\partial}{\partial t}(\rho w) + \frac{\partial}{\partial x}(\rho uw) + \frac{\partial}{\partial y}(\rho vw) + \frac{\partial}{\partial z}(\rho ww) = -\frac{\partial P}{\partial z} + \mu \left(\frac{\partial^2 w}{\partial x^2} + \frac{\partial^2 w}{\partial y^2} + \frac{\partial^2 w}{\partial z^2} \right) \quad (2.3)$$

Continuity

$$\frac{\partial}{\partial x}(\rho u) + \frac{\partial}{\partial y}(\rho v) + \frac{\partial}{\partial z}(\rho w) = 0 \quad (2.4)$$

The y-axis of the Cartesian coordinate system is aligned in the vertical direction as shown in Figure 2-1. u , v and w are the velocity components in the x , y and z directions respectively, ρ is the mass density, μ is the viscosity and β is the thermal expansion coefficient of air. t is time, T is the temperature, P is the pressure, and g is the gravitational acceleration. The Boussinesq approximation was used and therefore fluid properties were assumed constant except for the density change with temperature which leads to the buoyancy forces. The density change is assumed to be proportional to the temperature difference.

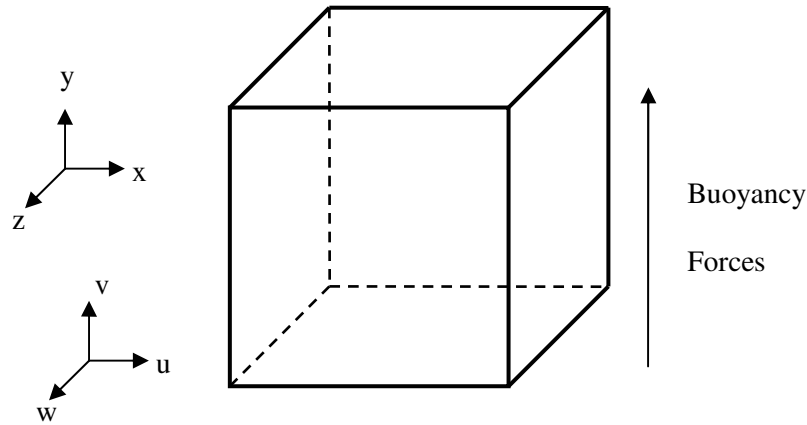


Figure 2-1 Coordinate system and control volume used in present study

The equation of continuity simply states that mass is conserved or that the net accumulation of mass in the control volume is zero in steady flow. Each term in the continuity equation represents the net mass flow through a face perpendicular to one of the respective axis.

Because the y direction equation contains a temperature dependant term, a necessary addition to the Navier Stokes equations is the energy equation. Because of the assumptions being used, the conservation of energy equation is:

$$\frac{\partial}{\partial t}(\rho c_p T) + \frac{\partial}{\partial x}(\rho u c_p T) + \frac{\partial}{\partial y}(\rho v c_p T) + \frac{\partial}{\partial z}(\rho w c_p T) = K \left(\frac{\partial^2 T}{\partial x^2} + \frac{\partial^2 T}{\partial y^2} + \frac{\partial^2 T}{\partial z^2} \right) + q''' \quad (2.5)$$

where c_p is the specific heat (J/kgK), and K is the conductivity (W/m K) of the fluid and q''' is the rate of internal heat generation.

Equations 2.1 to 2.5 describe the flow and temperature distributions. For turbulent flow, the velocity and temperature vary with time and this study will investigate and compare several models that have been developed to predict turbulent flow.

2.3 Turbulence Models

Fluctuations in the velocity field mix transported quantities such as momentum and energy and cause the transported quantities to fluctuate as well. These fluctuations can be of a very small scale and therefore can create extremely large computational expenses for practical engineering calculations. A modified set of equations that require much less computational expense are used. This is done by time-averaging the instantaneous governing equations which then contain additional unknown variables. Turbulence models are needed to solve these unknown variables.

No single turbulence model can be universally applied to all situations. Some consideration must be taken when choosing a turbulence model including; physics encompassed in the flow; level of accuracy; and computation resources available. Several turbulence transport models will be examined and discussed in this section. Both the Realizable and RNG (Renormalization Group) K-Epsilon models along with the standard K-epsilon turbulence models were tested. The standard and Shear Stress Transport variations of the K-Omega turbulence model were examined, as well as, the Detached Eddy Simulation (DES) model and the Large Eddy Simulation (LES) model.

The equations of motion are averaged with respect to time and these turbulent transport models predict the effect of turbulence on the time averaged mean motion. Since all of the terms currently in the equations of motion are instantaneous values, they are replaced with the sum of a time-mean quantity and a fluctuating quantity. (for instance $T = \bar{T} + T'$). A new set of equations of motion with the same form are obtained with the addition of these quantities.

Energy

$$\begin{aligned} \frac{\partial}{\partial t}(\rho c_p \bar{T}) + \frac{\partial}{\partial x}(\rho \bar{u} c_p \bar{T}) + \frac{\partial}{\partial y}(\rho \bar{v} c_p \bar{T}) + \frac{\partial}{\partial z}(\rho \bar{w} c_p \bar{T}) \\ = K \left(\frac{\partial^2 \bar{T}}{\partial x^2} + \frac{\partial^2 \bar{T}}{\partial y^2} + \frac{\partial^2 \bar{T}}{\partial z^2} \right) - \frac{\partial}{\partial x_i}(\rho c_p \bar{T}' u'_i) + q''' \end{aligned} \quad (2.6)$$

Momentum in x-direction

$$\begin{aligned} \frac{\partial}{\partial t}(\rho \bar{u}) + \frac{\partial}{\partial x}(\rho \bar{u} \bar{u}) + \frac{\partial}{\partial y}(\rho \bar{v} \bar{u}) + \frac{\partial}{\partial z}(\rho \bar{w} \bar{u}) = -\frac{\partial \bar{P}}{\partial x} + \mu \left(\frac{\partial^2 \bar{u}}{\partial x^2} + \frac{\partial^2 \bar{u}}{\partial y^2} + \frac{\partial^2 \bar{u}}{\partial z^2} \right) - \frac{\partial}{\partial x_i}(\rho \bar{u}' u'_i) \end{aligned} \quad (2.7)$$

Momentum in y-direction

$$\begin{aligned} \frac{\partial}{\partial t}(\rho \bar{v}) + \frac{\partial}{\partial x}(\rho \bar{u} \bar{v}) + \frac{\partial}{\partial y}(\rho \bar{v} \bar{v}) + \frac{\partial}{\partial z}(\rho \bar{w} \bar{v}) \\ = -\frac{\partial \bar{P}}{\partial y} + \mu \left(\frac{\partial^2 \bar{v}}{\partial x^2} + \frac{\partial^2 \bar{v}}{\partial y^2} + \frac{\partial^2 \bar{v}}{\partial z^2} \right) - \frac{\partial}{\partial x_i}(\rho \bar{v}' u'_i) - \rho g \beta (\bar{T}_\infty - \bar{T}) \end{aligned} \quad (2.8)$$

Momentum in z-direction

$$\begin{aligned} \frac{\partial}{\partial t}(\rho \bar{w}) + \frac{\partial}{\partial x}(\rho \bar{u} \bar{w}) + \frac{\partial}{\partial y}(\rho \bar{v} \bar{w}) + \frac{\partial}{\partial z}(\rho \bar{w} \bar{w}) = -\frac{\partial \bar{P}}{\partial z} + \mu \left(\frac{\partial^2 \bar{w}}{\partial x^2} + \frac{\partial^2 \bar{w}}{\partial y^2} + \frac{\partial^2 \bar{w}}{\partial z^2} \right) - \frac{\partial}{\partial x_i}(\rho \bar{w}' u'_i) \end{aligned} \quad (2.9)$$

Continuity

$$\frac{\partial}{\partial x}(\rho u) + \frac{\partial}{\partial y}(\rho v) + \frac{\partial}{\partial z}(\rho w) = 0 \quad (2.10)$$

The momentum equations have the term $-\partial/\partial x_i (\rho \overline{u'_j u'_i})$ given in compact tensor notation¹. These terms represent the effect that turbulent motion has on the time-mean quantities known as Reynold's stresses which are high frequency fluctuating velocity components. The new terms in the energy equation $(-\partial/\partial x_i (\rho c_p \overline{T' u'_i}))$ represents the turbulent heat fluxes which are the fluctuating components of the temperature and velocity.

The eddy-viscosity concept proposed by Boussinesq can then be applied to the motion equations. The additional turbulent stresses are assumed to be proportional to the mean-velocity gradients. The stresses in tensor notation can be related as follows.

$$\overline{u'_j u'_i} = \frac{\mu_t}{\rho} \left(\frac{\partial \bar{u}_j}{\partial x_i} + \frac{\partial \bar{u}_i}{\partial x_j} \right) - \frac{2}{3} k \delta_{ji} \quad (2.11)$$

where μ_t is the eddy viscosity, k is the kinetic energy, and δ_{ji} is the Kronecker delta. This approach is used in both the k-epsilon and k-omega models. The advantage being that computational costs are relatively low because of the computational power needed to calculate the turbulent viscosity. Also, the turbulent heat fluxes are assumed to be proportional to the mean temperature gradients and are again expressed in tensor notation.

$$-\rho c_p \overline{T' u'_i} = c_p \Gamma \frac{\partial \bar{T}}{\partial x_j} \quad (2.12)$$

¹ In x-direction, $\frac{\partial}{\partial x_i} (\rho \overline{u'_j u'_i})$ expands to $\frac{\partial}{\partial x} (\rho \overline{u'_j u'_i}) + \frac{\partial}{\partial y} (\rho \overline{u'_j v'_i}) + \frac{\partial}{\partial z} (\rho \overline{u'_j w'_i})$

where Γ is the turbulent diffusivity of heat. Both the eddy viscosity and the turbulent diffusivity of heat are properties of the flow, not the fluid. In order to relate these two quantities together, the turbulent Prandtl number is introduced. It can be assumed constant as experiments have shown that this ratio does not vary in flows or between flows even though μ_t and Γ do.

$$\sigma_t = \frac{\mu_t}{\Gamma} \quad (2.13)$$

By substituting equations 2.11, 2.12 and 2.13 into the equations of motion (equations 2.6 to 2.10) the fluctuating quantities are removed as eddy viscosity and mean quantity gradients describe the turbulent diffusion and the equations of motion are represented as follows.

Energy

$$\begin{aligned} \frac{\partial}{\partial t}(\rho c_p \bar{T}) + \frac{\partial}{\partial x}(\rho \bar{u} c_p \bar{T}) + \frac{\partial}{\partial y}(\rho \bar{v} c_p \bar{T}) + \frac{\partial}{\partial z}(\rho \bar{w} c_p \bar{T}) \\ = K \left(\frac{\partial^2 \bar{T}}{\partial x^2} + \frac{\partial^2 \bar{T}}{\partial y^2} + \frac{\partial^2 \bar{T}}{\partial z^2} \right) + \frac{\partial}{\partial x_i} \left(\frac{\partial \bar{T}}{\partial x_i} \frac{c_p \mu_t}{\sigma_t} \right) + q''' \end{aligned} \quad (2.14)$$

Momentum in x-direction

$$\frac{\partial}{\partial t}(\rho \bar{u}) + \frac{\partial}{\partial x}(\rho \bar{u} \bar{u}) + \frac{\partial}{\partial y}(\rho \bar{v} \bar{u}) + \frac{\partial}{\partial z}(\rho \bar{w} \bar{u}) = -\frac{\partial \bar{P}}{\partial x} + (\mu + \mu_t) \left(\frac{\partial^2 \bar{u}}{\partial x^2} + \frac{\partial^2 \bar{u}}{\partial y^2} + \frac{\partial^2 \bar{u}}{\partial z^2} \right) \quad (2.15)$$

Momentum in y-direction

$$\begin{aligned} \frac{\partial}{\partial t}(\rho \bar{v}) + \frac{\partial}{\partial x}(\rho \bar{u} \bar{v}) + \frac{\partial}{\partial y}(\rho \bar{v} \bar{v}) + \frac{\partial}{\partial z}(\rho \bar{w} \bar{v}) \\ = -\frac{\partial \bar{P}}{\partial y} + (\mu + \mu_t) \left(\frac{\partial^2 \bar{v}}{\partial x^2} + \frac{\partial^2 \bar{v}}{\partial y^2} + \frac{\partial^2 \bar{v}}{\partial z^2} \right) - \rho g \beta (\bar{T}_\infty - \bar{T}) \end{aligned} \quad (2.16)$$

Momentum in z-direction

$$\frac{\partial}{\partial t}(\rho \bar{w}) + \frac{\partial}{\partial x}(\rho \bar{u} \bar{w}) + \frac{\partial}{\partial y}(\rho \bar{v} \bar{w}) + \frac{\partial}{\partial z}(\rho \bar{w} \bar{w}) = -\frac{\partial \bar{P}}{\partial z} + (\mu + \mu_t) \left(\frac{\partial^2 \bar{w}}{\partial x^2} + \frac{\partial^2 \bar{w}}{\partial y^2} + \frac{\partial^2 \bar{w}}{\partial z^2} \right) \quad (2.17)$$

Continuity

$$\frac{\partial}{\partial x}(\rho \bar{u}) + \frac{\partial}{\partial y}(\rho \bar{v}) + \frac{\partial}{\partial z}(\rho \bar{w}) = 0 \quad (2.18)$$

This form of the equations differs from the original instantaneous equations due only to the momentum and heat diffusion coefficients. The new terms in the momentum and energy equations represent the influence of turbulence on the time-mean quantities. The following sections describe the turbulence models that will be tested in order to determine which model gives the best results for large atrium flow, specifically the case described at the beginning of this section.

2.3.1 K-Epsilon Turbulence Model

The K-Epsilon model has become one of the most widely used turbulence models as it provides robustness, economy and reasonable accuracy for a wide range of turbulent flows. Improvements have been made to the standard model which improves its performance and two variants are available in Fluent; the RNG (renormalization group) model and the realizable model. Three versions of the K-Epsilon model will be investigated here. The standard, RNG, and realizable models have similar form with transport equations for k and ε . The two transport equations independently solve for the turbulent velocity and length scales. The main differences between the three models are as follows;

- The turbulent Prandtl Numbers governing the turbulent diffusion of k and ε

- The generation and destruction terms in the equation for ε
- The method of calculating turbulent viscosity

2.3.1.1 Standard K-Epsilon Turbulence Model

This original model was initially proposed by Launder and Spalding (1972). For this model the transport equation for k is derived from the exact equation, but the transport for ε was obtained using physical reasoning and is therefore similar to the mathematically derived transport equation of k , but is not exact. The turbulent kinetic energy k , and its rate of dissipation ε , for this model are obtained by the following equations.

$$\frac{\partial}{\partial t}(\rho k) + \frac{\partial}{\partial x_i}(\rho k u_i) = \frac{\partial}{\partial x_j} \left[\left(\mu + \frac{\mu_t}{\sigma_k} \right) \frac{\partial k}{\partial x_j} \right] + G_k + G_b - \rho \varepsilon - Y_M + S_K \quad (2.19)$$

$$\frac{\partial}{\partial t}(\rho \varepsilon) + \frac{\partial}{\partial x_i}(\rho \varepsilon u_i) = \frac{\partial}{\partial x_j} \left[\left(\mu + \frac{\mu_t}{\sigma_\varepsilon} \right) \frac{\partial \varepsilon}{\partial x_j} \right] + C_{1\varepsilon} \frac{\varepsilon}{k} (G_k + C_{3\varepsilon} G_b) - C_{2\varepsilon} \rho \frac{\varepsilon^2}{k} + S_\varepsilon \quad (2.20)$$

where G_k represents the generation of turbulent kinetic energy that arises due to mean velocity gradients, G_b is the generation of turbulent kinetic energy that arises due to buoyancy, and Y_M represents the fluctuating dilation in compressible turbulence that contributes to the overall dissipation rate. S_ε and S_k are source terms defined by the user.

$C_{1\varepsilon}$, $C_{2\varepsilon}$ and C_μ are constants that have been determined experimentally and are taken to have the following values;

$$C_{1\varepsilon}=1.44, \quad C_{2\varepsilon}=1.92, \quad C_\mu=0.09$$

σ_k and σ_ε are turbulent Prandtl numbers for the turbulent kinetic energy and its dissipation rate. These have also been derived experimentally and are defined as follows.

$$\sigma_k=1.0, \quad \sigma_\varepsilon=1.3$$

The turbulent (or eddy) viscosity at each point is related to the local values of turbulent kinetic energy and its dissipation rate by;

$$\mu_t = \rho C_\mu \frac{k^2}{\varepsilon} \quad (2.21)$$

where C_μ is constant and defined above.

The term for the production of turbulent kinetic energy G_k is common in many of the turbulence models studied and is defined as

$$G_k = -\overline{\rho u'_i u'_j} \frac{\partial u_j}{\partial x_i} \quad (2.22)$$

The modulus of mean rate-of-strain tensor, S is defined as

$$S = \sqrt{2S_{ij}S_{ij}} \quad (2.23)$$

The generation of turbulent kinetic energy that arises due to buoyancy, G_b is defined as follows

$$G_b = \beta g_i \frac{\mu_t}{Pr_t} \frac{\partial T}{\partial x_i} \quad (2.24)$$

As the present study uses relatively low velocities, the dilation dissipation term, Y_M which accounts for turbulence from compressibility effects is defined as

$$Y_M = 2\rho\varepsilon M_t^2 \quad (2.25)$$

2.3.1.2 RNG K-Epsilon Turbulence Model

Similar to the standard k-epsilon model, the RNG model was derived from the instantaneous Navier Stokes equations, except it uses a technique called renormalization group theory described by Yakhot and Orszag (1986). This derivation produces a model with different constants to those used in the standard k-epsilon model and also adds new terms to the transport equations for the turbulent kinetic energy and its dissipation. The effect of swirl is also accounted for in the RNG model enhancing the accuracy of swirling flows. An analytical formula for turbulent Prandtl numbers is provided in this model while the standard model relies on user-specific constant values. Finally, assuming appropriate treatment of the near wall region, the RNG model uses an analytically derived differential formula for the effective turbulent viscosity which accounts for low Reynolds number flows. The RNG K-Epsilon model is therefore more accurate and more reliable than the standard K-Epsilon model for a wider range of flows.

As a result from these differences, the transport equations appear as follows.

$$\frac{\partial}{\partial t}(\rho k) + \frac{\partial}{\partial x_i}(\rho k u_i) = \frac{\partial}{\partial x_j} \left[\alpha_k \mu_{eff} \frac{\partial k}{\partial x_j} \right] + G_k + G_b - \rho \epsilon - Y_M + S_K \quad (2.26)$$

$$\frac{\partial}{\partial t}(\rho \epsilon) + \frac{\partial}{\partial x_i}(\rho \epsilon u_i) = \frac{\partial}{\partial x_j} \left[\alpha_\epsilon \mu_{eff} \frac{\partial \epsilon}{\partial x_j} \right] + C_{1\epsilon} \frac{\epsilon}{k} (G_k + C_{3\epsilon} G_b) - C_{2\epsilon} \rho \frac{\epsilon^2}{k} - R_\epsilon + S_\epsilon \quad (2.27)$$

where G_k represents the generation of turbulent kinetic energy that arises due to mean velocity gradients, G_b is generation of turbulent kinetic energy the arises due to buoyancy, and Y_M represents the fluctuating dilation in compressible turbulence that contributes to the overall dissipation rate. S_ϵ and S_k are source terms defined by the user. α_k and α_ϵ are inverse effective Prandtl numbers for the turbulent kinetic energy and its dissipation.

The RNG theory uses a scale elimination procedure that defines the effective viscosity given in the following equation.

$$d\left(\frac{\rho^2 k}{\sqrt{\epsilon \mu}}\right) = 1.72 \frac{\hat{v}}{\sqrt{\hat{v}^3 - 1 + C_v}} d\hat{v} \quad (2.28)$$

where $\hat{v} = \mu_{eff} / \mu$ and C_v is a constant equal approximately to 100. This equation incorporates the ability to accurately define how the effective turbulent transport varies with effective Reynolds number to obtain more accurate results for low-Re flows and near-wall flows. For high Reynolds numbers, the effective viscosity is defined by the following ratio;

$$\mu_t = \rho C_\mu \frac{k^2}{\epsilon} \quad (2.29)$$

Although this is similar to the turbulent viscosity of the standard model, the constant C_μ is derived using the RNG theory and found to be 0.0845 which is very close to the value used in the standard model (i.e., 0.09).

$C_{1\epsilon}$ and $C_{2\epsilon}$ are constants that have been derived analytically by the RNG theory and are defined as follows.

$$C_{1\epsilon} = 1.42, \quad C_{2\epsilon} = 1.68$$

2.3.1.3 Realizable K-Epsilon Turbulence Model

The Realizable model by Shih (1995) is the most recently developed of the three K-Epsilon variations and features two main differences from the standard K-Epsilon model. It uses a new equation for the turbulent viscosity and the dissipation rate transport equation has been derived from the equation for the transport of the mean-square vorticity

fluctuation. The form of the eddy viscosity (turbulent) equations is based on the realizability constraints; the positivity of normal Reynolds stresses and Schwarz' inequality for turbulent shear stresses (i.e., certain mathematical constraints on the normal stresses are satisfied). This is not satisfied by either the standard or the RNG K-Epsilon models which makes the realizable model more precise than both models at predicting flows such as separated flows and flows with complex secondary flow features.

In terms of the improved changes by Shih (1995), the transport equations become:

$$\frac{\partial}{\partial t}(\rho k) + \frac{\partial}{\partial x_j}(\rho k u_j) = \frac{\partial}{\partial x_j} \left[\left(\mu + \frac{\mu_t}{\sigma_k} \right) \frac{\partial k}{\partial x_j} \right] + G_k + G_b - \rho \epsilon - Y_M + S_K \quad (2.30)$$

$$\frac{\partial}{\partial t}(\rho \epsilon) + \frac{\partial}{\partial x_j}(\rho \epsilon u_j) \quad (2.31)$$

$$= \frac{\partial}{\partial x_j} \left[\left(\mu + \frac{\mu_t}{\sigma_\epsilon} \right) \frac{\partial \epsilon}{\partial x_j} \right] + \rho C_1 S \epsilon - \rho C_2 \frac{\epsilon^2}{k + \sqrt{\nu \epsilon}} + C_{1\epsilon} \frac{\epsilon}{k} C_{3\epsilon} G_b + S_\epsilon$$

where G_k represents the generation of turbulent kinetic energy the arises due to mean velocity gradients, G_b is generation of turbulent kinetic energy the arises due to buoyancy, and Y_M represents the fluctuating dilation in compressible turbulence that contributes to the overall dissipation rate. S_ϵ and S_k are source terms defined by the user. α_k and α_ϵ are the turbulent Prandtl numbers for the turbulent kinetic energy and its dissipation.

Similar to the previous variations of the K-Epsilon models, the turbulent viscosity is determined by the formula given below; however it produces different results as C_μ is not constant.

$$\mu_t = \rho C_\mu \frac{k^2}{\varepsilon} \quad (2.32)$$

where C_μ is computed from

$$C_\mu = \frac{1}{A_0 + A_s \frac{kU^*}{\varepsilon}} \quad (2.33)$$

where

$$U^* = \sqrt{S_{ij}S_{ij} + \tilde{\Omega}_{ij}\tilde{\Omega}_{ij}} \quad \text{and} \quad \tilde{\Omega}_{ij} = \overline{\Omega_{ij}} - \varepsilon_{ijk}\omega_k - 2\varepsilon_{ijk}\omega_k$$

In the above equation, $\overline{\Omega_{ij}}$ is the mean rate of rotation tensor viewed in a rotating reference frame with angular velocity ω_k . The constants A_0 and A_s are defined as;

$$A_0 = 4.04, \quad A_s = \sqrt{6} \cos \phi$$

where

$$\phi = \frac{1}{3} \cos^{-1} \left(\sqrt{6} \frac{S_{ij}S_{jk}S_{ki}}{\tilde{S}^3} \right), \quad \tilde{S} = \sqrt{S_{ij}S_{ij}}, \quad S_{ij} = \frac{1}{2} \left(\frac{\partial u_j}{\partial x_i} + \frac{\partial u_i}{\partial x_j} \right)$$

It has been shown that C_μ is a function of the mean strain and rotational rates, the angular velocity of the rotating system, and the turbulent kinetic energy and its dissipation rate. The standard value of $C_\mu = 0.09$ is found to be the solution of equation 2.32 for an inertial sub layer in the equilibrium boundary layer.

The constants $C_{1\varepsilon}$, C_2 , σ_k and σ_ε have been determined by Shih (1995) and are defined as follows.

$$C_{1\varepsilon}=1.44, \quad C_2=1.9, \quad \sigma_k=1.0, \quad \sigma_\varepsilon=1.2$$

2.3.2 K-Omega Turbulence Model

The second turbulence model to be investigated is the K-Omega turbulence model. The K-Omega model has two variations that will both be described in this section; the standard K-Omega model, and the shear stress transport (SST) model. Both of these models use similar transport equations for k and ω but the SST model differs from the standard model as follows:

- There is a gradual change from the standard k-omega model in the inner region of the boundary layer to the k-epsilon model in the outer part of the boundary layer.
- In order to account for the transport effects of the principal turbulent shear stresses the SST model incorporates a modified turbulent viscosity equation

The following sections explain these differences, present the transport equations and show the methods of solving for turbulent viscosity and all constants.

2.3.2.1 Standard K-Omega Turbulence Model

FLUENT uses a standard K-Omega model developed by Wilcox (1998) that was formulated to better compute low-Reynolds number effects, compressibility, and shear flow spreading. The standard model is an empirical based model with transport equations for turbulent kinetic energy (k) and its specific dissipation rate (ω). This model has been modified numerous times in an attempt to improve its accuracy and as a result the transport equations used in FLUENT for Wilcox's model are as follows.

$$\frac{\partial}{\partial t}(\rho k) + \frac{\partial}{\partial x_i}(\rho k u_i) = \frac{\partial}{\partial x_i} \left[\left(\mu + \frac{\mu_t}{\sigma_k} \right) \frac{\partial k}{\partial x_j} \right] + G_k - Y_k + S_k \quad (2.34)$$

$$\frac{\partial}{\partial t}(\rho \omega) + \frac{\partial}{\partial x_i}(\rho \omega u_i) = \frac{\partial}{\partial x_j} \left[\left(\mu + \frac{\mu_t}{\sigma_\omega} \right) \frac{\partial \omega}{\partial x_j} \right] + G_\omega - Y_\omega + S_\omega \quad (2.35)$$

where G_k represents the generation of turbulent kinetic energy that arises due to mean velocity gradients and G_ω is generation of ω which are defined in the exact manner as the K-Epsilon model. Y_k and Y_ω represent the dissipation of k and ω due to turbulence. α_k and α_ω are the turbulent Prandtl numbers (constants in this case; equal to 2) for k and ω respectively and S_ϵ and S_k are source terms defined by the user.

The turbulent viscosity is defined using a damping coefficient (α^*);

$$\mu_t = \alpha^* \frac{\rho k}{\omega} \quad (2.36)$$

The low-Reynolds number correlation is obtained from this coefficient α^* which damps the turbulent viscosity. This coefficient is given by,

$$\alpha^* = \alpha_\infty^* \left(\frac{\alpha_0^* + \text{Re}_t / R_k}{1 + \text{Re}_t / R_k} \right) \quad (2.37)$$

where $\text{Re}_t = \frac{\rho k}{\mu \omega}$, $R_k = 6$, $\alpha_0^* = \beta_i / 3$ and $\beta_i = 0.072$. For the high-Re form of the standard k-omega model, $\alpha^* = \alpha_\infty^* = 1$

The term for the dissipation of k due to turbulence, Y_k is defined as

$$Y_k = \rho \beta^* f_{\beta^*} k \omega \quad (2.38)$$

and the term for the dissipation of ω due to turbulence, Y_ω is defined as

$$Y_\omega = \rho \beta f_\beta \omega^2 \quad (2.39)$$

This k-omega model was developed by Wilcox (1998) has shown comparable results for far wakes, mixing layers and various jet types which make it applicable to wall bounded flows and free shear flows. It incorporates modifications for compressibility, shear flow spreading, and low-Re number effects which are applicable in the present study.

2.3.2.2 SST K-Omega Turbulence Model

The shear stress transport K-Omega model is the only variation of the standard k-omega model available in FLUENT. It was developed by Menter (1994) using the standard k-omega model and a transformed k-epsilon model. The main difference is the way in which the model calculates the turbulent viscosity to account for the transport of the principal turbulent shear stress. This model also incorporates a cross-diffusion term in the ω equation and a blending function to allow proper calculation of the near-wall and far-field areas. The blending function triggers the standard K-Omega model in near wall regions, and triggers the K-Epsilon-like model in areas away from the surface. These differences make the SST model more precise for a larger variety of flows than the standard model.

Similar to the standard K-Omega model, the transport equations for k and ω are slightly modified and are given by;

$$\frac{\partial}{\partial t}(\rho k) + \frac{\partial}{\partial x_i}(\rho k u_i) = \frac{\partial}{\partial x_j} \left[\left(\mu + \frac{\mu_t}{\sigma_k} \right) \frac{\partial k}{\partial x_j} \right] + \tilde{G}_k - Y_k + S_k \quad (2.40)$$

$$\frac{\partial}{\partial t}(\rho \omega) + \frac{\partial}{\partial x_i}(\rho \omega u_i) = \frac{\partial}{\partial x_j} \left[\left(\mu + \frac{\mu_t}{\sigma_\omega} \right) \frac{\partial \omega}{\partial x_j} \right] + G_\omega - Y_\omega + D_\omega + S_\omega \quad (2.41)$$

where \tilde{G}_k represents the generation of turbulent kinetic energy the arises due to mean velocity gradients, G_ω is generation of ω , and Y_k and Y_ω represent the dissipation of k and ω due to turbulence. α_k and α_ω are the turbulent Prandtl numbers for k and ω respectively and S_ε and S_k are source terms defined by the user. D_ω is the cross-diffusion term which will be described below.

The term for production of turbulent kinetic energy, \tilde{G}_k is determined slightly differently from the other models and is defined as

$$\tilde{G}_k = \min(G_k, 10\rho\beta^* k\omega)$$

where G_k is defined the same way as described in the previous models.

The term for the production of ω , G_ω is defined as

$$G_\omega = \frac{\alpha}{\nu_t} G_k \quad (2.42)$$

The terms for the dissipation of k and ω due to turbulence, Y_k and Y_ω , are defined in a similar manner to that used in the standard model with the main difference being that f_{β^*} and f_β are both considered constants with a value of 1.

The turbulent viscosity is computed in a different way from that used in the standard model and is given by;

$$\mu_t = \frac{\rho k}{\omega} \frac{1}{\max\left[\frac{1}{\alpha^*}, \frac{SF_2}{a_1 \omega}\right]} \quad (2.43)$$

where S is the strain rate magnitude and α^* is the damping coefficient calculated using equation (2.35). The turbulent Prandtl numbers which were constant in the standard model are equated below and incorporate the blending functions F_1 and F_2 . Blending functions have been added to the SST model to ensure that the model equations behave appropriately in both near wall and far field zones.

$$\sigma_k = \frac{1}{F_1/\sigma_{k,1} + (1-F_1)/\sigma_{k,2}} \quad (2.44)$$

$$\sigma_\omega = \frac{1}{F_1/\sigma_{\omega,1} + (1-F_1)/\sigma_{\omega,2}} \quad (2.45)$$

where;

$$F_1 = \tanh(\Phi_1^4) \quad F_2 = \tanh(\Phi_2^2)$$

The cross diffusion term, D_ω blends the standard k-epsilon model and the standard k-omega model and is defined as

$$D_\omega = 2(1-F_1)\rho\sigma_{\omega,2} \frac{1}{\omega} \frac{\partial k}{\partial x_j} \frac{\partial \omega}{\partial x_j} \quad (2.46)$$

The constants specific to the SST k-omega model are defined as

$$\sigma_{\omega,1} = 2.0, \quad \sigma_{\omega,2} = 1.168, \quad \sigma_{k,1} = 1.176, \quad \sigma_{k,2} = 1.0, \quad a_1 = 0.31$$

2.3.3 Detached Eddy Simulation (DES) Model

The detached Eddy simulation (DES) model is a cross between the Large Eddy Simulation (LES) and Reynolds Averaged Navier Stokes (RANS) coupling modeling

approach. This model is generally used when it is advantageous to combine the RANS modeling approach with the LES approach when the use of the LES is determined to be too computationally expensive. In this case, with a large mesh size, the DES approach is significantly less expensive than an LES approach, but more expensive than RANS. In FLUENT, the DES model as proposed by Shur et al. (1999) is based on the single-equation Spalart-Allmaras (1992) approach.

An unsteady RANS version of the Spalart-Allmaras (1992) model and a filtered version of the same model are combined to create two regions within the flow domain. In the high-Re regions where large turbulence scales play a dominant role an LES model based on a one-equation sub-grid model is used by the DES model. In areas where viscous effects are dominant, such as near wall regions, the RANS model is used.

The DES model uses the single equation Spalart-Allmaras model that has one transport equation as follows;

$$\frac{\partial}{\partial t}(\rho\tilde{v}) + \frac{\partial}{\partial x_i}(\rho\tilde{v}u_i) = G_v + \frac{1}{\sigma_{\tilde{v}}} \left[\frac{\partial}{\partial x_i} \left\{ (\mu + \rho\tilde{v}) \frac{\partial \tilde{v}}{\partial x_j} \right\} + C_{b2} \left(\frac{\partial \tilde{v}}{\partial x_j} \right)^2 \right] - Y_v + S_{\tilde{v}} \quad (2.47)$$

where G_v and Y_v are the production and destruction of turbulent viscosity, C_{b2} and $\sigma_{\tilde{v}}$ are constants and $S_{\tilde{v}}$ is a user defined source term. Turbulent kinetic energy (k) is not calculated in the Spalart-Allmaras method and therefore when considering the stresses for the Boussinesq approximation, the last term in equation 2.11 is disregarded. Turbulent viscosity is calculated from equation 2.48.

$$\mu_t = \rho\tilde{v}f_{v1} \quad (2.48)$$

where

$$f_{v1} = \frac{\left(\frac{\tilde{v}}{\nu}\right)^3}{\left(\frac{\tilde{v}}{\nu}\right)^3 + C_{v1}^3}$$

The main difference in the model proposed by Spalart and Allmaras (1992) is in calculating the turbulent production and destruction from the transport equation (2.47). The Spalart-Allmaras model has the following equation for calculating the production of turbulence.

$$G_v = C_{b1} \rho \tilde{v} \left(S + \frac{\tilde{v}}{\kappa^2 d^2} f_{v2} \right) \quad (2.49)$$

where

$$f_{v2} = 1 - \frac{\left(\frac{\tilde{v}}{\nu}\right)}{1 + \left(\frac{\tilde{v}}{\nu}\right) f_{v1}}$$

The destruction term is calculated by;

$$Y_v = C_{w1} \rho f_w \left(\frac{\tilde{v}}{d} \right)^2 \quad (2.50)$$

where

$$f_w = g \left[\frac{1 + C_{w3}^6}{g^6 + C_{w3}^6} \right]^{1/6} \quad \text{and} \quad g = \frac{\tilde{v}}{\tilde{S} \kappa^2 d^2} + C_{w2} \left(\left(\frac{\tilde{v}}{\tilde{S} \kappa^2 d^2} \right)^6 - \frac{\tilde{v}}{\tilde{S} \kappa^2 d^2} \right)$$

A new length scale is defined for the DES model for all of the above equations. A new length scale, \tilde{d} is substituted for every variable d , and defined as;

$$\tilde{d} = \min(d, C_{des} \Delta) \quad (2.51)$$

where Δ is the grid spacing and is from the largest grid space in the x, y, or z directions, and the constant C_{des} is equal to 0.65.

2.3.4 Large Eddy Simulation (LES) Model

Unlike the Reynolds-averaged Navier Stokes (RANS) equation method, LES uses filtered Navier Stokes equations. Filtering the equations is a procedure by which the eddies with a scale smaller than the filter width (grid spacing) are filtered out leaving equations that model the dynamics of large scale eddies only. The LES model directly resolves large eddies in a time dependent simulation using the filtered equations essentially modeling less turbulence (and calculating more) thereby decreasing the inaccuracies created by modeling turbulence in small scales. In general these large eddies are similar in size to the characteristic length of the mean flow. Smaller Eddies that are usually responsible for dissipation of turbulent kinetic energy are “filtered” depending on the mesh size in FLUENT and modeled separately. The reason to use this type of modeling is due to the following reasons; large eddies are dictated by the geometries and boundary conditions of the flow involved and therefore become more problem dependent, small eddies tend to be more isotropic and less dependent on geometry making them more universal. Finer grid densities are required for LES models than the RANS models making the LES model computationally much more expensive. High-Re flows require large CPU costs. However a coarse near wall mesh coupled with wall functions can reduce the cost. Careful consideration must be taken into the discretization schemes, as higher order models must be used to achieve accurate results.

The filtering process is first achieved by defining the filtered variable (represented by an overbar)

$$\bar{\phi}(x) = \int_D \phi(x') G(x, x') dx' \quad (2.52)$$

where D is the fluid domain, and G is the filter function that determines the scale of the resolved eddies. The default filtering operation in the finite volume discretization uses the following equation.

$$\bar{\phi}(x) = \frac{1}{V} \int_V \phi(x') dx', \quad x' \in V \quad (2.53)$$

Here, V is the volume of the cell, and the filter function G is defined as

$$G(x, x') = \begin{cases} 1/V, & x' \in V \\ 0, & x' \text{ otherwise} \end{cases} \quad (2.54)$$

The Navier Stokes equation can be filtered in terms of the new filtered variables. The Smagorinski-Lilly (1963) version of the LES model has been used and the eddy viscosity is defined by

$$\mu_t = \rho L_s^2 |\bar{S}| \quad (2.55)$$

L_s is the mixing length for subgrid scales defined as

$$L_s = \min(\kappa d, C_s V^{1/3}) \quad (2.56)$$

where κ is the von Karman constant, d is the distance closest to the wall and C_s is the Smagorinsky constant. The rate of strain is defined as

$$|\bar{S}| \equiv \sqrt{2\bar{S}_{ij}\bar{S}_{ij}} \quad (2.57)$$

Lilly (1992) derived a value of 0.17 for C_s however it gave inaccurate results near solid boundaries due to the damping of large scale fluctuations. A value of 0.1 has been found to give the most accurate universal results. Details of this and the validation of this model are given in work by Kim (2004).

2.4 Radiation Model

The presence of a temperature gradient is required in order for heat transfer by conduction or convection to occur. Heat transfer by thermal radiation is extremely important to consider in many modeling cases such as the case being investigated here. This section will discuss the thermal radiation that is apparent in this project and the models used to calculate the radiant heat transfer in the domain.

FLUENT offers five radiation models; Discrete Transfer Radiation Model (DTRM); P-1 Radiation Model; Rosseland Radiation Model; Surface to Surface (S2S) Radiation Model; and Discrete Ordinates (DO) Radiation Model. The optical thickness of the medium (which is a product of the absorptivity (a) and the mean beam length (L)) must be considered when choosing the type of radiation model. The absorptivity of the medium in the present study is the emissivity of the air of the atrium and mean beam length for an atrium would be the length (the longer dimension) of the atrium. Typically the Rosseland and P-1 models are used for $aL > 1$ with Rosseland operating better for optically thicker mediums. The Rosseland model doesn't account for wall emissivity as it uses a temperature slip condition at the walls, and therefore it will not be further considered. For optically thin scenarios ($aL < 1$), the DTRM and DO model should be used although they are both considerably more computationally expensive to use. The DO model is the only model to account for diverse types of semi-transparent walls, and is also the only model that allows for specular and partially specular reflection reflection (dust-free or dusty mirrors). It is also the only model that allows for the calculation of non-gray radiation using a gray band model.

The radiative transfer equation (RTE) for scattering, absorbing and emitting mediums at a position \vec{r} and in the direction \vec{s} is defined by;

$$\frac{dI(\vec{r}, \vec{s})}{ds} + (a + \sigma_s)I(\vec{r}, \vec{s}) = an^2 \frac{\sigma T^4}{\pi} + \frac{\sigma_s}{4\pi} \int_0^{4\pi} I(\vec{r}, \vec{s}') \Phi(\vec{s} \cdot \vec{s}') d\Omega' \quad (2.58)$$

where \vec{r} = position vector

\vec{s} = direction vector

\vec{s}' = scattering direction vector

s = path length

a = absorption coefficient

n = refractive index

σ_s = scattering coefficient

σ = Stefan-Boltzmann Constant ($5.672 \times 10^{-8} \text{ W/m}^2 \text{ -K}^4$)

I = radiation intensity, which depends on position (and direction)

T = local temperature

Φ = phase function

Ω' = solid angle

The radiative heat transfer equation is illustrated in Figure 2-2 below.

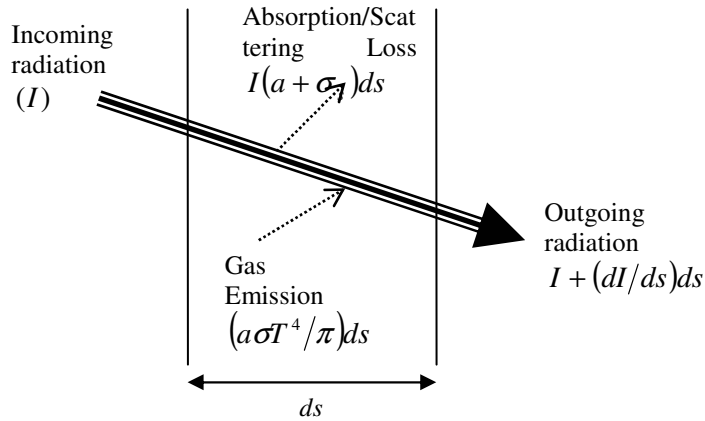


Figure 2-2 Radiative Heat Transfer

As explained above there are several radiation models available in FLUENT however as the main purpose of this thesis is to investigate the effects of different turbulent models, the P-1 radiation model was selected based on the above characteristics and it will be discussed in the following section.

2.4.1 P1 Radiation Model

The P-1 model was used to model the radiation in this project. It uses the RTE equation which is simple to solve using little CPU expense (power and time) and allows for scattering. These are two of its advantages over the other models. Some limitations to this model are that it assumes all surfaces are diffuse (which is a common limitation among most radiation models), it assumes gray radiation, for complex geometries with

small optical thicknesses accuracy can be reduced, and it tends to over-predict fluxes from localized heat sources or sinks. Since none of these limitations will limit the accuracy in any of the models being tested here, the P-1 was selected for use.

The P-1 radiation model is derived from the P-N radiation model and is the simplest form of this model (Fluent, 2006). The radiative heat flux is defined in equation (2.59).

$$q_r = \frac{-1}{3(a + \sigma_s) - C\sigma_s} \nabla G \quad (2.59)$$

where a is the absorption coefficient, σ_s is the scattering coefficient, G is the incident radiation and C is the linear-anisotropic phase function coefficient. The transport equation for G is defined by equation 2.60 with the parameter Γ which is defined in equation 2.60.

$$\nabla \cdot (\Gamma \nabla G) - aG + 4a\sigma T^4 = S_G \quad (2.60)$$

$$\Gamma = \frac{1}{3(a + \sigma_s) - C\sigma_s} \quad (2.61)$$

In equation 2.60, S_G is a user defined radiation source and the Stefan-Boltzmann constant is again defined by σ . Using equations 2.59 and 2.60 an expression for $-\nabla \cdot q_r$ is obtained that can be used in the energy equation to account for the absorption, emission and scattering of incident radiation in media as well as the radiation of heat sinks and sources.

$$-\nabla \cdot q_r = aG - 4a\sigma T^4 \quad (2.62)$$

As mentioned earlier, the P-1 model accounts for scattering and the linear-anisotropic phase function coefficient (C) is how it is accounted for.

$$\Phi(\vec{s}' \cdot \vec{s}) = 1 + C \vec{s}' \cdot \vec{s} \quad (2.63)$$

where \vec{s} is the unit vector in the direction of scattering, \vec{s}' is the unit vector in the direction of incident scattering. The linear anisotropic phase function is a property of the fluid and ranges from -1 to 1. More radiant energy is scattered forward than backward for a negative value of C , and the opposite is true for a positive value of C . Isotropic scattering occurs at a value of 0.

In order to get the boundary condition for incident radiation the following equations are considered.

$$q_r \cdot \vec{n} = -\Gamma \nabla G \cdot \vec{n} \quad (2.64)$$

$$q_{r,w} = -\Gamma \frac{\partial G}{\partial n} \quad (2.65)$$

The following boundary conditions are then used to compute the radiative heat flux.

$$I_w(\vec{r}, \vec{s}) = f_w(\vec{r}, \vec{s}) \quad (2.66)$$

$$f_w(\vec{r}, \vec{s}) = \varepsilon_w \frac{\sigma T_w^4}{\pi} + \rho_w I(\vec{r}, -\vec{s}) \quad (2.67)$$

where ρ_w is the wall reflectivity. The angular dependence is eliminated using the Marshak boundary condition given in equation 2.67.

$$\int_0^{2\pi} I_w(\vec{r}, \vec{s}) \vec{n} \cdot \vec{s} d\Omega = \int_0^{2\pi} f_w(\vec{r}, \vec{s}) \vec{n} \cdot \vec{s} d\Omega \quad (2.68)$$

Executing this integral, substituting equations 2.66 and 2.67 and considering that all walls are diffuse grey ($\rho_w = 1 - \varepsilon_w$) the following equation is used to compute for the incident radiation boundary conditions and the for the energy equation.

$$q_{r,w} = -\frac{\varepsilon_w}{2(2 - \varepsilon_w)} (4\sigma T_w^4 - G_w) \quad (2.69)$$

Flow inlets and outlet heat flux calculations are calculated in a similar fashion to the procedure described above. Used defined emissivity values for inlets and outlets are required or a default value of 1 is given.

2.4.1.1 Solar Load Model

The radiation effects from the sun's rays that enter the computational domain can be calculated by the solar load model. It is important to simulate the solar loading of the atrium as much of the radiation effects in the room are due to the heat fluxes that will occur from the solar radiation entering through the glass windows. This heat transfer can be a burden in the summer as there could be too much energy entering through the window but could also save on heating costs during cooler months and it is important to recognize the effects of this phenomenon.

There are two options available in FLUENT for the solar load model; the solar ray-tracing, and DO irradiation. The ray-tracing method is very practical and efficient as it applies solar loads as heat sources in the energy equations. The DO irradiation allows the user to input beam direction and intensity parameters to the DO radiation model and since the P-1 radiation model has been selected for use, the DO irradiation option will not be used. A solar calculator is also available in FLUENT to calculate the beam direction and irradiation. The solar calculator can be used to find the sun's location in the sky when given inputs of time date and global position.

Chapter 3 – Computational Fluid Dynamics

This chapter describes the fundamentals of computational fluid dynamics (CFD). Background information on CFD and the finite volume method, the solver parameters for the commercial CFD software and the post-processing techniques will be explained in the following sections.

3.1.1 CFD Background

Computational fluid dynamics (CFD) uses numerical methods to solve and analyze problems that involve fluid flows. The governing equations discussed above have been solved with respect to the specified boundary conditions using the finite volume method as implemented in the commercial CFD code FLUENT.

There are three components in CFD analysis; the pre-processor, the solver, and the post-processor. Preprocessor is defined as a program that processes input data to produce output that is used as an input to the processor. In the present study, the preprocessor being used is Gambit 2.3.16 (2007). Gambit was used to create the geometry of the system being considered and subdivide the domain into elements which as a whole constitute the mesh or grid. The solution of the flow is later solved at the center of each of these volumes by the solver. The preprocessor also defines general surface types (for example - inlet/outlet areas) to regions of the domain.

The solver discretizes the differential equations converting them to algebraic equations that can be solved numerically using the finite volume method. The finite volume method is discussed subsequently in this chapter in further detail. Finally the post-processor is a tool that allows the interpretation of the solution in the form of graphs,

plots, and charts. FLUENT is used for both the solver and the post-processor in the present work. Microsoft Excel is also used as a post processor for making graphs and charts to be presented in this report.

Jones and Whittle (1992) describe in detail the application of CFD to building environmental design, as well as the technical issues associated and potential of the techniques involved in these techniques. Figure 3-1 shows the general method of using CFD in the present study.

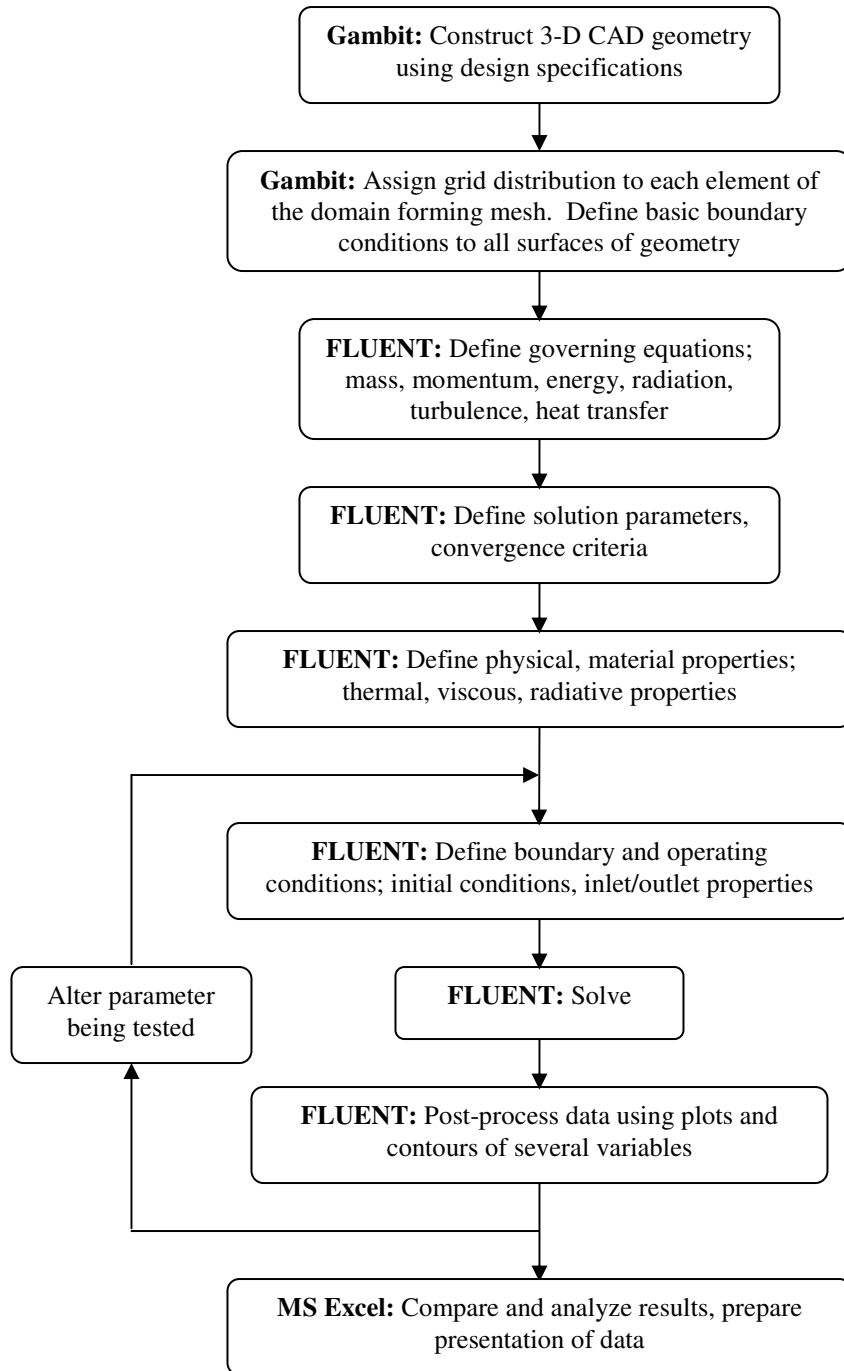


Figure 3-1 Flowchart of method used for CFD application

3.1.2 Finite Volume Method

The finite volume method is a numerical procedure for obtaining solutions to many of the problems encountered in air flow simulation. FLUENT uses this numerical method for solving partial differential equations that calculates the values at discrete places on a mesh. After the domain has been divided into discrete control volumes forming a computational grid or mesh, the governing equations are integrated over the individual control volumes forming surface integrals using Gauss' divergence theorem. These terms are evaluated as the fluxes at the surface of each finite volume and the fluxes are conserved throughout the domain. The finite volume method is described in more detail throughout this chapter.

3.1.3 Solution Method

There are two solvers for use in FLUENT; the segregated solver and the coupled solver. The segregated solver has been used as the solution algorithm in the present study. The coupled solver was not considered as it solves the governing equations simultaneously requiring higher computational expense. Because the governing equations are non-linear (coupled) numerous iterations of the solution loop must be completed. The coupled solver is more ideal for high-velocity flows which is unnecessary in the current modeling and initial tests on the Concordia-like atrium revealed that convergence could be reached using the segregated solver.

The segregated solver resolves the governing equations sequentially and obtains a converged solution by performing several iterations of the solution loop as the governing equations are coupled and non-linear. In the first iteration, the properties of the working

fluid are based on the initialization solution (user defined initialization) and for every following iteration the fluid properties are updated based on the current solution. Current values for pressure and face mass fluxes are used to solve the three momentum equations in order to update the velocity field. These velocities may not satisfy the continuity equation locally and therefore an equation for the pressure correlation derived from the continuity and linearized momentum equations is solved to obtain corrections to the pressure and velocity fields and the face mass fluxes. Equations for scalars such as turbulence, energy and radiation are solved using the updated values of the other variables. Finally a check for the convergence of the equation set is made. If the solution is converged, the iteration process is stopped and if convergence criteria has not been met, then the iteration process is continued. Figure 3-2 shows the iterative steps.

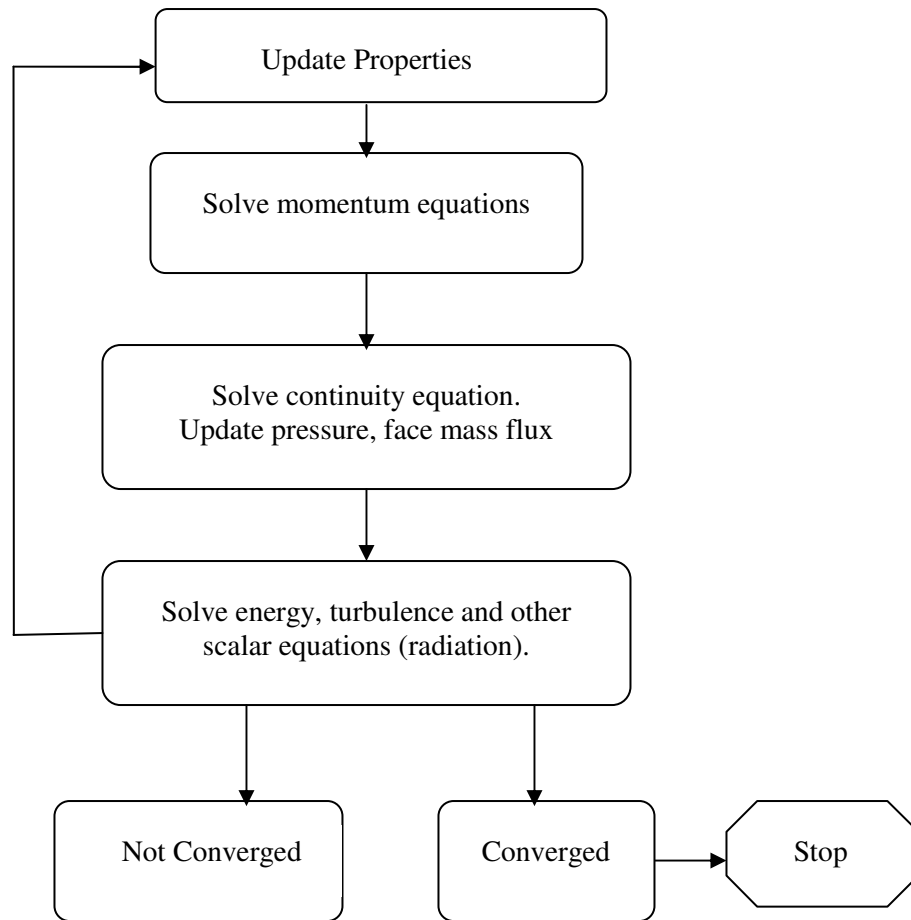


Figure 3-2 Overview of segregated solution method

The segregated solver in FLUENT provides three algorithms for pressure-velocity coupling; SIMPLE, SIMPLEC and PISO. SIMPLE and SIMPEC are quite similar although SIMPLEC can perform better for more complicated flows. Also, it is recommended that when using meshes with a high degree of distortion the PISO algorithm can outperform the other two methods. As the SIMPLE algorithm is the most

basic algorithm, it was chosen for all simulations run in the current work. The SIMPLE algorithm relates the velocity and pressure corrections to achieve mass conservation and to obtain the pressure field. A pressure is assumed in order to solve the momentum equations then a pressure-correction equation and flux-correction equation are used to ensure the continuity is satisfied for each iteration.

All equations solved using the pressure based solver have under-relaxation factors associated with them. The default values were used to start the model, and then decreased according to the residuals which were plotted for all iterations. Each model typically started with the suggested under-relaxation factors for pressure, momentum, energy, turbulence values, and radiation of 0.3, 0.1, 0.85, 0.8 and 0.8 respectively. These values were altered as needed to meet the convergence criteria.

Overly conservative under-relaxation factors, number of computational cell and grid orientation are a few factors that can slow the convergence of a solution. Convergence can be based on residual levels, or other scalar quantities such as heat transfer coefficients or drag. In the present study, several quantities were monitored, but the converged solution was based on the residual levels. The residuals were monitored to be sure that the residual decreased and stayed below the convergence criteria (10^{-3} for all models except energy and radiation which have the criteria of 10^{-6}) for a substantial number of iterations.

3.1.4 Discretization

Once the solution has been initialized with estimated initial flow variables (velocity, temperature etc.) and inputs for boundary conditions and physical properties, a control-volume-technique used in FLUENT converts the governing equations into algebraic equations to be solved numerically.

In order to ensure that flow variables are conserved over each cell or control volume, the governing equations must first be integrated over the control volume. To demonstrate this, a general steady state transport for any flow variable ϕ , can be expressed as equation 3.1.

$$\nabla(\vec{v}\rho\phi) = \nabla(\Gamma\nabla\phi) + S_\phi \quad (3.1)$$

where \vec{v} is a velocity vector, ρ is the density, ϕ is a scalar variable, and Γ is the transport coefficient. Equation 3.2 is obtained by integrating equation 3.1 over a control volume (CV).

$$\int_{CV} \nabla(\vec{v}\rho\phi) dV = \int_{CV} \nabla(\Gamma\nabla\phi) dV + \int_{CV} S_\phi dV \quad (3.2)$$

This integral form of the equation can now be transformed to a local form using Gauss' theorem of divergence. Again considering the volume in **Error! Reference source not found.**, Gauss' theorem is expressed in equation 3.3.

$$\int_{CV} \nabla(\vec{M}) dV = \int_A \vec{M} \cdot \vec{n} dA \quad (3.3)$$

where the value \vec{M} is a sufficiently smooth vector field defined by the volume V, are of the surface A and a unit vector (n) normal to the surface. Gauss' theorem can be applied to equation 3.2 and the following formula is obtained.

$$\int_S (\vec{v}\rho\phi) \cdot \vec{n} dA = \int_S (\Gamma\nabla\phi) \cdot \vec{n} dA + \int_{CV} S_\phi dV \quad (3.4)$$

FLUENT must have the equation in an algebraic form and therefore the discretized form of the equation for one cell becomes;

$$\sum_f^{N_{faces}} \rho_f \phi_f \vec{v}_f \cdot \vec{A}_f = \sum_f^{N_{faces}} \Gamma_\phi (\nabla \phi)_n \cdot \vec{A}_f + S_\phi V \quad (3.5)$$

where the subscript “ f ” refers to the face value of the variable.

Equation 3.5 allows each discrete value of the scalar quantity ϕ to be calculated for the entire domain and represented in the center of each cell of the mesh. The generation or consumption of the value ϕ within the volume is given by the last term in equation 3.2 and again in equation 3.5. The face values are required for convection terms in equation 3.5 and are interpolated from the center of the cell using an upwind scheme. The diffusion terms in equation 3.5 are always central differenced and second order accurate, however FLUENT offers several upwind schemes to derive the face value quantities in the upwind (upstream) cell relative to the direction of the normal velocity (\vec{v}_n in equation 3.5). In the present work the first order upwind scheme was used. This scheme assumes that the cell center value of any field variable is the averaged value and this averaged cell value is equal to face values. Therefore the face value ϕ_f is set equivalent to the center value ϕ in the cell upstream.

When a higher order of accuracy is desired a multidimensional linear reconstruction approach to computing face values can be solved by using the 2nd order upwind scheme. This approach is described in further detail by Barth and Jespersen (1989). A Taylor series expansion of the solution at the cell center is completed to obtain

higher accuracy in the face values. The cell face value ϕ_f is now calculated from equation 3.6.

$$\phi_f = \phi + \nabla \phi \cdot \Delta \vec{s} \quad (3.6)$$

where ϕ is the value at the cell center, $\nabla \phi$ is the gradient in the upstream cell, and $\Delta \vec{s}$ is the displacement vector from the center of the upstream cell center to the face center.

The gradient is computed by equation (3.4).

$$\nabla \phi = \frac{1}{V} \sum_f^{N_{faces}} \tilde{\phi}_f \vec{A} \quad (3.4)$$

where the face values $\tilde{\phi}_f$ are averaged from the two adjacent cells of the face.

The above equations have now been related by cell center and face values, but the discretized equation will be non-linear regarding these variables. A linearized form of this equation is given in equation (3.5).

$$a_p \phi = \sum_{nb} a_{nb} \phi_{nb} + b \quad (3.5)$$

where the neighboring cells are referred to by the subscript “nb” and the linearized coefficients for ϕ and ϕ_{nb} are a_p and a_{nb} respectively.

In order to determine which scheme to select, an investigation of upwind schemes was undertaken for the 1x1x1 cavity study by Salat et al. (2004) described in Section 4.1.3. The realizable k-epsilon model was used for both the 1st order upwind scheme and the 2nd order upwind scheme models. Temperature and velocity profiles in the median plane at mid-height and mid-width are given in Figure 3-3 to Figure 3-6. A discussion of the results will be presented later in this report.

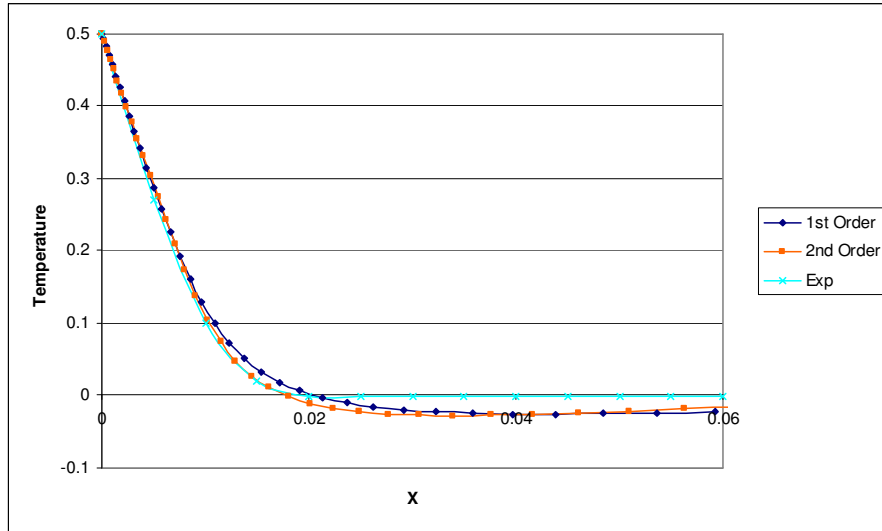


Figure 3-3 Temperature Profile at mid-height in the median plane

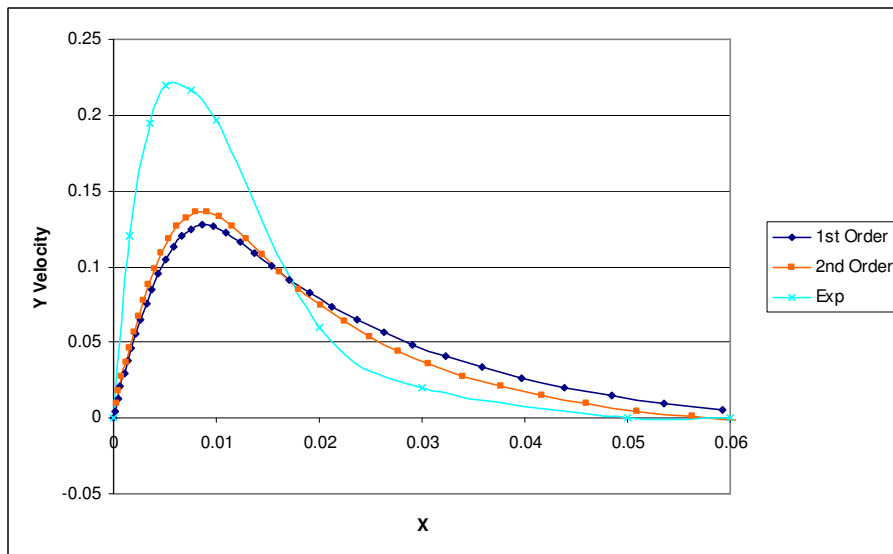


Figure 3-4 Velocity Profile at mid-height in the median plane

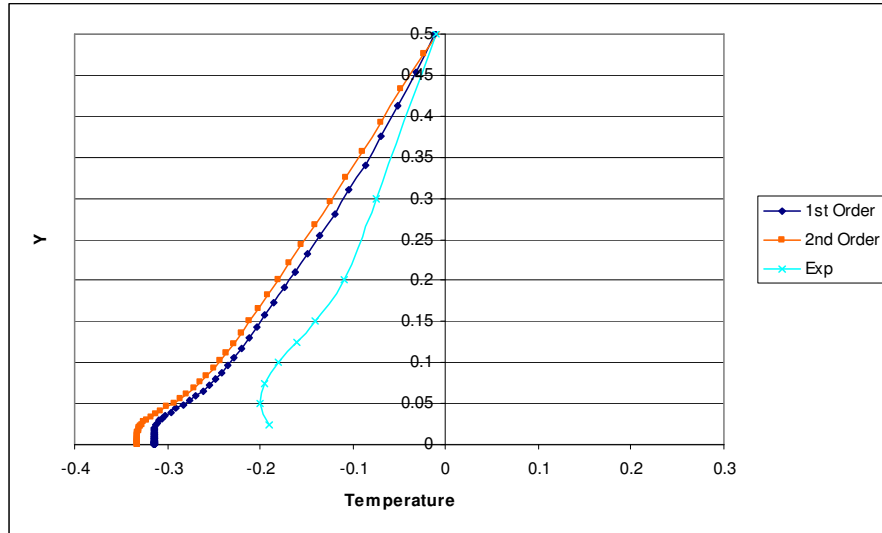


Figure 3-5 Temperature Profile at mid-width in the median plane

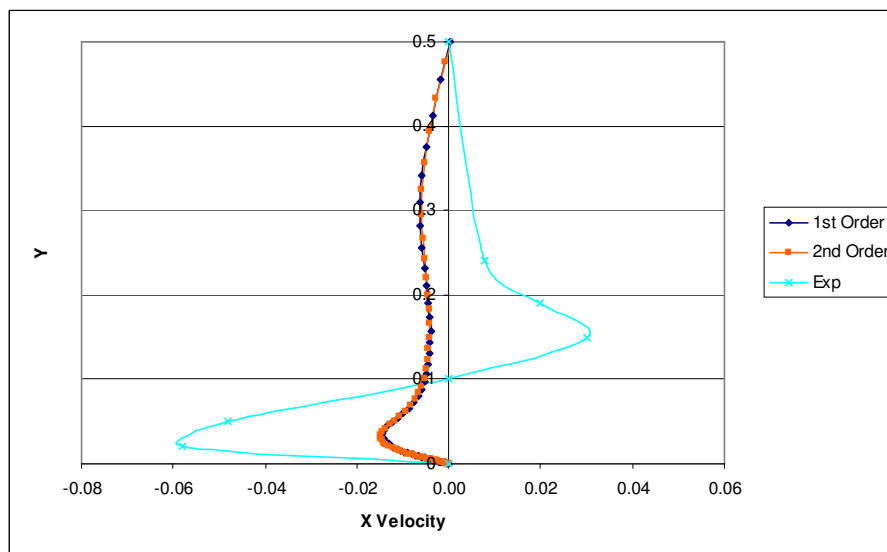


Figure 3-6 Velocity Profile at mid-width in the median plane

The results for both the 1st and 2nd order upwind differencing schemes give very similar results. Overall the 2nd order scheme gave improved results compared to the 1st order scheme in the temperature fields however it gave similar or inferior results to the 1st

order scheme results for velocity profiles at mid-height and mid-width. Also, the 2nd order model was far more computationally expensive as convergence took up to four times as long compared to the 1st order model. From these results it was decided that the 1st order differencing scheme gave adequate results considering the accuracy of the results and the computational costs.

Chapter 4 – Physical Models and Boundary Conditions

The main goal of this thesis is to evaluate several turbulence models and their ability to accurately simulate the flow in an atrium without large computational resources. Three flow situations are considered here. The physical models and boundary conditions for these situations will be discussed in this chapter. The first case being examined is a situation similar to that of the EV building at Concordia University and it will be described first. Since minimal experimental data for temperatures and velocities were available to compare to the computed results, two other situations for which extensive experimental results were available were used to confirm the modeled results. Firstly, the Annex 26 Atrium in Yokohama Japan was selected as it is of comparable size to the Concordia Atrium. Secondly, a 1m cubic cavity in which the effects of solar radiation were neglected was selected in order to gain further confidence in the accuracy of the results from the Concordia Atrium. These three models are described in the following sections.

Several tests were performed to justify the solutions including a grid sensitivity check and turbulence modeling tests. For the grid sensitivity check, several grids were used and run in FLUENT to determine a grid size that was fine enough to obtain a solution of acceptable accuracy, but not so fine that excessive computational demands were created.

4.1.1 Atrium in EV Building, Concordia University

The EV building at Concordia University houses several engineering departments and research facilities. It stands 17 floors high and encloses 5 identical atria, each atrium being 3 stories high. An outside view of the building is given in Figure 4-1. The south facing wall of the atrium is completely glass, the two perpendicular walls are solid and adjacent to the offices and the wall opposite the glass wall holds a circular staircase that opens to hallways connecting the offices.

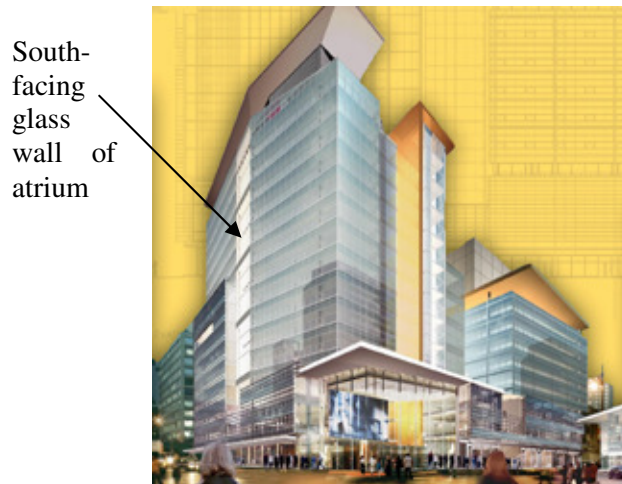


Figure 4-1 Outside view of EV building at Concordia University

The assumptions and boundary conditions that apply to the domain must be defined. This simplified domain is shown below in Figure 4-2. It is an approximate model of the Concordia Atrium in the EV building that disregards the staircase, any furniture, or any openings to the hallways. The dotted vertical and horizontal lines in the center of the geometry are the lines along which the results obtained with different turbulent models will be compared.

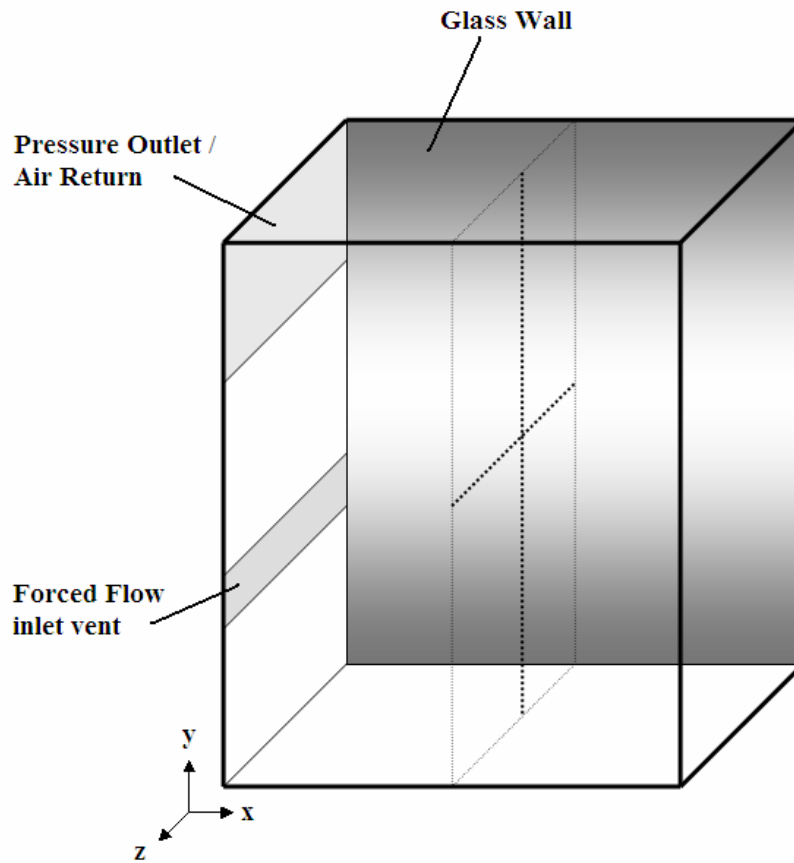


Figure 4-2 Three-Dimensional domain

4.1.1.1 Grid Generation

As described in section 3.1.1, the preprocessor used to create the meshes in the present study was Gambit 2.3.16 (2007). As the geometry for the Concordia-like atrium is simple and rectangular, a structured grid with an aspect ratio no more than 1.15 was used. The initial mesh created for this is shown in Figure 4-3. After initial work, it was realized that higher velocities would be occurring around the outside walls and low velocities were observed in middle of the x-y plane. A finer mesh was used at the

boundaries of the x-y domain which can be seen in the Figure 4-3. Higher grid densities were also used for velocity inlets and pressure outlets. Table 4-1 shows the number of nodes in each geometry, and Figure 4-3 to Figure 4-6 show the four grid densities used in the present study.

Table 4-1 Mesh densities of Grids 1 to 4

	Grid 1	Grid 2	Grid 3	Grid 4
# of Nodes	232,524	392,877	583,234	1,130,395

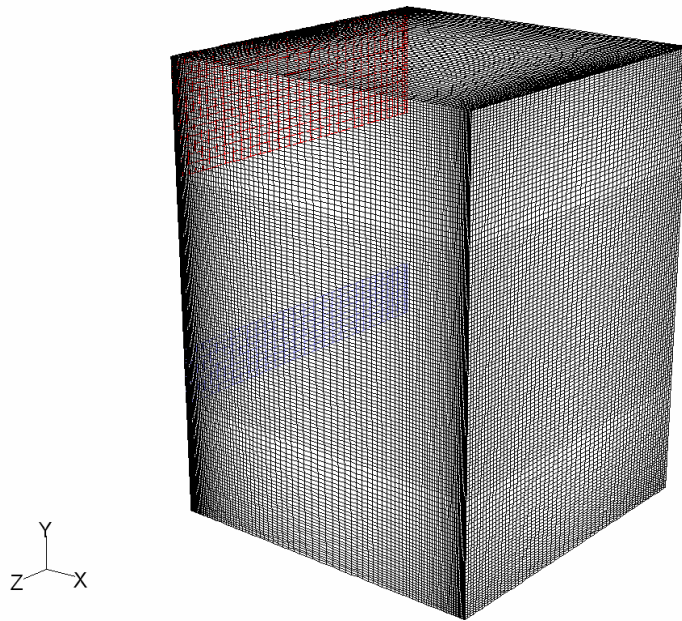


Figure 4-3 Concordia Mesh 1 with 232,524 nodes

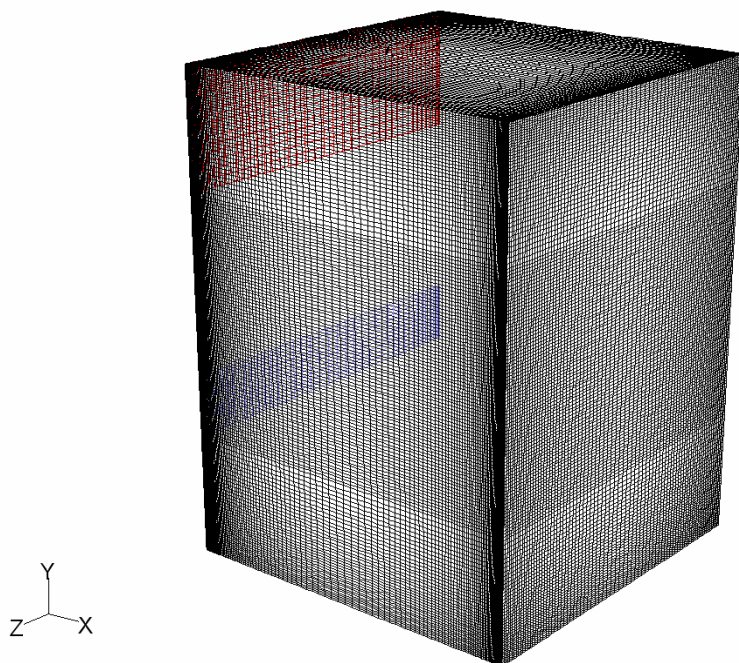


Figure 4-4 Concordia Mesh 2 with 392,877 nodes

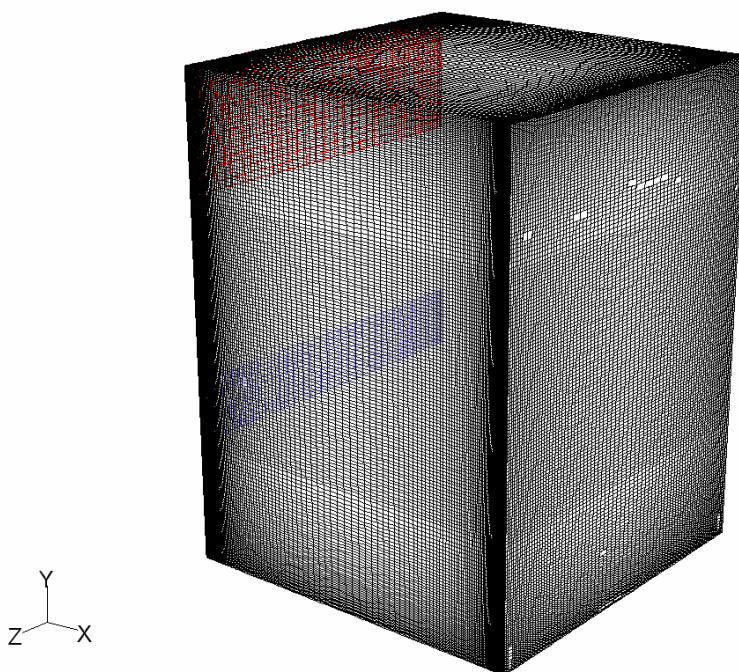


Figure 4-5 Concordia Mesh 3 with 583,234 nodes

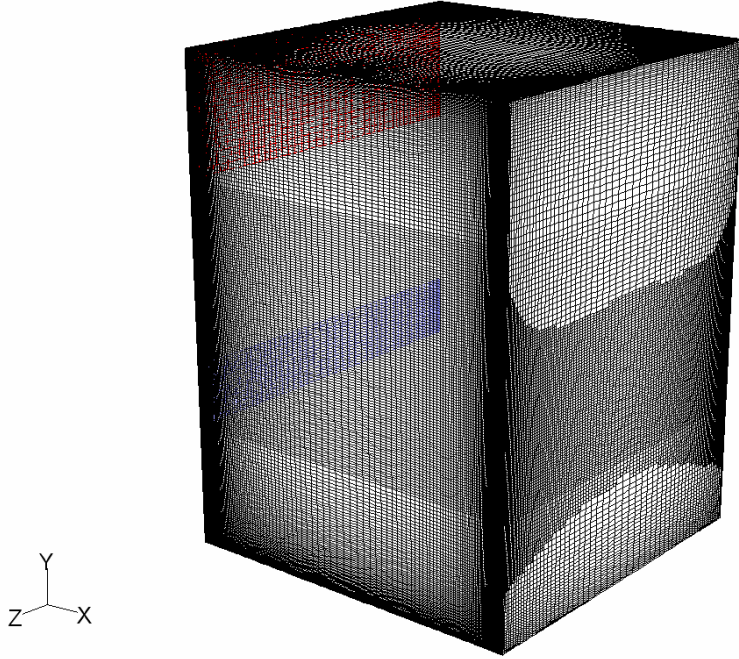


Figure 4-6 Concordia Mesh 4 with 1,130,395 nodes

In the near wall region there are very large gradients of the solution variables and therefore to achieve an accurate representation of the flow in this region it is important to have a high enough grid density. Once the grid has been imported into FLUENT a y^+ adaptation tool is used to adapt the grid in areas in which high velocities and gradients occur. The documentation states that the distance between a near wall cell centroid and the wall boundary is defined as the dimensionless distance y^+ . The equation for this distance is given in equation (4.1).

$$y^+ = \frac{\rho u_t y}{\mu} \quad (4.1)$$

The literature gives several acceptable y -plus values ranging from 5 to 50 for near wall turbulence modeling however the documentation states that for turbulence modelling a y^+ value of 10 is sufficient. The present study used this minimum value of 10.

A grid sensitivity check was implemented using the four grids mentioned above. Velocity and temperature profiles were recorded along the dotted vertical and horizontal lines shown in Figure 4-2. For each of the velocity and temperature profiles in Figures Figure 4-7 to Figure 4-10, the x-value with the largest difference in the corresponding y-values was noted. The percentage difference for these x-values can be seen in Tables Table 4-2 to Table 4-4 following each of the plots.

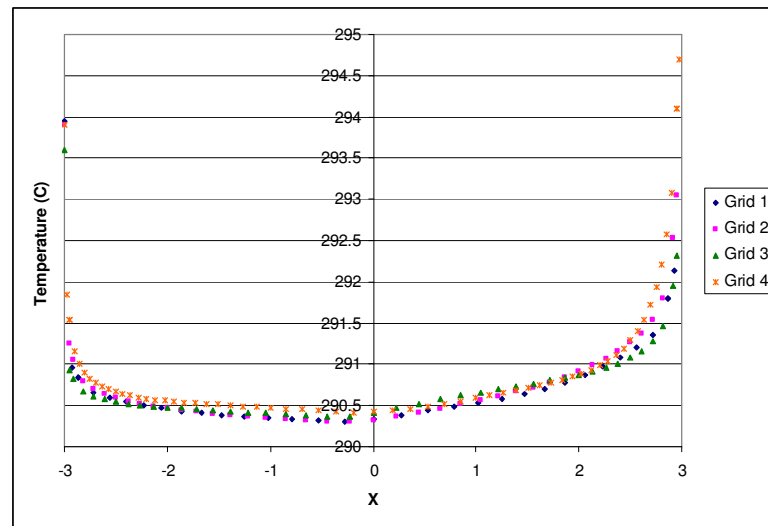


Figure 4-7 Horizontal temperature profile for several grid densities

Table 4-2 Percentage difference between horizontal temperature profiles for grids 1 to 4

	$-3 < X < -2$	$2 < X < 3$
Grid 1-2	0.304	0.229
Grid 2-3	0.088	0.027
Grid 3-4	0.175	0.284

Table 4-2 shows the percentage difference between the profiles as the grids increase in density. It can be seen that all grids are very similar in trend and magnitude for the horizontal temperature.

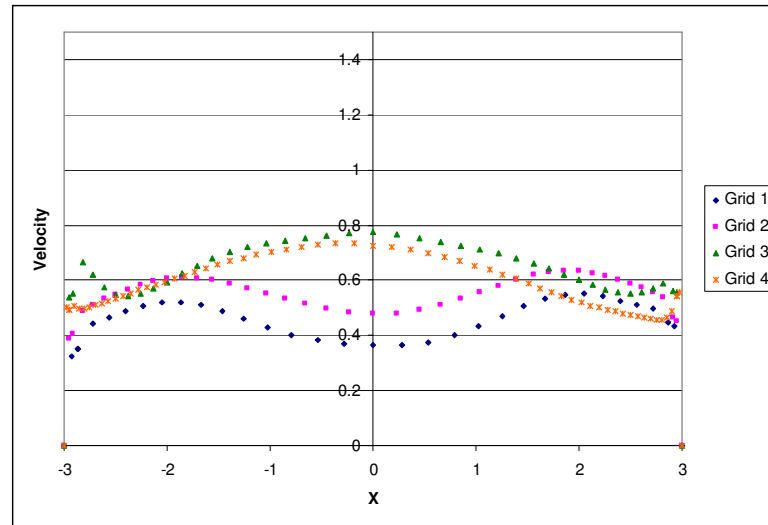


Figure 4-8 Horizontal velocity profile for several grid densities

Table 4-3 Percentage difference between horizontal velocity profiles for grids 1-4

	X = 0
Grid 1-2	23.4
Grid 2-3	38.3
Grid 3-4	6.5

Table 4-3 shows the percentage difference between the horizontal velocity profiles seen in Figure 4-8 at an x-value of 0. The two meshes with the least number of nodes (finest) share similar trends and the two meshes with the most number of nodes (most

coarse) share similar trends. At a value of $X=0$, where the largest difference in results arise, the meshes that give most similar results are the two finest grids. The high percentage differences can be attributed to the low velocities in this area with velocities ranging from 0.2 m/s to 0.8 m/s.

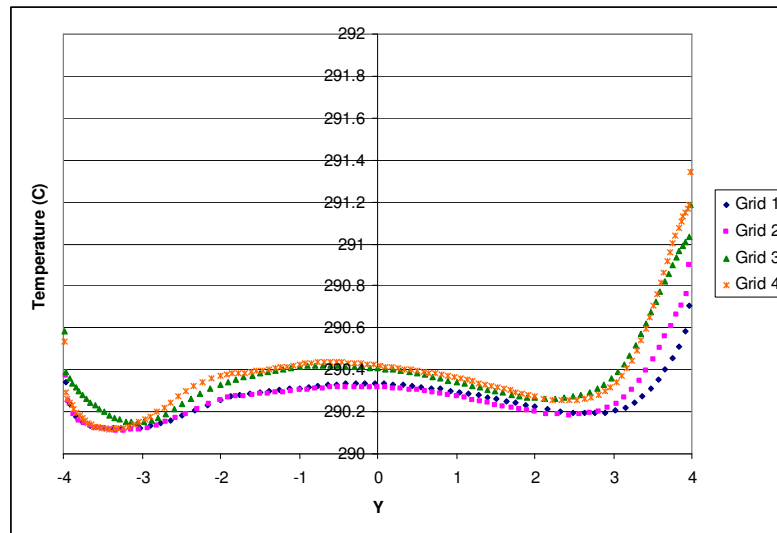


Figure 4-9 Vertical temperature profile for several grid densities

Table 4-4 Percentage difference between vertical temperature profiles for grids 1-4

	$-1 < Y < 0$	$3 < Y < 4$
Grid 1-2	0.004	0.033
Grid 2-3	0.039	0.089
Grid 3-4	0.004	0.035

Table 4-4 shows the percentage difference between the vertical temperature profiles as the grids increase in density. Similar to the horizontal temperature profiles, the

percentages are very low again due to the large values (290K to 292K). Again the two finest meshes are very close and the two coarsest meshes are very close.

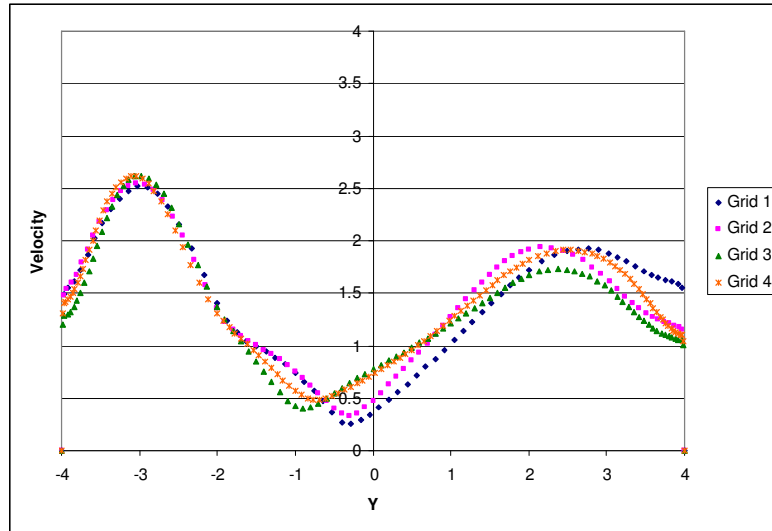


Figure 4-10 Vertical velocity profile for several grid densities

Table 4-5 Difference between vertical velocity profiles for grids 1-4

	$-1 < Y < 0$	$3 < Y < 4$
Grid 1-2	22.8	27.6
Grid 2-3	48.1	9.3
Grid 3-4	25.6	17.2

In the vertical velocity profile seen in Figure 4-10 all four grids give similar trends but the two main areas where they differ have been analyzed and the percentage difference is given in Table 4-5. Again the high percentages can be attributed to the low

velocities. The largest difference is seen between grids 2 and 3 because of the shift in the curve.

It was determined that the results obtained using grid 3 were close enough to those of grid 4 and also required significantly less computational expense than grid 4. Grids 1 and 2 also displayed similar results but the differences between grids 2 and 3 suggest the possibility that the mesh needed to be finest to capture accurate results. Based on the results, grid 3 was used to calculate results for all models of the Concordia-like atrium.

4.1.1.2 Walls

All wall boundaries excluding the glass wall, the forced flow inlet and the pressure outlet are considered opaque surfaces. Since the actual radiation values of the materials in the Concordia atrium were not given, realistic but approximate values were used for wall surfaces.

The ceiling and floor are both assumed insulated and therefore treated as adiabatic. The heat transfer to the wall boundary from a solid cell is therefore defined as;

$$q = k_{eff} \frac{\partial T}{\partial n} + q_{rad} = 0 \quad (4.2)$$

where k_{eff} is the effective thermal conductivity of the solid and n is the direction vector normal to the wall. Since the actual radiation values of the materials in the Concordia atrium were not available, realistic but approximate surface radiation values were used for wall surfaces, the floor and the ceiling.

The glass window was modeled as a semitransparent surface and radiation properties were obtained from the ASHRAE Fundamentals Handbook (2001). These properties account for glazing of the surface as well as the thickness.

4.1.1.3 Forced Flow Inlet and Pressure Outlet

The forced flow inlet was modeled as a velocity inlet as the air is being forced into the room mechanically. The flow is considered to be uniform and undeveloped and set to a temperature of 290K and a velocity magnitude of 4m/s which will be varied during testing. The inlet angle is originally set to 45 degrees but will also be varied during testing.

The return vent was modeled as a pressure outlet where the flow would be exiting at a 45 degree angle downward which is consistent with the actual atrium at Concordia. The dimensions of the supply and return can be seen in Figure 4-11.

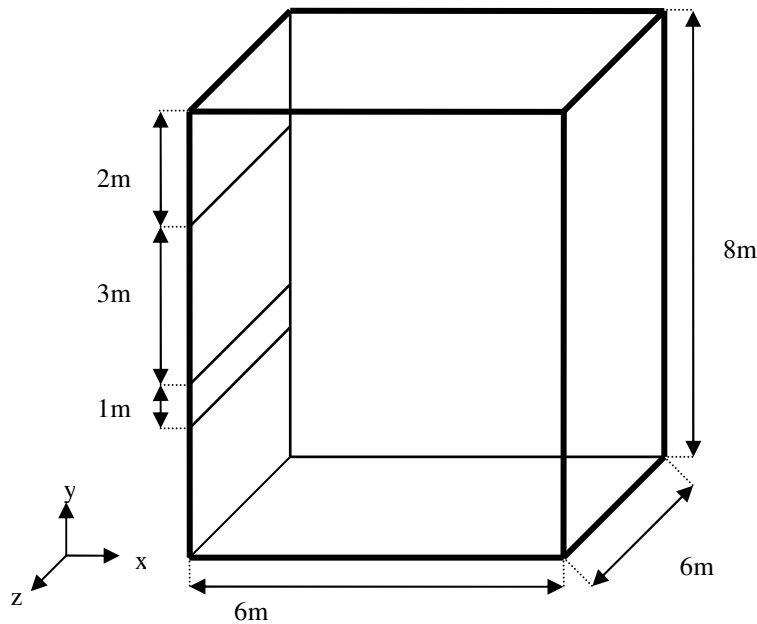


Figure 4-11 Dimensions of Concordia Atrium

4.1.1.4 Solar Loading

The sole purpose of having the large glass wall in the atrium is to allow sunlight to enter in the south facing glass wall to improve lighting and this also causes greater heat transfer into the building. It is important to be able to accurately predict the solar energy entering the atrium as the large glazing allows significant heat transfer into the building through solar radiation. The solar loading application available in FLUENT and described in section 2.4.1.1 allows an accurate calculation of the amount of solar and thermal energy entering through semitransparent surfaces.

The small amount of experimental data that was obtained for the atrium was taken on June 21 of 2006. This date and the global position of Montreal, Quebec, Canada (Longitude: -76.3, Latitude: 44.16, Time zone: -4) were entered into the solar calculator.

4.1.2 IEA Annex 26 Atrium

The atrium is located in Yokohama, Japan and was built for the purpose of validating simulations of large spaces as a part of a research program coordinated by IEA Annex 26 (Heiselberg et al. 1998). The atrium has three glass walls (south, east and west walls), a glass roof, and an insulated floor and north wall. Figure 4-12 shows a picture of the atrium and Figure 4-13 shows the dimensions of the atrium.



Figure 4-12 IEA Annex 26 Atrium, Yokohama, Japan

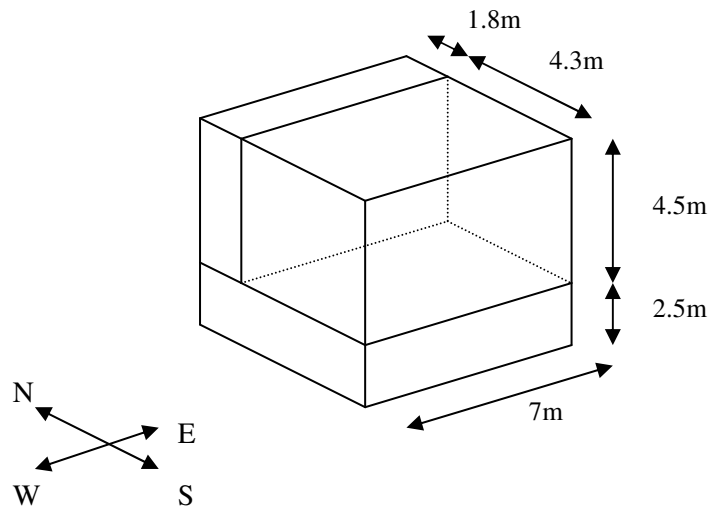


Figure 4-13 Dimensions of Annex 26 Atrium

Since the Annex 26 atrium is comparable in size to the Concordia-like atrium a similar grid distribution to that used in calculating the flow in the Concordia-like atrium was used. Since there is no mechanically forced air flow into or out of the Annex atrium, a

structured grid with more nodes near the walls was used since this area will have the largest gradients. The mesh can be seen in Figure 4-14.

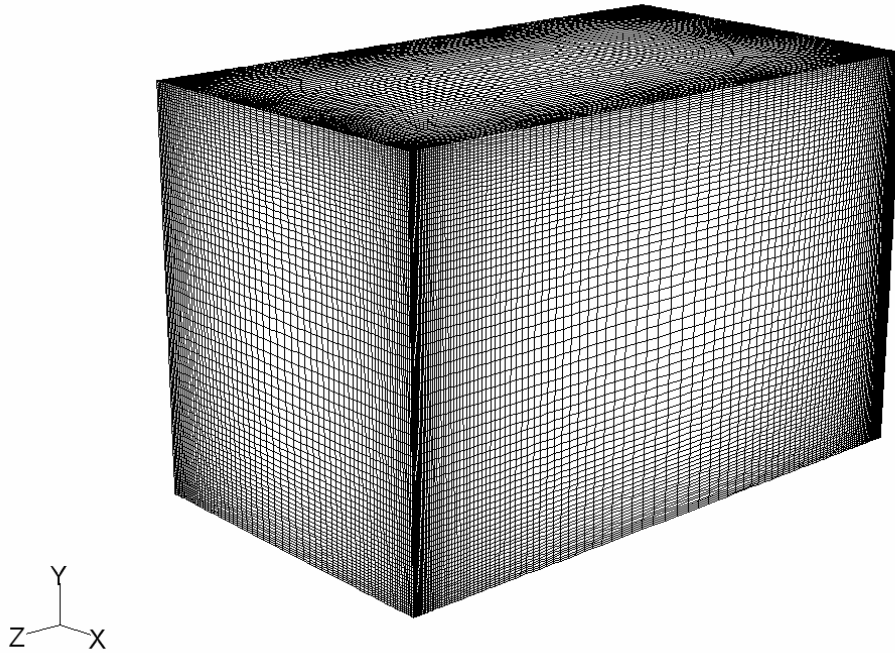


Figure 4-14 Annex 26 Atrium Mesh

Very little information was given for the boundary conditions of this atrium, and therefore radiation, and material properties similar to that used for the Concordia-like atrium were adopted. It can be seen in Figure 4-13 that there are areas outside of the atrium behind the north wall and below the floor. Only the inner part of the atrium was modeled and therefore experimental surface temperatures obtained from the study by Heiselberg et al. 1998 were used for the north wall and floor of the atrium to simulate the effects of the rooms adjacent to these surfaces.

The experimental data was collected on March 31, 1994 and collected without any ventilation and air conditioning. This date and the global position of Yokohama, Japan (Longitude: -139.28, Latitude: 35.27, Time zone: 9) were entered into the solar calculator.

4.1.3 1m Cubic Cavity

Salat et al (2004) experimentally and numerically investigated the natural convective flow that develops in a differentially heated cavity. The cavity had height $H=1\text{m}$, a width $W=H$ and a depth $D=0.32H$ with guard cavities of the same size on either side of the test cavity. A temperature difference between the opposite hot and cold walls of 15K was used, the hot wall being at 303 K and the cold wall being at 288 K . The upper and lower walls were considered adiabatic. A schematic view of the experimental setup is given in Figure 4-15.

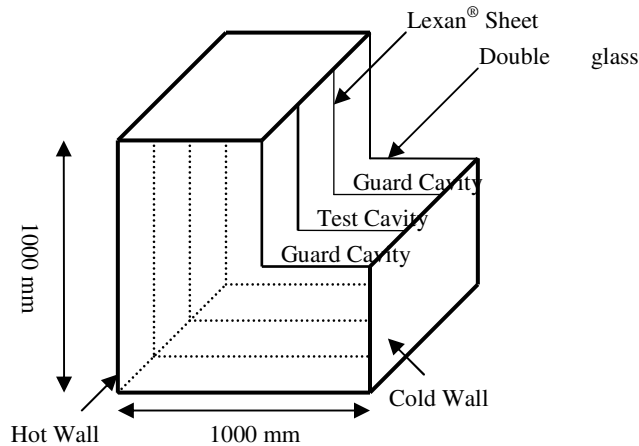


Figure 4-15 Dimensional domain of air filled cavity

Both 2D and 3D LES and 3D DNS calculations were performed for two scenarios; using adiabatic temperatures on the horizontal walls, and using experimentally measured

temperatures on the horizontal walls. The measurement protocol, methodology and results are well documented and can be found in Salat et al. (2004).

Although grid characteristics for the model used by Salat et al (2004) were not identified in the literature, a very fine mesh was applied to the domain as this study investigated the accuracy in calculating the near wall effects. The grid generated for this case can be seen in Figure 4-16.

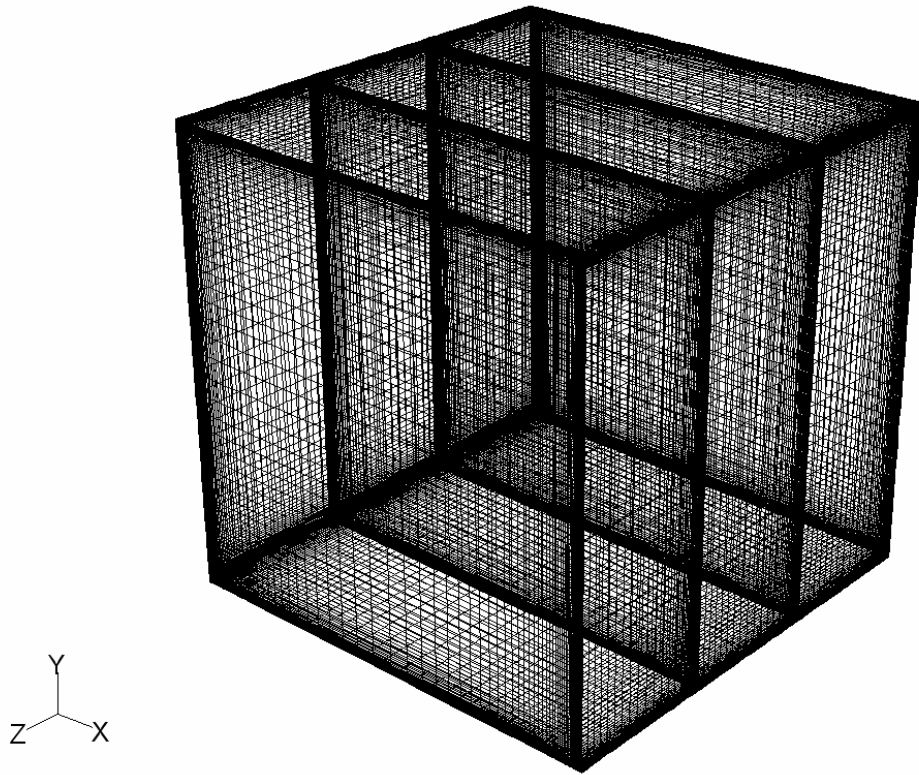


Figure 4-16 Mesh for air-filled cavity

The outer walls perpendicular to the z-axis were made of glass, and the inner walls perpendicular to the z-axis were made of Lexan[®] sheet. Properties for the Lexan[®] sheet were obtained from the product data sheet provided by GE Structured Products (1998). Other material properties were obtained from MatWeb (2002). Radiative

properties for materials were not given in the paper and had to be approximated and this could have affected results.

Chapter 5 – Results and Discussions

5.1 Introduction

In this chapter the validation of the numerical solution procedure will be confirmed by comparing experimental and numerical results produced Salat et al. (2004) with numerical results produced in this study using several turbulent models these being described in Chapter 2 –. Secondly, numerical results showing the difference in the results obtained using various turbulence models for the Concordia Atrium are presented and discussed. The effect of inlet flow angle and velocity for the Concordia Atrium are presented and the effects of external physical conditions (date and time) are also given. Finally, the numerical and experimental results from the paper by Salat et al. (2004) on the Annex 26 Atrium in Yokohama Japan are compared to numerical results derived using modeling techniques similar to those used in previous cases.

5.2 1m Cubic Cavity Results

In order to be sure that accurate modeling techniques were used in the modeling of the Concordia atrium, similar modeling techniques were applied to the case developed by Salat et al. (2004) that was described in Section 4.1.3. The experimental setup is shown in Figure 4-15. The experimental and numerical results and a comparison of the results are given here.

5.2.1 Temperature and Velocity Fields

Salat et al. (2004) first compared the horizontal wall temperature distributions of the top and bottom walls on the median plane ($y=0.5A_y$). Figure 5-1 shows the results obtained experimentally and numerically by Salat et al. as well as the numerical results obtained in the present study for a number of different turbulence models.

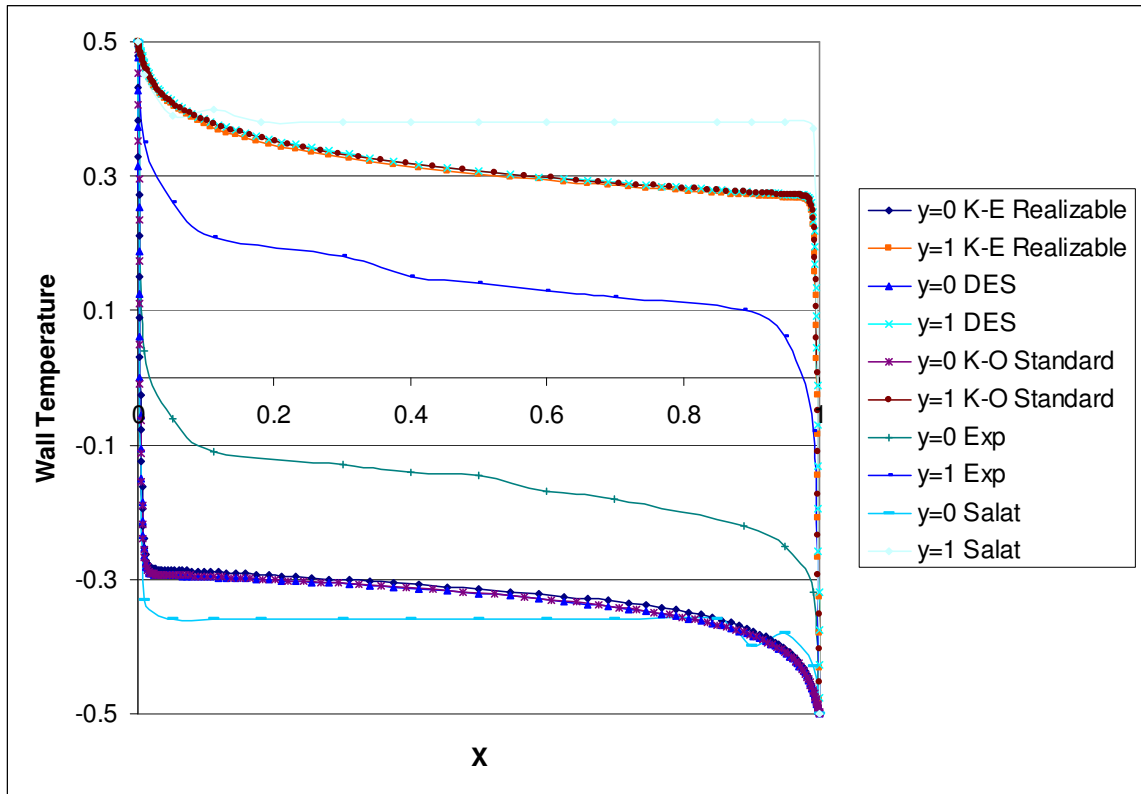


Figure 5-1 (Dimensionless) Temperature distribution on the cavity horizontal walls (from hot wall, $x=0m$ to cold wall, $x=1m$)

The experimental profiles were obtained from measurements very close to the cavity walls. The numerical data obtained by Salat et al. are similar to the numerical results obtained in the present study but the consistency and variation in wall temperature seem to more closely match results obtained in the present work. The difference between

the numerical and experimental results is most likely due to the fact that not all material properties and radiative properties were given for the walls of the cavity.

Figure 5-2 and Figure 5-3 compare the experimental and numerical results obtained by Salat et al. (2004) for dimensionless temperature and velocity at mid-height of the cavity, with the numerical results given by three turbulent models. The temperature results given by Salat et al. (2004) were in dimensionless form. The equation used to find the dimensionless temperature is as follows.

$$\text{Dimensionless Temperature} = \frac{T - T_{mean}}{T_H - T_C} \quad (5.1)$$

where T_H and T_C are the temperatures of the hot and cold walls (30°C and 15°C respectively), T_{mean} is the mean temperature ($[T_H + T_C]/2 = 22.5^\circ\text{C}$) and T is the instantaneous temperature. The dimensionless velocity was defined by Salat et al (2004) as follows;

$$\text{Dimensionless Velocity}(U_{CN}) = \frac{\alpha}{H} Ra^{1/2} \quad (5.2)$$

where α is the thermal diffusivity and H is the height.

The numerical and experimental temperature and velocity results at mid-height display similar trends. There are some differences in the velocity magnitude in the near wall region, and there is a dissimilarity in the near wall regions of the temperature profiles between the numerical and experimental data. It can be seen that all three turbulence models from the present study give similar results for temperature but the DES model gives superior results for vertical velocity. Further calculations were undertaken by Salat et al. (2004) using experimental horizontal wall temperatures as boundary conditions in

the numerical model. This gave numerical results that were in much better agreement with the experimental results than those obtained using adiabatic walls.

Figure 5-4 and Figure 5-5 gives the dimensionless temperature and velocity profiles at mid-width of the median plane in the cavity. The experimental results differ from the numerical results in magnitude but again show similar trends. The k-epsilon model showed slightly better results for thermal stratification and the DES model again proved to give better results for the velocity profile. Note that in the graph, the DNS model profile is the result given by Salat et al. (2004).

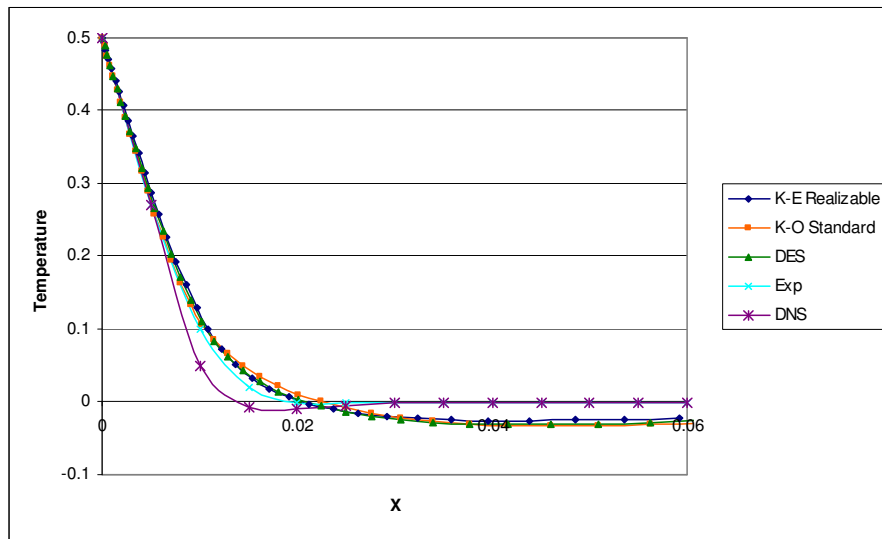


Figure 5-2 Dimensionless temperature profile at mid-height in the median plane in meters

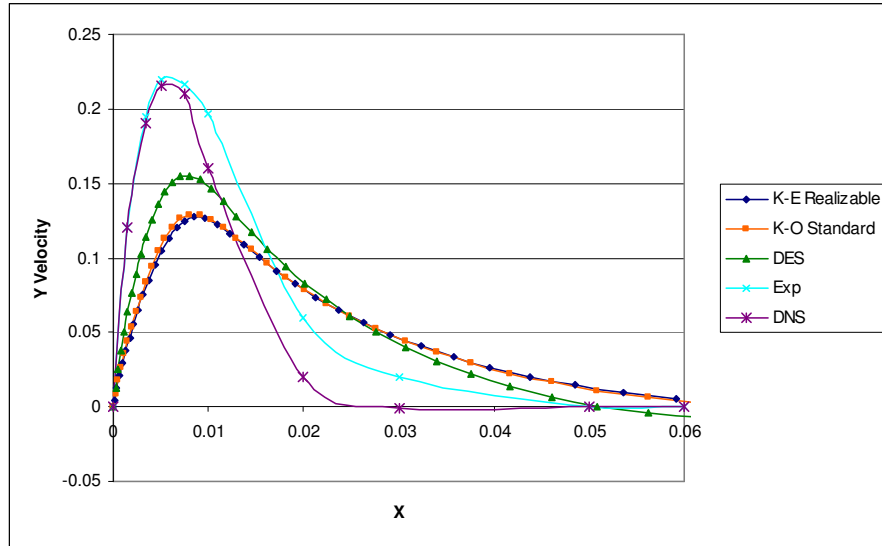


Figure 5-3 Dimensionless velocity profile at mid-height in the median plane in meters

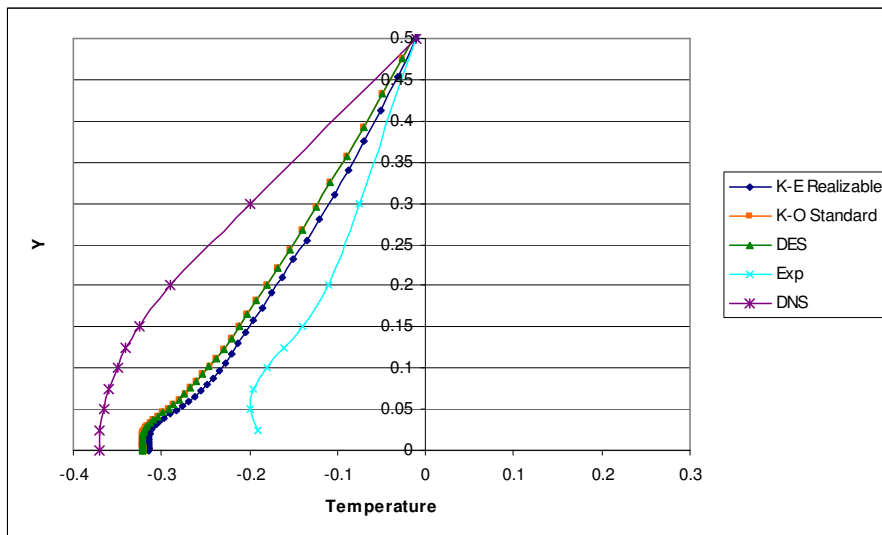


Figure 5-4 Dimensionless temperature profile at mid-width in the median plane in meters

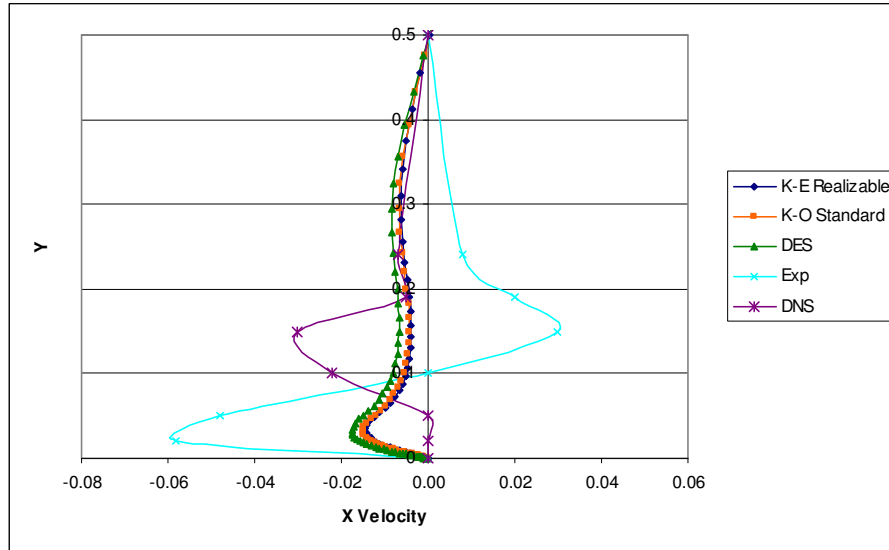


Figure 5-5 Dimensionless velocity profile at mid-width in the median plane in meters

The above graphs do not show the results obtained for other turbulence models considered (e.g., standard k-epsilon model, RNG k-epsilon model, SST k-omega model, and the LES model). The results obtained using all turbulence models are given in Appendix A – Further Numerical Results. The difference between the results given by all of the turbulent models is further discussed below.

K-epsilon Models

As discussed in the FLUENT documentation, the realizable and standard models are very similar with slightly different dissipation (ε) equations and slightly different ways of calculating the eddy viscosity (C_μ). The results obtained with these two models are very similar as can be seen from the results given in Appendix A – Further Numerical Results. The standard model is usually more accurate for domains with entirely turbulent flows however it will be seen that it predicts similar results to both k-epsilon models. The

realizable term has a modified dissipation formula which may allow more accurate flow predictions in some situations. However this was not the case here.

The RNG model gave results similar to those obtained using the standard k-epsilon model. The main difference between the RNG model and the standard model is in the calculation of the turbulent viscosity. The RNG calculates the effects of high strain rates more accurately and therefore it is typically better in some types of flows.

K-omega Models

The k-omega SST model varies slightly from the standard model in that it uses the standard k-omega model in the inner region of the boundary layer and then switches to a high-Re number version of the standard k-epsilon model in the outer region of the boundary layer using a blending function. The standard k-omega model incorporates a low-Re correlation coefficient that dampens the turbulent viscosity in low-Re flows. It has a built in wall function approach similar to the enhanced wall functions available in the k-epsilon model and when fine meshes are used in the near wall regions, the low-Re boundary conditions are applied. The SST model accounts for the transport of principal shear stress when calculating the turbulent viscosity and also has a cross-diffusion term introduced by separate equations used in regions near and far from the wall. It is believed for these reasons that the standard k-omega model and the k-omega SST model will give similar results in the near wall regions but in some cases will give different results in regions far from the walls. The results obtained using these two models are given in Appendix A – Further Numerical Results.

LES and DES Model

The results obtained using the LES model was not shown in the above figures. Generally the LES models gave results that were less accurate than those given by the DES model. As previously mentioned the LES model directly resolves the large eddies and models the small eddies and in a case such as this and requires a much finer mesh than RANS modeling. This caused significantly larger CPU costs. The same mesh was used and it is believed that this is the reason that less accurate results were achieved. Results for the LES and DES models are given in Appendix A – Further Numerical Results.

5.2.2 Heat Transfer at Walls

Average Nusselt number values along the line $y=0.5A_y$ for the hot wall are given in Table 5-1. Experimental results and results obtained numerically using several turbulence models are also given in this table.

Table 5-1 Comparison of average Nusselt number along the hot wall median line for several turbulence models

Turbulence Model	Surface Nu
Salat et al. Experimental	54.0
Salat et al. LES	61.0
Salat et al. DNS	60.1
K- ε Standard	51.2
K- ε Realizable	50.7
K- ε RNG	51.3
2nd Order K- ε Realizable	52.0
K- ω Standard	53.3
K- ω SST	50.6
DES	54.1
LES	61.6

It will again be seen that the numerical results are basically in good agreement with the experimental results. The LES average Nusselt number obtained in the present

study is very close to the LES results obtained by Salat et al. The DES model again proved to give the most accurate results as it almost exactly predicting the experimentally measured average Nusselt number of the hot wall. The standard K-omega model and RNG K-epsilon model also produced good results although all models except the DES model slightly underestimated the mean Nusselt number.

5.3 Concordia Atrium Results

Numerical results obtained using the physical assumptions listed in section 4.1.1 for the Concordia Atrium are discussed in this section. Calculations for various inlet vent velocities and various inlet flow angles for several external atmospheric conditions have been undertaken and will also be discussed.

5.3.1 Results with Different Turbulence Models

To further compare the results given by the various turbulence models, several models were used to find temperature and velocity fields in the Concordia atrium. The temperature and velocity profiles were obtained along vertical and horizontal lines that are shown as dotted lines in Figure 1-1. Figure 5-6 and Figure 5-7 show the horizontal temperature and velocity profiles at mid-height of the Concordia atrium perpendicular to the glass wall (a schematic of the Concordia Atrium is given in Figure 4-11). All four models display similar results for temperature and the LES and DES models give almost identical profiles. For the horizontal velocities all models show similar trends however the K-omega model predicts significantly different velocity magnitudes.

The vertical temperature and velocity profiles at the centre of the Concordia atrium are shown in Figure 5-8 and Figure 5-9. Once again, the K-omega model results

show similar trends but differ quite significantly in magnitude from the results given by other models. The temperature profiles are extremely close for all models except in the area $2m < Y < 4m$ where the K-omega model gave results that were significantly different from those given by the other models. The difference between the k-omega results and those given by the other models is possibly due to the incorporation of a low-Re modification in the model that gives this model the ability to predict wall bounded flows with good accuracy. Similar to the results obtained in the modeling undertaken by Salat et al (2004), the vertical velocities given by the DES and LES models appear to be greater in magnitude than those given by the K-epsilon model.

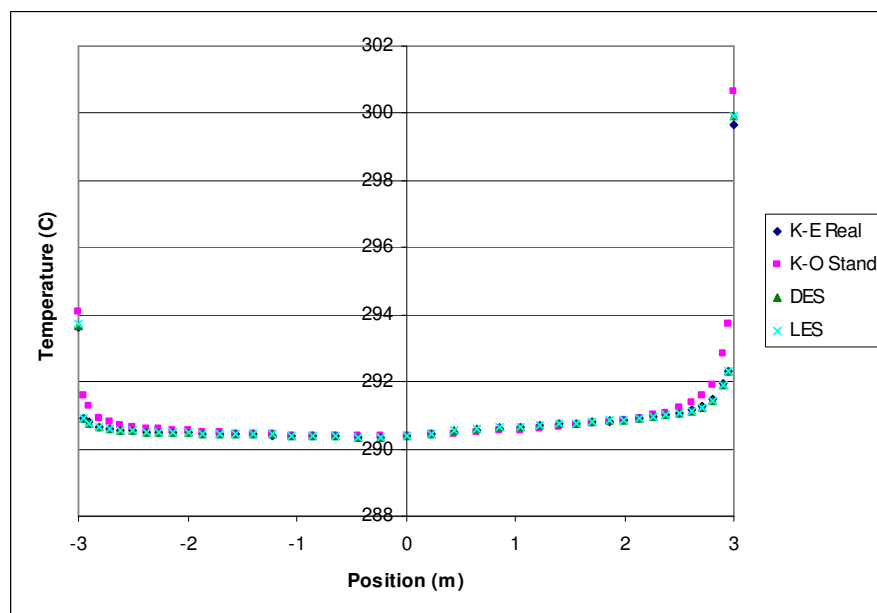


Figure 5-6 Horizontal temperature profile at mid-height of the Concordia Atrium using several turbulence models

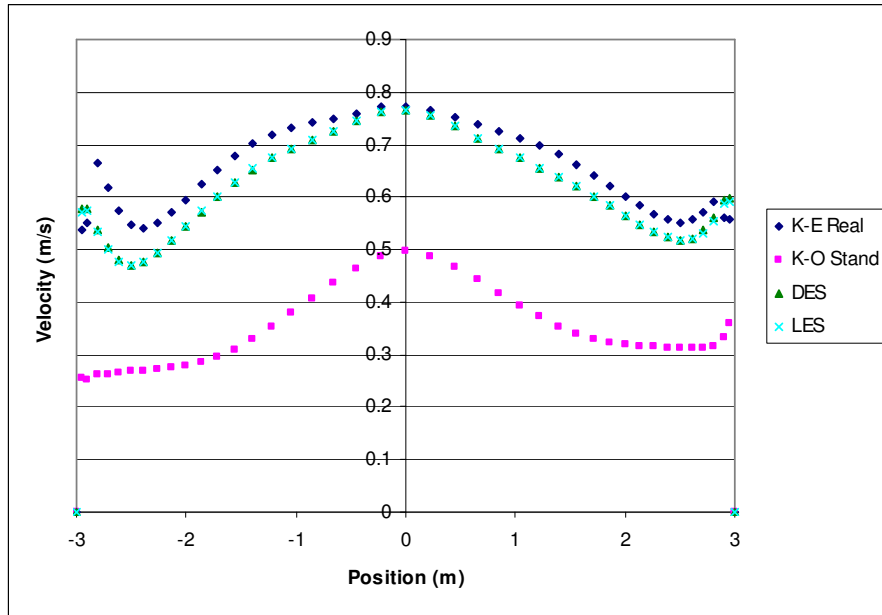


Figure 5-7 Horizontal velocity profile at mid-height of the Concordia Atrium using several turbulence models

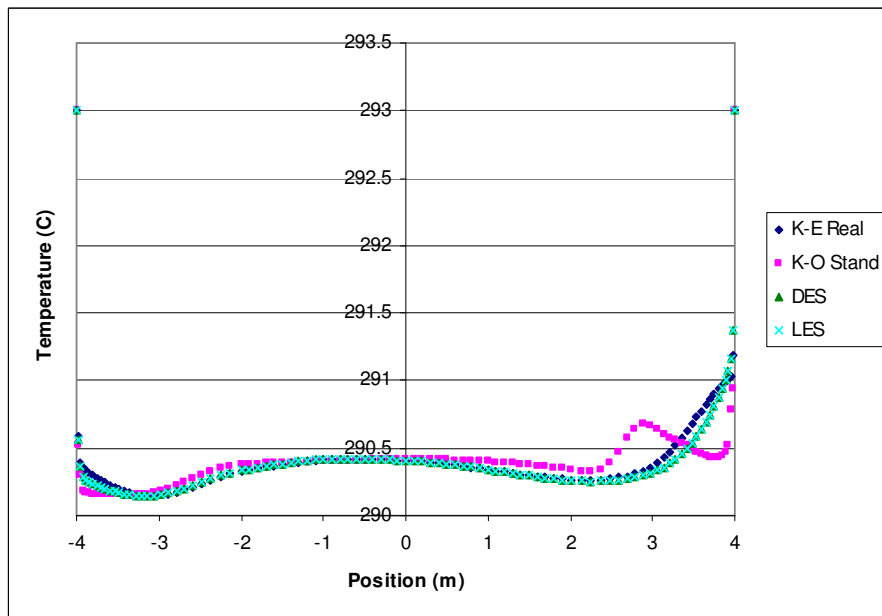


Figure 5-8 Vertical temperature profile at center of the Concordia Atrium using several turbulence models

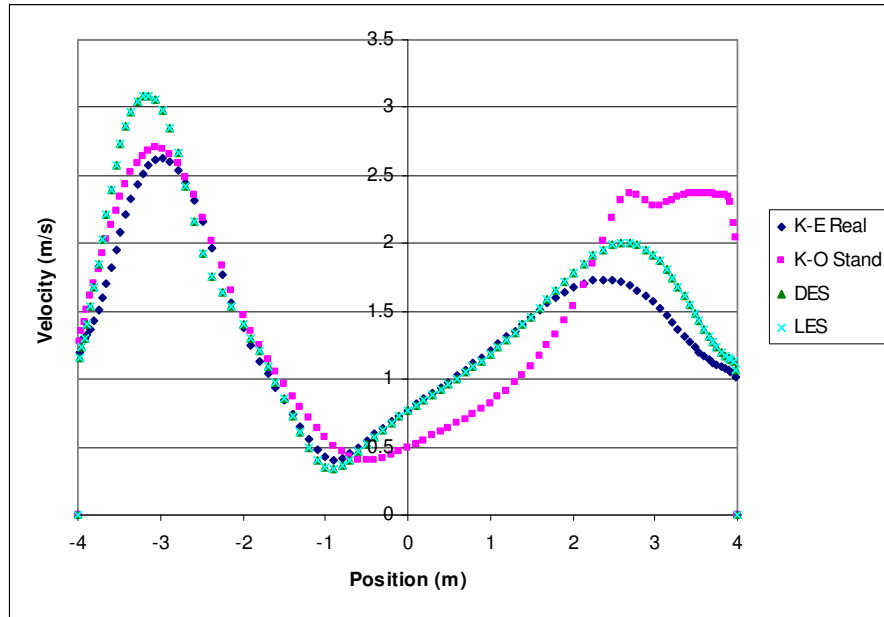


Figure 5-9 Vertical velocity profile at center of the Concordia Atrium using several turbulence models

5.3.2 Effect of Inlet Velocity

Calculations with vent inlet velocities of 1, 2, 3 and 4 m/s were used to determine the effect of the inlet velocity on the temperature and velocity fields. Figure 5-10 and Figure 5-11 show the horizontal profiles at mid-height of the Concordia atrium. It can be seen that the temperature profiles do not change much with changes in the inlet velocities. Figure 5-12 and Figure 5-13 show the vertical profiles and it can again be seen that the inlet velocity has little effect on the temperature except for the vertical temperature at an inlet velocity of 1m/s. In this case the vertical temperature through the middle of the atrium shows a temperature increase of approximately 0.5 Celsius.

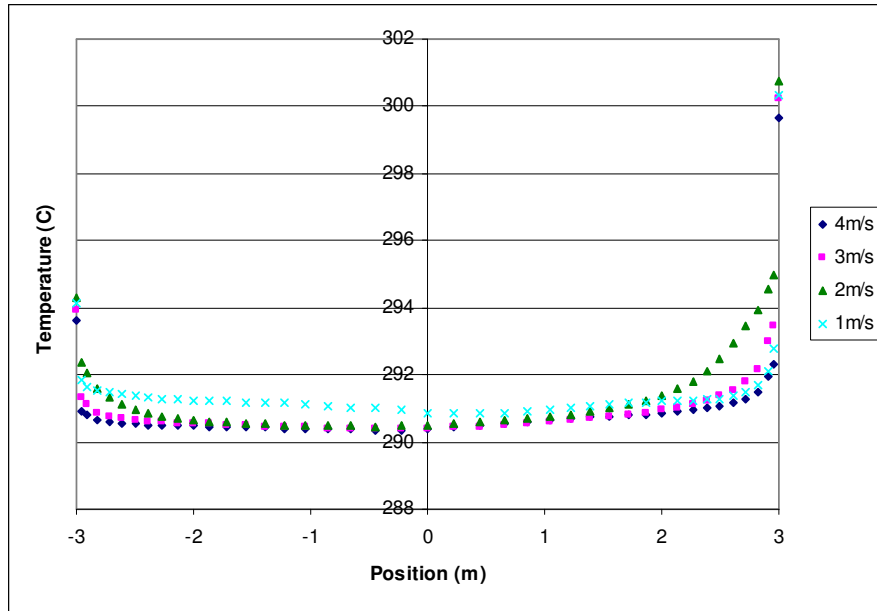


Figure 5-10 Horizontal temperature profile in the Concordia Atrium for several inlet velocities

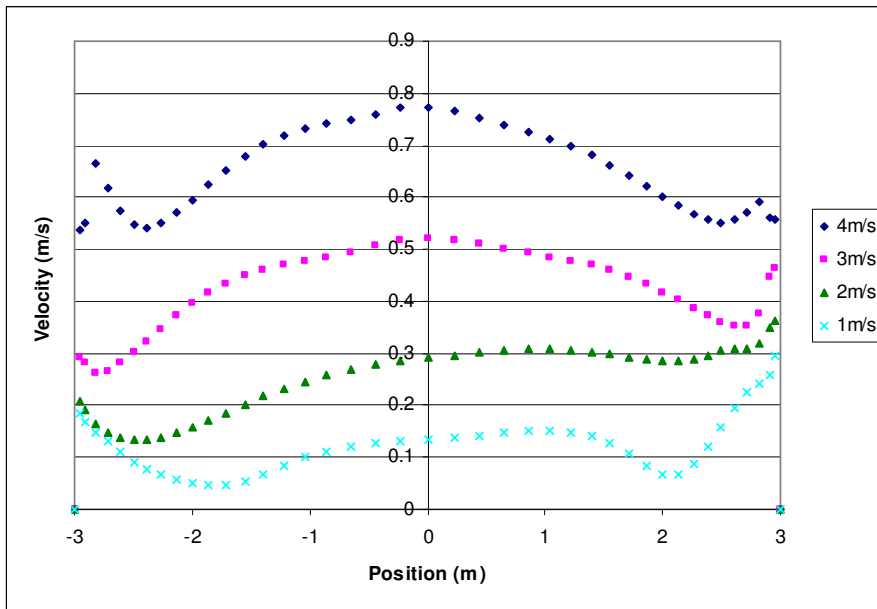


Figure 5-11 Horizontal velocity profile in the Concordia Atrium for several inlet velocities

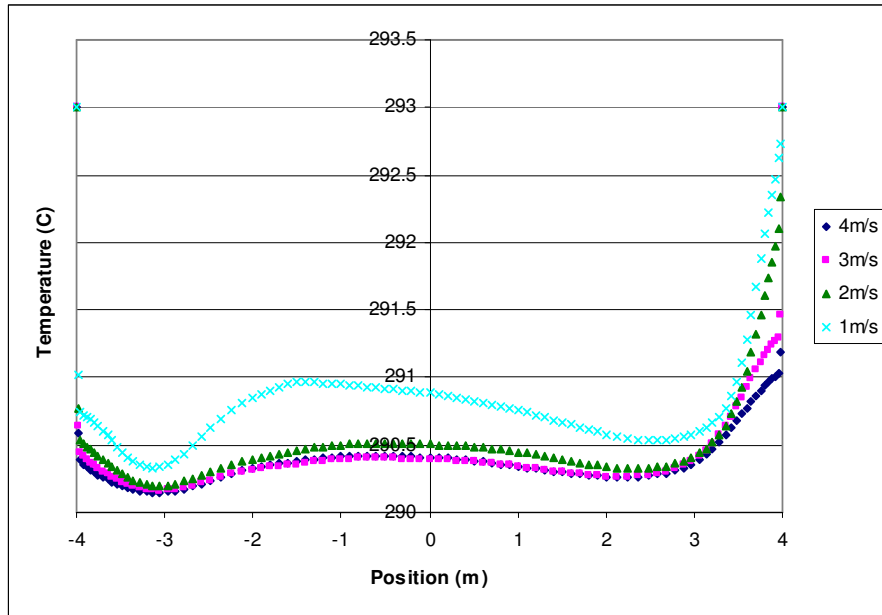


Figure 5-12 Vertical temperature profile in the Concordia Atrium for several inlet velocities

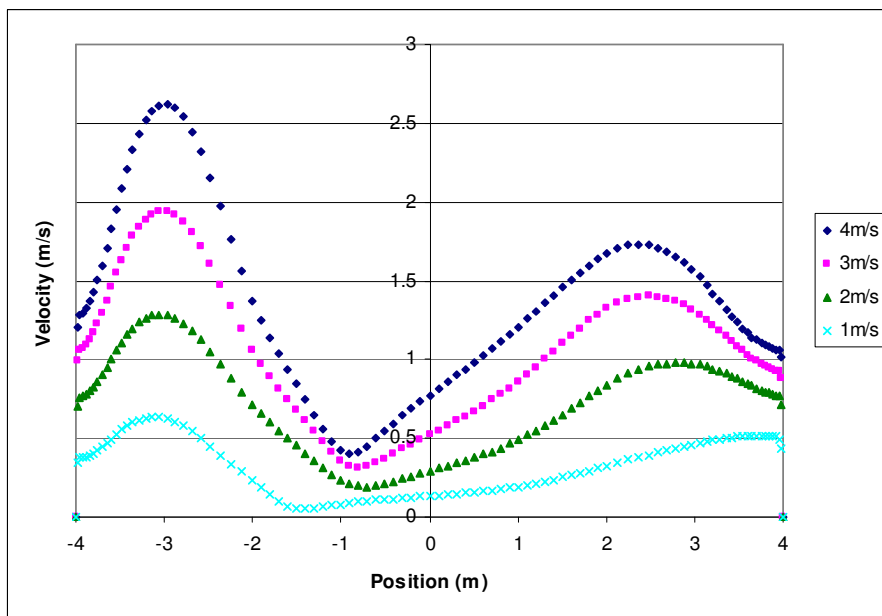


Figure 5-13 Vertical velocity profile in the Concordia Atrium for several inlet velocities

In a 3-dimensional flow case such as this, it is helpful to get a more descriptive look at the entire flow domain. Therefore temperature and velocity contours are given in Figure 5-14 and Figure 5-15. Two of the vertical planes cut through the middle of the atria and the third vertical plane shows the temperature contour of the glazing. The three horizontal planes are distributed evenly throughout the atrium.

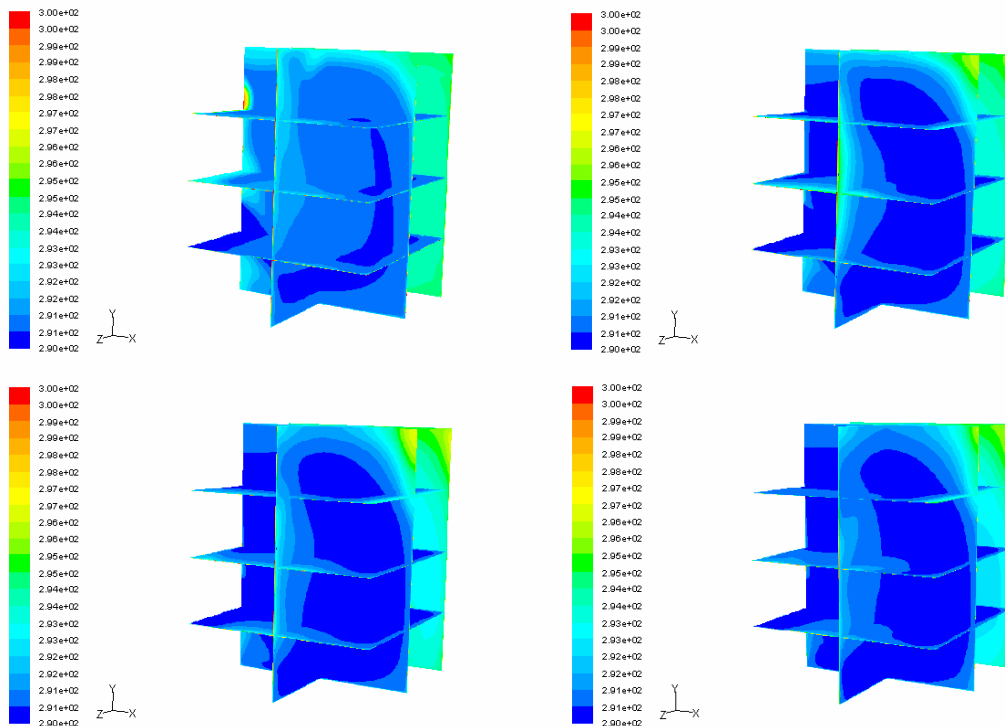


Figure 5-14 Temperature contours on multiple planes in the Concordia Atrium for inlet velocities of 1, 2, 3 and 4m/s respectively

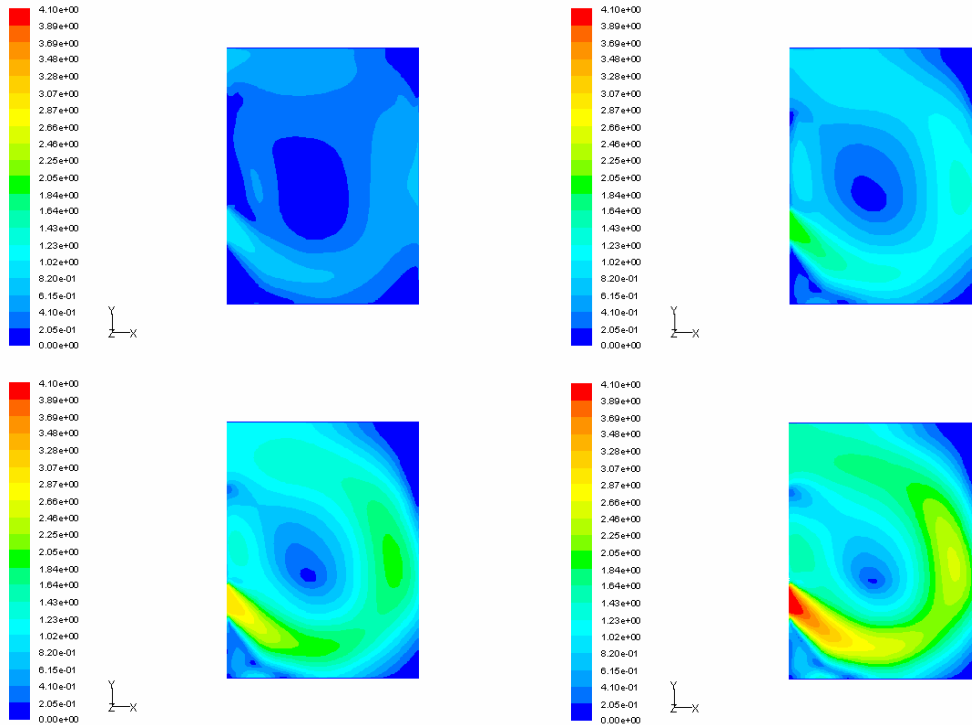


Figure 5-15 Velocity contours in the middle ($z=3\text{m}$) of the Concordia atrium parallel to the glazing for inlet velocities of 1, 2, 3 and 4m/s respectively

The contours given in Figure 5-14 show that the temperatures distributions are in all cases similar indicating that the inlet velocity does not have a large effect on the overall temperature distribution. All four velocities at the inlet are too high to show any significant difference in temperature stratification. The velocity contours given in Figure 5-15 shows that large velocities are predicted in areas of high pedestrian traffic and this may pose a comfort issue in the atrium. Both of these problems will be addressed later in this chapter.

5.3.3 Effect of Flow Inlet Angle

In order to gain a better understanding of what changes in the flow arise due to changes in flow inlet angle, a velocity of 2m/s was used and the flow was calculated for several inlet flow angles. Figure 5-16 and Figure 5-17 show the temperature and velocity contours for flow inlet angles of 26, 45, 63 and 90 degrees. This angle is defined as the angle between the vertical plane and the flow inlet direction. A flow inlet angle of 90 would be perpendicular to the vertical wall as seen in the following figures.

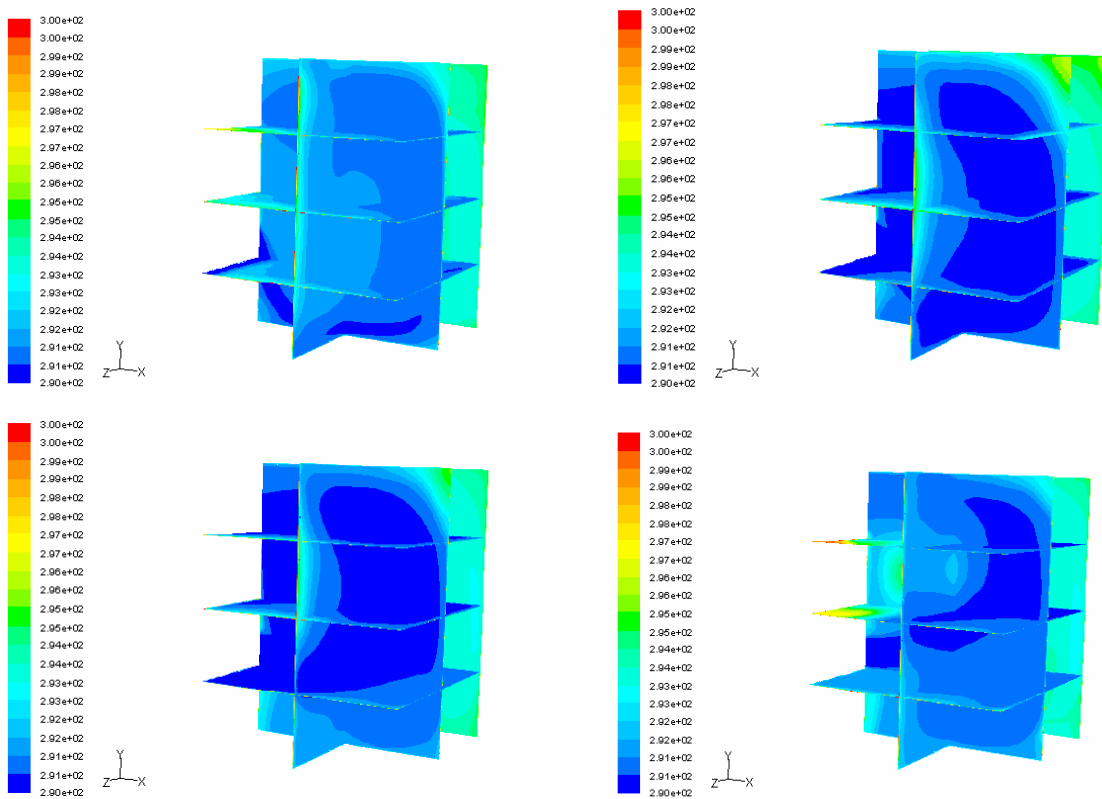


Figure 5-16 Temperature (K) contours on multiple planes in the Concordia atrium for inlet angles of 26, 45, 63 and 90 degrees respectively

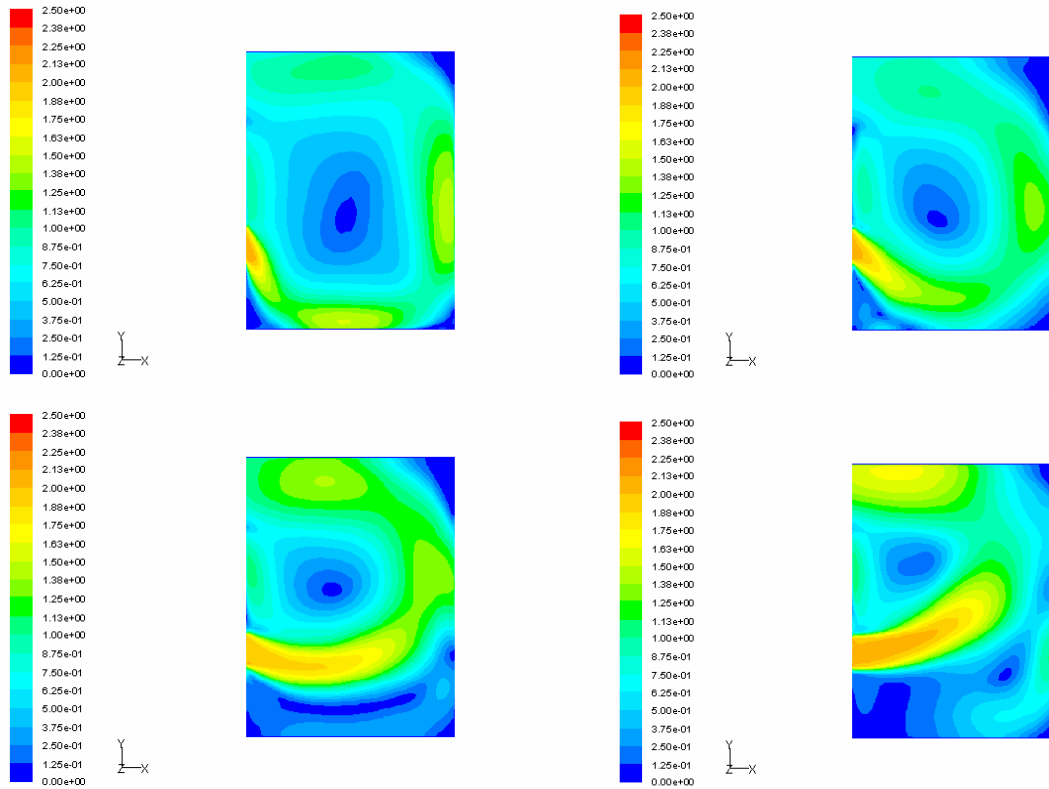


Figure 5-17 Velocity contours in the middle of the Concordia atrium parallel to the glazing for inlet angles of 26, 45, 63 and 90 degrees respectively

Figure 5-16 shows that the temperature contours in the room are relatively similar although for vent angles of 26 and 90 degrees the contours show areas with high temperature gradients that may be detrimental to comfort levels. The velocity contours show that for inlet angles of 63 and 90 there are lower velocities in the high traffic areas as the inlet vent is 2m from the floor but velocities are still too high for human comfort. At inlet angles of 26 and 45 degrees, velocities between 1 and 1.5m/s in the high traffic area are obtained which is likely to cause discomfort for patrons as the maximum recommended velocity for human comfort is 0.3m/s reported by Jones et al. (1992).

The results in this section and section 5.3.2 have shown that the inlet velocity and temperature tend to have the major effect on the temperature and velocity profiles in the atrium at any of the inlet velocities and inlet angles (as opposed to other effects such as buoyancy or radiation effects considered). Further work was undertaken to find inlet conditions that gave an acceptable indoor environment based on considerations of human comfort. A velocity of 0.5m/s and a temperature of 293K were used for the flow inlet boundary conditions and results for several turbulence models were obtained, these being given in Figure 5-18 to Figure 5-21.

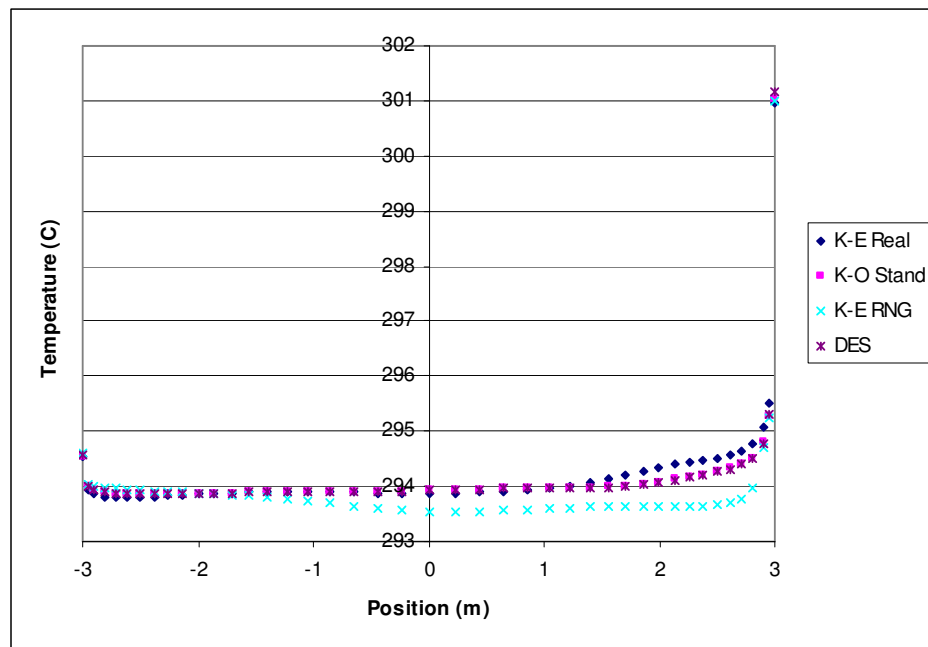


Figure 5-18 Horizontal temperature profile for inlet velocity of 0.5m/s and inlet temperature of 293K

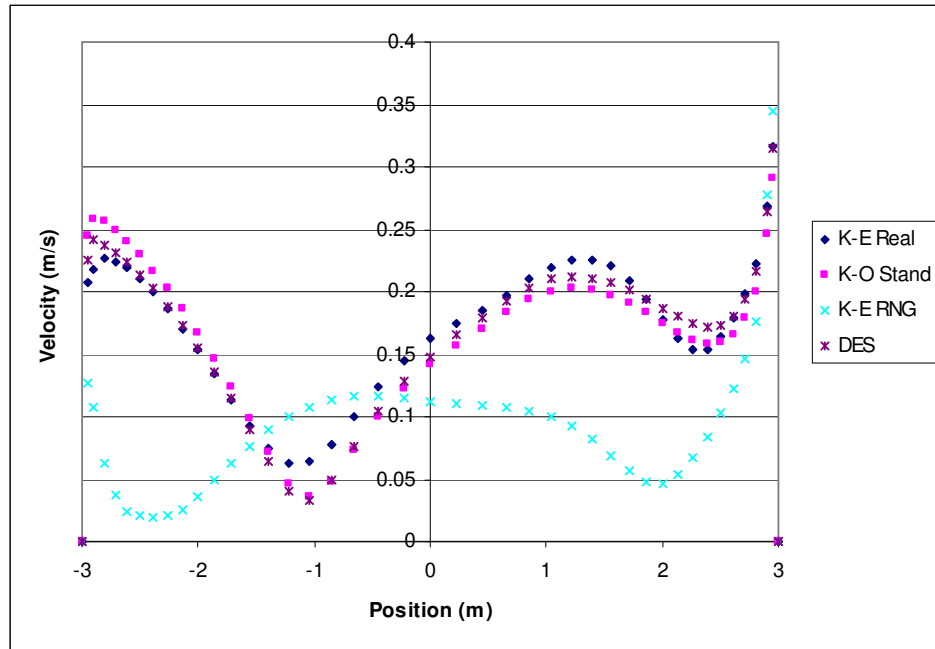


Figure 5-19 Horizontal velocity profile for inlet velocity of 0.5m/s and inlet temperature of 293K

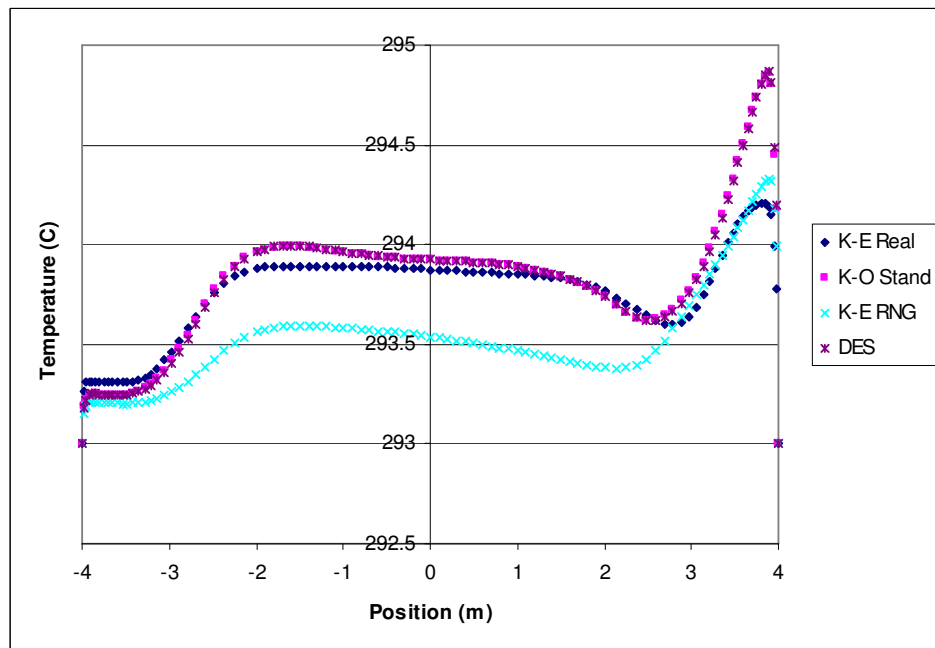


Figure 5-20 Vertical temperature profile for inlet velocity of 0.5m/s and inlet temperature of 293K

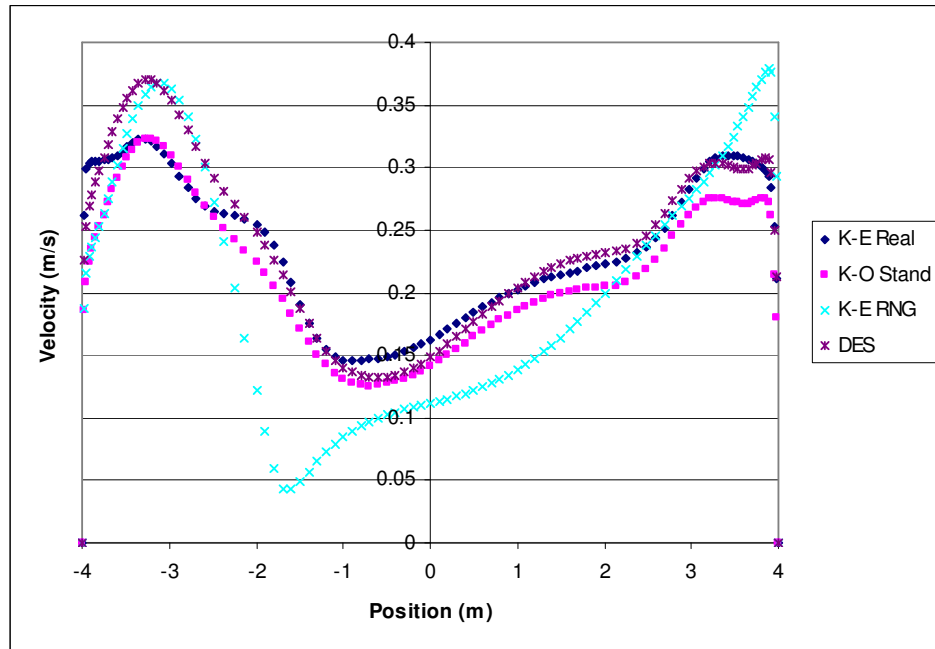


Figure 5-21 Vertical velocity profile for inlet velocity of 0.5m/s and inlet temperature of 293K

The temperature and velocity profiles in the horizontal and vertical directions show common trends for almost all the turbulent models considered. The k-epsilon model however gave results that were different in magnitude and sometimes in the profile form particularly in the velocity profiles. The different velocities for the inlet flow conditions have affected the velocities and temperatures significantly. This is demonstrated by comparing the contours in Figure 5-17 with the velocity contours given in Figure 5-22. The velocities are much lower in the region below 2m where pedestrians may be. Velocities were found to be around the 0.3m/s max for human comfort except in areas close to the inlet vent where velocities increase to 0.5 m/s. The profiles in Figure 5-19 and Figure 5-21 also show that velocities reach a value of up to 0.3m/s in the region about 2m from the floor. It should also be noted that the k-epsilon RNG model had

convergence problems and took much longer to converge which may be why the results given by this model differ from that given by the other models. Temperature contours for the atrium are shown in Figure 5-23 for the inlet flow of 0.5m/s. The temperatures are more consistent and more evenly distributed at around 294K as opposed to the temperatures in Figure 5-16 where the higher inlet velocity was used. The profiles given in Figure 5-23 shows that no large temperature gradients are present which may cause thermal comfort issues.

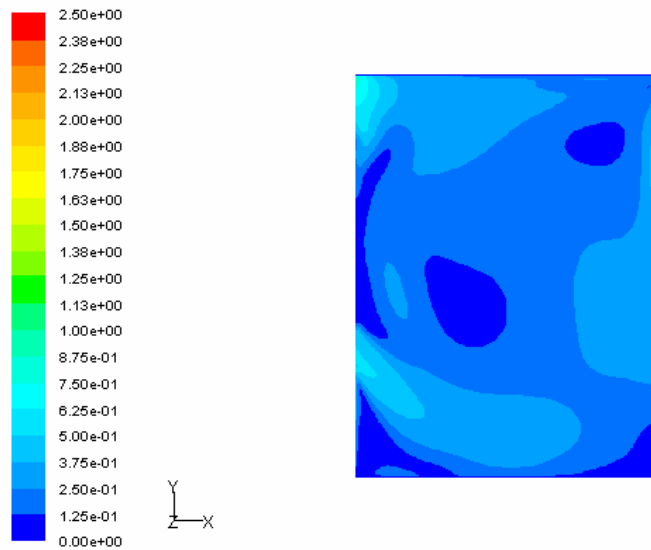


Figure 5-22 Velocity (m/s) contour at mid width in the x-y plane for inlet velocity of 0.5m/s and inlet temperature of 293K

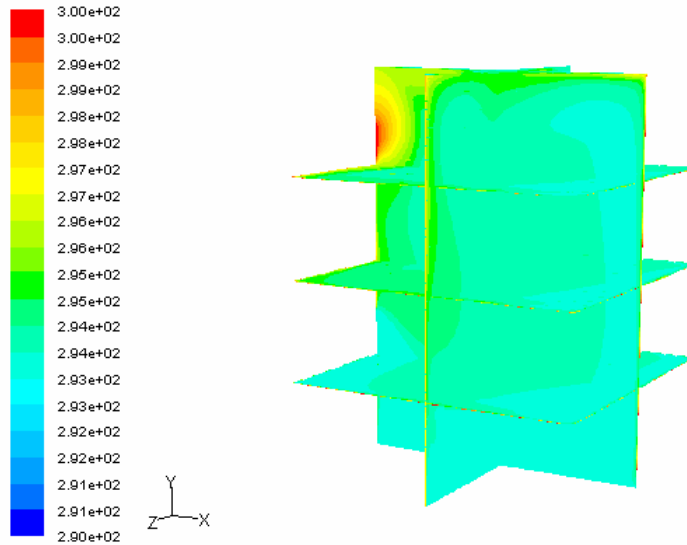


Figure 5-23 Temperature contour for inlet velocity of 0.5m/s and inlet temperature of 293K

5.3.4 Natural Convection

Three cases for different times of year for the atrium when there was no mechanically induced air flow in the atrium (i.e., all air motion was due to natural convection) were examined. The k-epsilon Realizable model was used for the natural convection study. Figure 5-24 and Figure 5-25 show the horizontal temperature and velocity profiles and it can be seen that the temperature is as would be expected; slightly lower temperatures in the colder months. The velocity profile shows that velocities do not change significantly depending on the time of year. The above statements are also true about the vertical temperature and velocity profiles in Figure 5-26 and Figure 5-27.

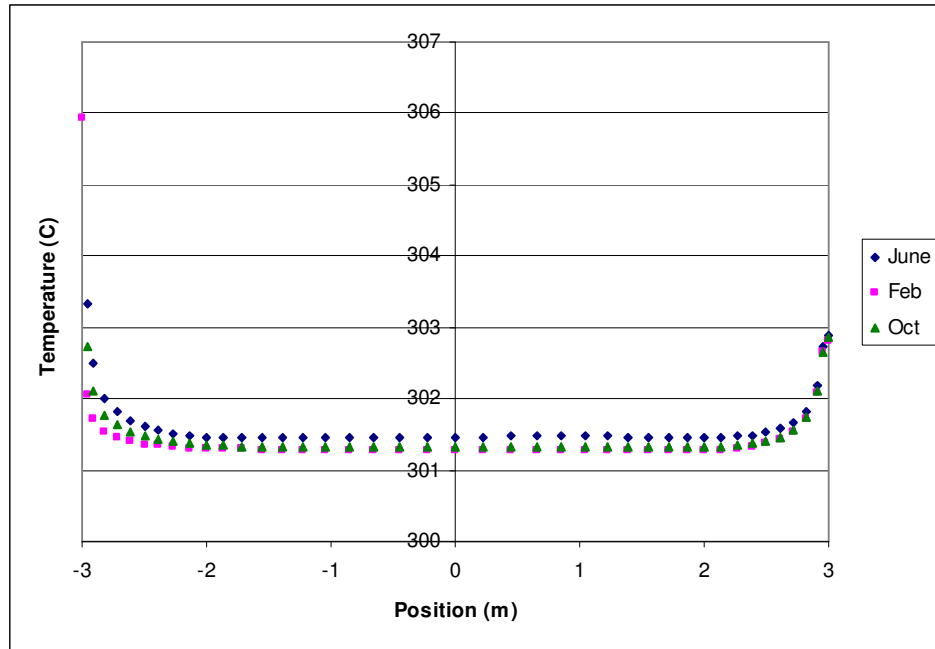


Figure 5-24 Horizontal temperature profile using the k-epsilon realizable model for different times of year

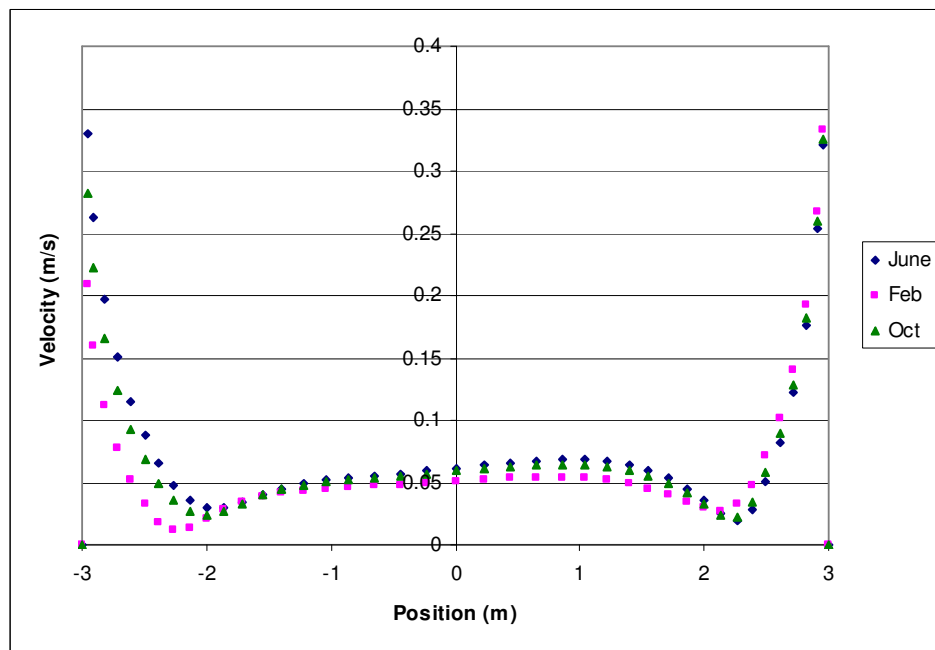


Figure 5-25 Horizontal velocity profile using the k-epsilon realizable model for different times of year

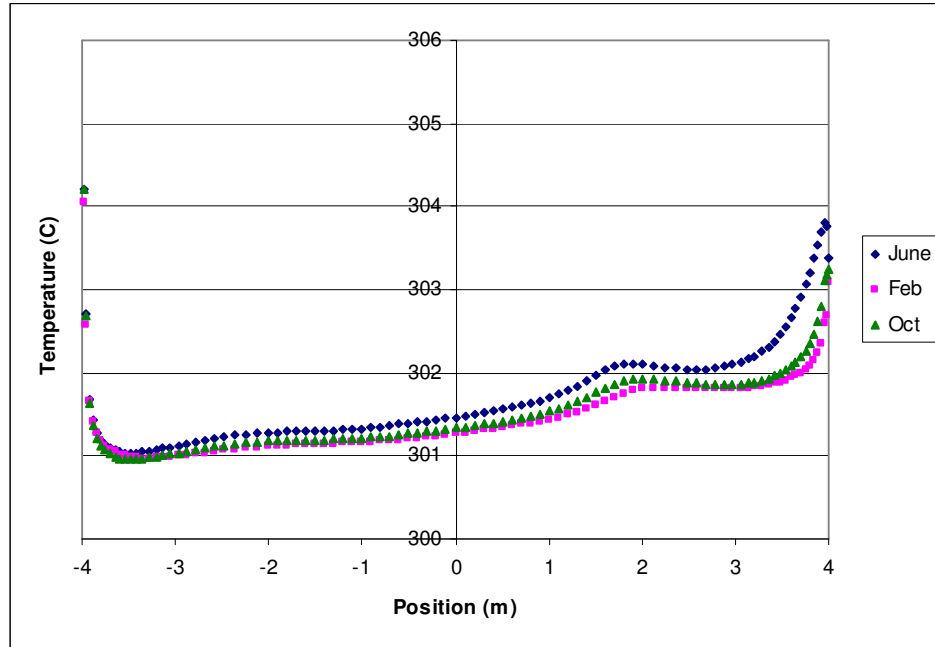


Figure 5-26 Vertical temperature profile using the k-epsilon realizable model for different times of year

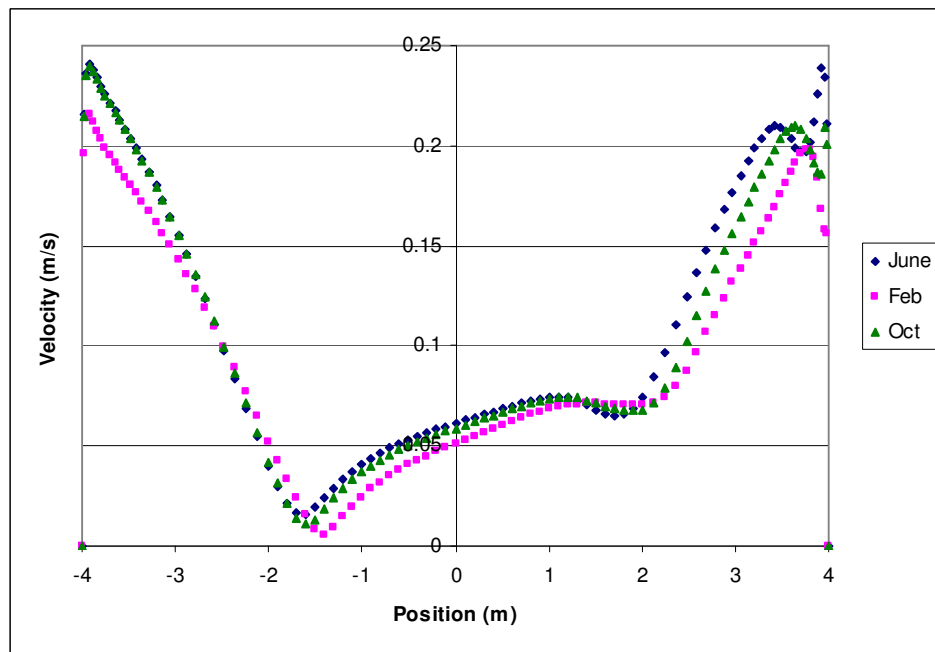


Figure 5-27 Vertical velocity profile using the k-epsilon realizable model for different times of year

Temperatures in the atrium are consistent with the climate for the specific time of year considered, and the velocity profiles are relatively similar for all months considered. It is important to note that in the colder months, the sun is lower and therefore more solar energy is entering through the glass wall into the atrium. This is most likely the reason for the relatively small differences in the temperature profiles for the atrium for February, June and October even though there are large differences in climatic conditions in these results.

Three turbulence models (k-epsilon RNG, Realizable and Standard) and two flow situations (forced flow and purely natural convection) were used to model the air flow in the Concordia-like atrium using external conditions for the month of February to investigate the differences in velocity and temperature. The velocity was found at a height of 1.2m (to consider human comfort levels) and a temperature difference was calculated from the bottom of the atrium (0.25m from the floor) to the top of the atrium (0.25m for the ceiling). The temperature difference and velocity at height $y = 1.2\text{m}$ is compared for the purely natural convection case and a case using a inlet velocity of 0.5m/s and a temperature of 293K described in section 5.3.3. Figure 5-28 shows atrium with the dashed lines representing the where the velocity and temperature profiles were calculated and plotted.

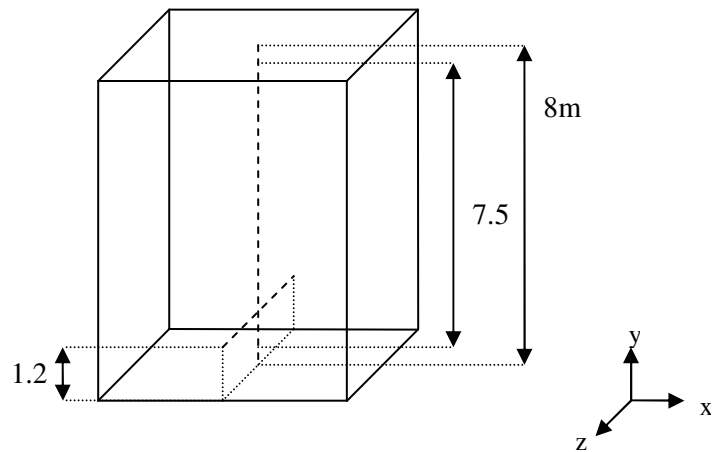


Figure 5-28 Geometry showing dashed lines where temperature and velocity profiles are calculated

The results are summarized in Table 5-2 and the plots for the natural convection case are given in Appendix A. The plots for the forced flow ($v=0.5\text{m/s}$ and $T=293\text{K}$) are given in Figure 5-18 to Figure 5-21. The velocities in the table at a height of 1.2m represent the velocity averaged along the horizontal dashed line in Figure 5-28 except for the regions that were 0.25m or less from each wall.

Table 5-2 Temperature and velocity at $H=1\text{m}$ for several turbulence models and flow situations

Model	Natural Convection		Forced Flow (inlet velocity=0.5m/s)	
	ΔT (K)	V (m/s)	ΔT (K)	V (m/s)
k- ε RNG	0.59	0.17	1.04	0.33
k- ε Realizable	0.41	0.15	0.89	0.27
k- ω Stand.	0.92	0.12	1.50	0.27
DES	0.93	0.16	1.49	0.31

Results for natural convection show smaller differences in temperature than the results for the forced flow case. Temperature differences obtained with the various turbulence models considered are relatively close but the k-omega and DES models predict higher temperature differences than both k-epsilon models for the natural convection case and for the forced flow case. Similar to the results comparing turbulence models in section 5.3, the standard k-omega model predicted lower velocities than the other models even though they all predicted similar results. Considering human comfort, all models predicted temperature changes and velocities that are well within acceptable comfort levels for the natural convection case. The forced flow case gave velocities that were slightly higher than recommended acceptable levels but temperature levels and gradients proved to be acceptable

5.4 Annex 26 Atrium Results

Numerical results obtained using assumptions listed in the previous chapter for the Annex 26 atrium in Yokohama Japan are discussed in this section. Results will be given along the dashed lines shown in Figure 5-29. Air temperatures were measured along the vertical dashed lines in Figure 5-29-A, and the wall temperatures were measured along the dashed lines in Figure 5-29-B.

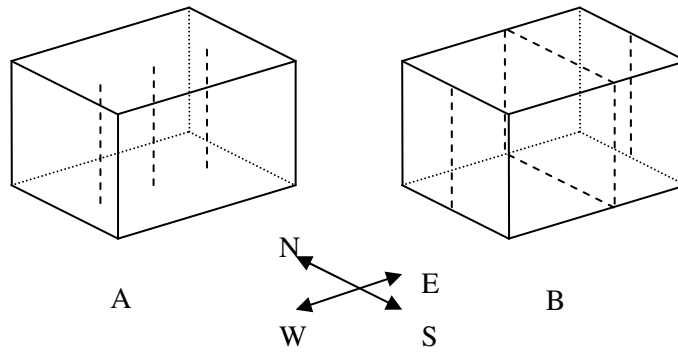


Figure 5-29 Vertical Profiles for different times of year

5.4.1 Comparing Results given by Various Turbulence Models

The results for average air temperature are given in Table 5-3. Several turbulence models were tested for this case including k-epsilon Realizable model, k-epsilon RNG model, k-omega Standard model, and the Detached Eddy Simulation (DES) model.

Table 5-3 Average Air Temperatures for several turbulence models

Model	Average Air Temperature (C)
Experimental	46
K- ϵ Realizable	38.0
K- ϵ RNG	39.3
K- ω Standard	38.9
DES	36.8

There are differences in the air temperatures predicted using the various turbulence models but all models predict similar values. It should be noted that no

information about the radiation properties are given in the paper by Heiselberg et al. (1998). This fact appears to have had an impact on the results because of the large amount of solar energy coming into the atrium through the four glass walls. As previously mentioned, the wall temperatures were calculated and averaged along the dashed line in Figure 5-29-B and are given in Table 5-4. Numerically calculated wall temperatures were found to be consistently lower than the experimental wall temperatures.

Table 5-4 Wall temperatures compared for several turbulence models

Wall	Experimental	K-ε Realizable	K-ε RNG	K-ω Standard	DES
West	36	32.5	32.7	32.7	30.5
East	32	27.8	28.3	28.3	26.2
North	48	48.0	48.0	48.0	48.0
South	42	35.6	35.8	35.6	33.5
Floor	48	48.0	48.0	48.0	48.0
Ceiling	44	43.5	43.4	43.2	42.6

5.5 Summary of Results

The results obtained for the air-filled cubic cavity were found to be comparable to experimental and numerical results obtained by Salat et al (2004). It was found that all of the turbulence models used in the study gave similar results and the results gave by the models varying only slightly from each other. The air temperature profiles were very close to experimental results showing the same basic trends. The velocity profiles also

showed similar trends, but the results given by the various models differed in magnitudes. The numerical results for heat transfer at the walls gave values very similar to the experimental results. None of the turbulence models gave clearly superior results to that given by the other models. The experimental results validated the numerical model used to a reasonable degree.

The effect of flow inlet velocities (1, 2, 3 and 4m/s) were investigated in a Concordia-like atrium giving good temperature distributions with no major fluctuations, but had velocity and temperatures within the space that would lead to human discomfort. All flow inlet angles considered also gave temperature distributions acceptable for human comfort throughout the atria but still gave velocities in high traffic areas that were much too high from 0.6m/s to 2.5m/s. A more reasonable set of boundary conditions (temperature = 293K, velocity = 0.5m/s) gave conditions in the atrium that met the criteria for acceptable levels of human comfort with velocities under 0.3m/s, good temperature distribution and average temperature around 294K.

The results for the purely natural convection case in the Concordia-like atrium for several times of the year suggested that the temperature in the atria is consistent with the climate for that time of year. The difference in temperatures for each time of year was relatively small compared to external temperature differences suggesting that solar heat entering the atria had a large effect on the temperature. More solar energy enters through the glass wall in the atria in colder months which possibly increased temperatures in the atria in colder months. When turbulence models were compared for the purely natural convective case and the forced flow case it was found that all models gave similar results but the k-epsilon models predicted slightly lower temperature differences than the k-

omega and DES models. Both the natural convective case and the forced flow case gave results that were reasonably acceptable for thermal comfort.

The results for the Annex 26 atrium in Yokohama Japan gave results for air temperature and wall temperature that were slightly lower than the experimental results but followed the same trend. The difference in experimental and numerical results can be attributed to the lack of information on material properties and radiation values of the surfaces. All models gave results that were relatively close to the experimental results for air and wall temperature. The difference in the numerical and experimental results is most likely because radiation values were not given and therefore had to be approximated for all surfaces in the atrium. This could make a significant difference considering how much solar radiation is entering through the four glass walls of the atrium.

Chapter 6 – Conclusions and Recommendations

6.1 Conclusions

Three separate scenarios have been used to study the difference in the results given by the selected turbulence models. Heat transfer quantities and temperature and velocity profiles have been examined in the comparison of the models to determine the relative accuracy of each of the models.

Computational and experimental results from a study by Salat et al. (2004) were compared with the numerical results produced in this study to validate the numerical solution procedure. The following conclusions were drawn from this comparison:

1. All turbulence models gave results for wall temperature that were similar and comparable to the experimental and numerical results of Salat et al. (2004). None of the models gave results that showed an increase in accuracy compared to the experimental results.
2. Temperature and velocity fields were compared and all turbulence models again gave comparable results however the DES model gave slightly more comparable results to the experimental data. The DES and LES models also require more computational expense as they can require a finer mesh to resolve the large eddies. The three K-Epsilon models gave similar results that were comparable to the experimental data.

3. The average surface Nusselt number was calculated and again all of the turbulence models gave results comparable to the results given by Salat et al. (2004). The DES model gave the most accurate results, the LES model gave the least accurate results and the RNS models all gave similar and comparable results.

The main case in which the turbulence models were examined was the Atria in the EV building at Concordia University. This building has 5 identical atria each being 3 stories high and a south wall that is all glazing. The following conclusions were made;

1. Horizontal and vertical temperature profiles were used to compare the turbulence models. All models gave similar results although the k-omega model gave significantly different results for both temperature and velocity especially in the near wall regions.
2. The numerical results indicate that the inlet velocity has a dramatic effect on the comfort level of the occupants in the space using the k-epsilon realizable turbulence model.
3. The flow inlet angle also has a direct affect on temperature and velocity distributions in the flow domain. All flow inlet angles considered gave acceptable temperature distributions for human comfort but still gave velocities in high traffic areas that were higher than recommended.
4. The direction and velocity of a flow inlet has a dramatic effect on the velocity and temperature distributions in a space. A flow inlet with a velocity of 0.5 m/s and a temperature of 293K were found to be a good test case for determining variations in flow with different turbulence models. Similar results for velocity and

temperature profiles for multiple turbulence models using these conditions were obtained except for k-epsilon RNG model. The RNG model again gave results that were quite different from all of the other turbulence models.

5. Numerical results indicate that the temperature in the atria is consistent with the climate for that time of year. The solar heat gain has a large effect on the atria temperature and keeps the temperature change in the atria between seasons minimal compared to the external climate changes. Further study in the effects of the solar loading effect on atria are required.
6. The numerical results indicate that, in general, the turbulence model used to simulate naturally convective airflow in the atria has an effect on the temperature and velocities. The various k-epsilon models gave similar results but were not comparable to the k-omega and DES models which gave similar results.

A final scenario was investigated to compare the turbulence models presented in this study. The numerical results for Annex 26 atrium for the various turbulence models used gave air and wall temperatures that were similar but consistently lower than the experimental values. The radiation values for this case were not given and the difference between the experimental and numerical results shows the importance of using accurate radiation properties.

Overall it was found that all turbulence models used gave similar results that were in reasonably good agreement with the available results. When there were differences between the numerical and the experimental results it appears that this was due more to

the assumptions made in defining the physical boundaries rather than with deficiencies in the turbulence models.

6.2 Recommendations

- In the present study, the openings to the hallway in the Concordia-like atrium model were neglected to simplify the study. In order to more accurately model the atrium, it is recommended that the openings should be incorporated. Also the velocity inlet and pressure outlet are oriented differently in the Concordia atrium and the effects of HVAC orientation should be considered.
- 1st order upwind discretization scheme was used in the present study, however more accurate results could be obtained using 2nd order if computational expense is not considered. This could also be beneficial if a less fine mesh is used and a grid created that is aligned with the flow in areas such as the velocity inlet. Therefore an investigation of non structured grids is recommended for further studies in this area in order to use higher order discretization schemes.
- It was noticed in this study that radiation values have a large impact on the flow patterns in atria since large windows allow a large amount of solar energy into the space. It is suggested that further investigation of the effect of surface material and radiation properties on air flow in atria is undertaken. It is also suggested that further investigation of radiation models be investigated for air flow in atria.
- As thermal comfort as a result of direct solar radiation was not taken into consideration in this study, it is suggested that it be considered in future work as human comfort plays a large role in atria design.

- There is a need for more accurate and detailed experimental data for a specific atrium. Detailed boundary conditions such as thermal building envelope, mechanical ventilation effects, and conditions in the space are needed to compare the numerical results to the actual data.
- Further study of the accuracy of using a y -plus value of 10 should be undertaken. It is recommended that the effect of using lower values should be considered. Also, a first order discretization scheme was used for all models. The adequacy of using a first order scheme should be further verified for the LES and DES turbulence models

References

1. **ASHRAE *Fundamentals Handbook*, 2001**, SI Edition, American Society of Heating, Refrigeration and Air-Conditioning Engineers, Atlanta, USA.
2. **ASHRAE *Fundamentals Handbook*, 2005**, SI Edition, American Society of Heating, Refrigeration and Air-Conditioning Engineers, Atlanta, USA.
3. **Barth, T. J., Jespersen, D., 1989**, “The design and application of upwind schemes on unstructured meshes”, *Technical Report AIAA-89-0366*, AIAA 27th Aerospace Sciences Meeting, Reno, Nevada.
4. **Berglund, L. G., Fobelets, 1987, A.**, “A subjective human response to low level air currents in asymmetric radiation”, *ASHRAE Transactions*, Vol. 93 (1), pp 497-523.
5. **Choudhury, D., 1993**, “Introduction to the Renormalization Group Method and Turbulence Modeling.” *Fluent Inc. Technical Memorandum*, TM-107.
6. **Clarke, D. S., Wilkes, N. S., 1988**, “The calculation of turbulent flows in complex geometries using the algebraic stress model”, *AERE R 13251*, UKAEA Harwell.
7. **Gambit 2.3.16**, Fluent Inc., 1998-2007
8. **GE Structured Products, 1998**, “Lexan[®] 9034 Sheet - Product Data Sheet” General Electric Company, www.structuredproducts.ge.com
9. **Fanger, P.O., Christensen, N.K., 1986**, “Perception of draught in ventilated spaces” *Ergonomics*, Vol. 29(2), pp 215-235.
10. **Fanger, P.O., Melikov, A.K., Hanzawa, H., Ring, J., 1989**, “Turbulence and draft” *ASHRAE Journal*, Vol. 31(4), pp18-25.
11. **Fluent Users Guide, 2006**, Fluent 6.3 Documentation.
12. **Gosman, A. D., Pun, W. K., Runchal, A. K., Spalding, D. B., Wolfshtein, 1969, M.**, “Heat and mass transfer in recirculating flows” Academic Press, London.

13. **Heiselberg, P., Murakami, S., Roulet, 1998, C.-A.,** *Ventilation of large spaces in buildings*, Final Report IEA Annex 26, IEA Energy Conservation in Buildings and Community Systems, Aalborg, Denmark.
14. **Jaballah, S., Sammouda, H., 2007,** “Effect of surface radiation on the natural-convection stability in a two-dimensional enclosure with diffusely emitting boundary wall”, *Numerical Heat Transfer, Part A*, Vol. 51, pp 495-516.
15. **Jiang, Y., Chen, Q., 2002,** “Effect of Fluctuating Wind Direction on Cross Natural Ventilation in Buildings from Large Eddy Simulation”, *Building and Environment*, Vol. 37, pp 379-386.
16. **Jones P. J., Whittle, G. E., 1992,** “Computational Fluid Dynamics for Building Air Flow Prediction – Current Status and Capabilities”, *Building and Environment*, Vol. 27, No. 3, pp 321-338.
17. **Kim, S.-E., 2004,** “Large eddy simulation using unstructured meshes and dynamic subgrid-scale turbulence models”, *Technical Report AIAA-2004-2548, American Institute of Aeronautics and Astronautics, 34th Fluid Dynamics Conference and Exhibit*.
18. **Lau, J., Niu, J. L., 2003,** “Measurement and CFD Simulation of the Temperature Stratification in an Atrium Using Floor Level Supply Method”, *Indoor Built Environment*, Vol. 12, pp 265-280.
19. **Launder, B. E., Spalding, D. B.,** *Lectures in Mathematical Models of Turbulence*, Academic Press, **1972**.
20. **Lilly, D. K., 1992,** “A Proposed Modification of the Germano Subgrid-Scale Closure Model”, *Physics of Fluids*, Vol. 4, pp 633-635.
21. **Matweb,** <http://www.matweb.com> the Online Materials Information Resource, **2002**.
22. **Menter, F.R., 1994,** “Two-Equation Eddy-Viscosity Turbulence Models for Engineering Applications,” *AIAA Journal*, 32(8):1598-1605.
23. **Nielsen, P. V., 1974,** “Flow in air conditioned rooms”, PHD Thesis, Technical University of Denmark, Copenhagen.

24. **Nielsen, P. V., 2000**, “Velocity distribution in a room ventilated by displacement ventilation and wall mounted air terminal devices” *Energy and Buildings*, Vol. 31, pp 179-187.
25. **Olesen, B.W., Scholer, M., Fanger, P.O., 1979**, “Vertical air temperature differences and comfort” *Indoor climate*, Fanger, P.O., Valbjorn, O., eds. Danish Building Research Institute, Copenhagen.
26. **Salat, J., Xin, S., Joubert, P., Sergent, A., Penot, F., Le Quere, P., 2004**, “Experimental and numerical investigation of turbulent natural convection in a large air-filled cavity”, *International Journal of Heat and Fluid Flow*, Vol. 25, pp 824-832.
27. **Shih, T.-H., Liou, W.W., Shabbir, A., Yang, Z., and Zhu, J., 1995**, “A New $k-\epsilon$ Eddy-Viscosity Model for High Reynolds Number Turbulent Flows - Model Development and Validation.”, *Computers Fluids*, 24(3):227-238.
28. **Shur, M., Spalart, P. R., Strelets, M. and Travin, A., 1999**, “Detached-Eddy Simulation of an Airfoil at High Angle of Attack,” *4th Int. Symposium on Eng. Turb. Modeling and Experiments*, Corsica, France.
29. **Smagorinsky, J., 1963**, “General Circulation Experiments with the Primitive Equations. I. The Basic Experiment”, *Month. Wea. Rev.*, Vol. 91, pp 99-164.
30. **Sodja, J., Podgornik, R., 2007**, “Turbulence Models in CFD”, University of Ljubljana.
31. **Spalart, P., Allmaras, S., 1992**, “A one-equation turbulence model for aerodynamic flows”, *Technical Report AIAA-92-0439*, American Institute of Aeronautics and Astronautics.
32. **Walsh, P. C., Leong, W. H., 2004**, “Effectiveness of Several Turbulence Models in Natural Convection”, *International Journal of Numerical Methods for Heat and Fluid Flow*, Vol. 14, No. 5, pp 633-648.
33. **Wilcox, D. C., 1998**, “Turbulence Modeling for CFD,” DCW Industries, Inc., La Canada, California.

- 34. Yakhot, V., Orszag, S. A.,** “Renormalization Group Analysis of Turbulence: Basic Theory”, *Journal of Scientific Computing*, 1(1):1-51, **1986.**

Appendix A – Further Numerical Results

The numerical results presented in this section are in addition to the results presented in Chapter 5 –.

Cubic Cavity Results

The following graphs show the comparison of the variations in the *k-epsilon* model.

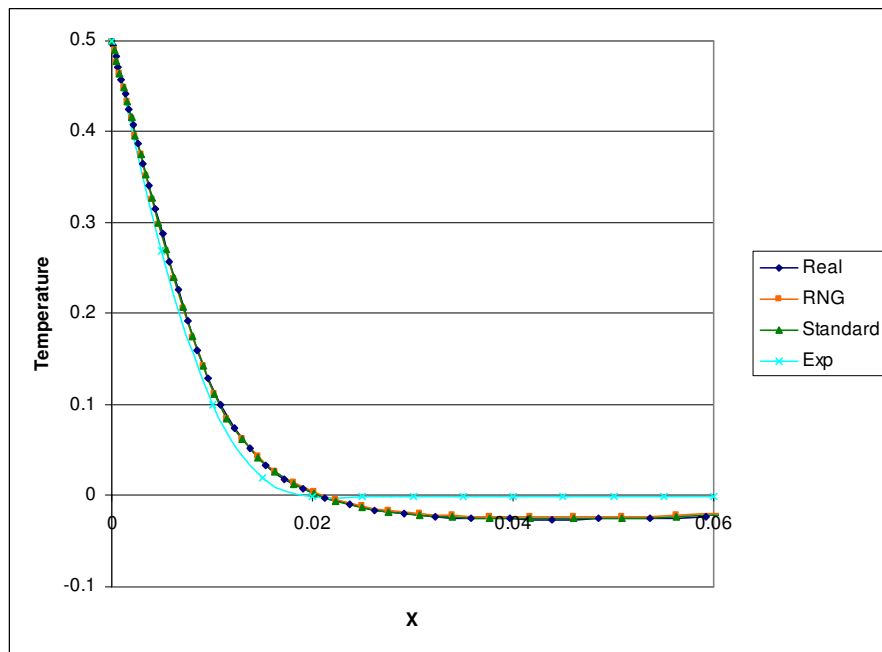


Figure 0-1 Temperature profile at mid-height in the median plane

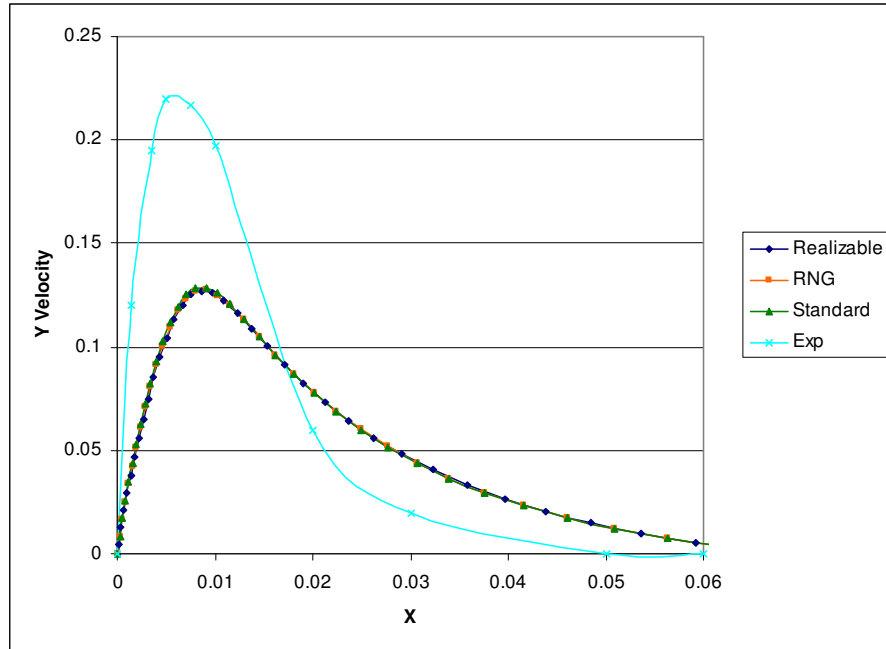


Figure 0-2 Temperature profile at mid-height in the median plane

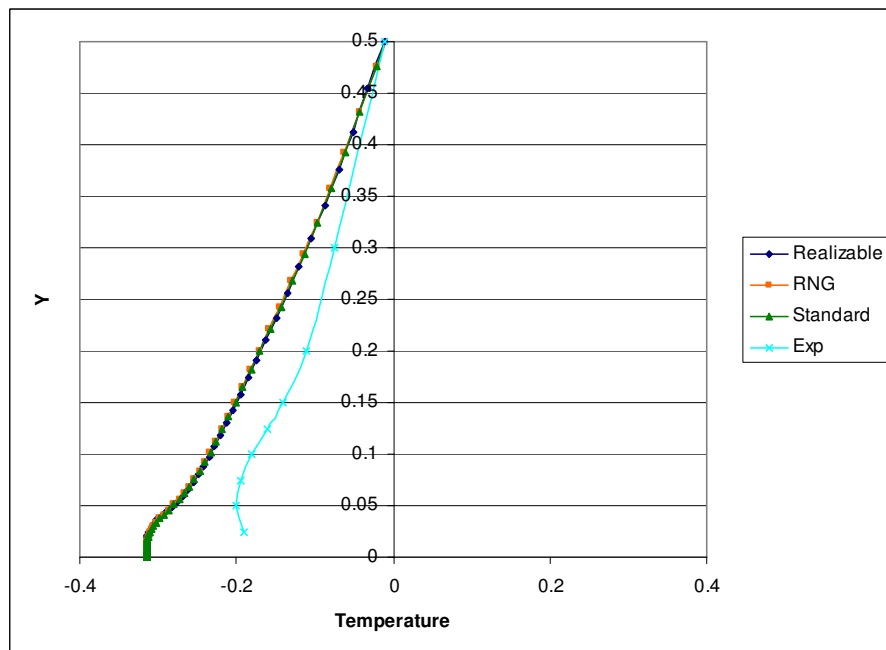


Figure 0-3 Velocity profile at mid-width in the median plane

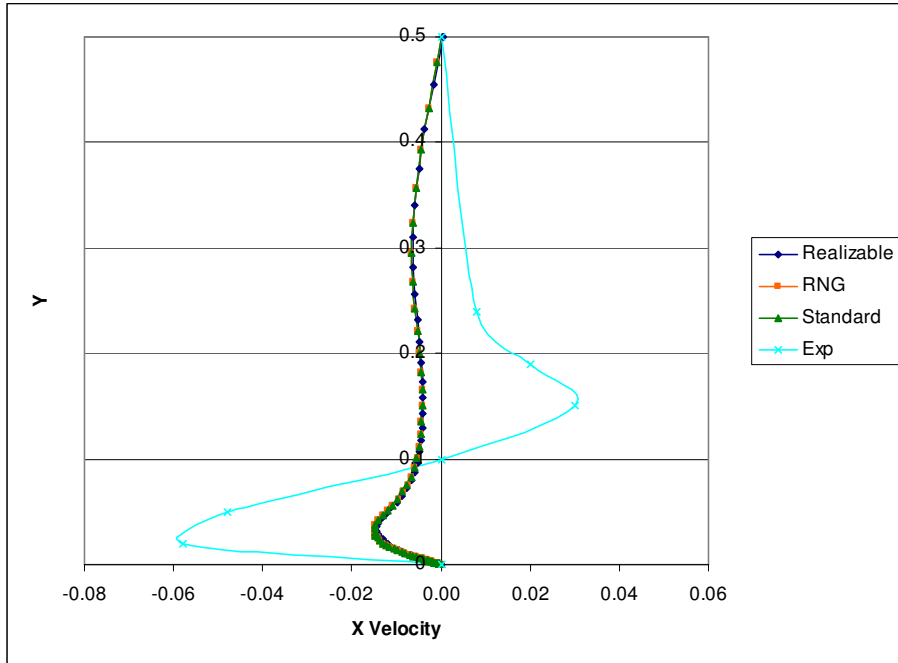


Figure 0-4 Temperature profile at mid-width in the median plane

The following graphs show the comparison of the variations in the *k-omega* model.

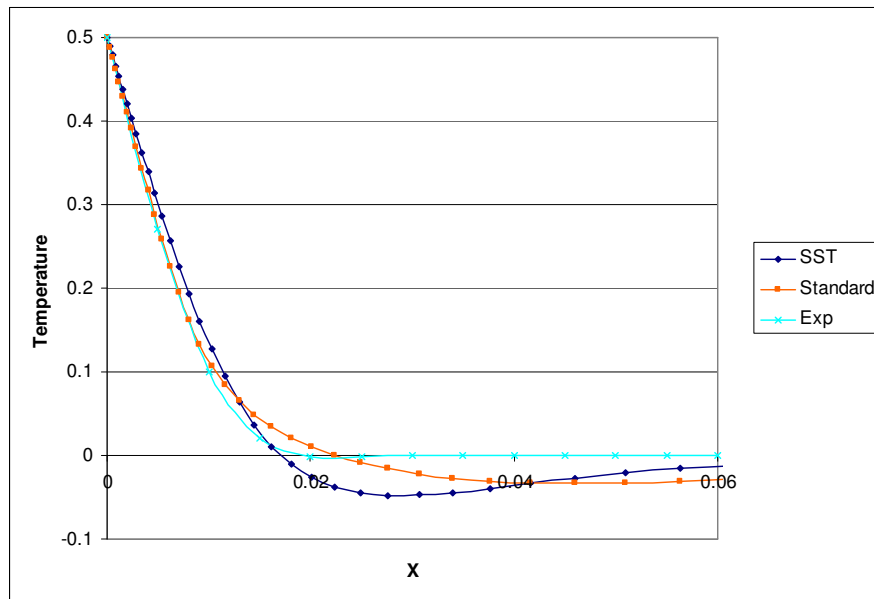


Figure 0-5 Temperature profile at mid-height in the median plane

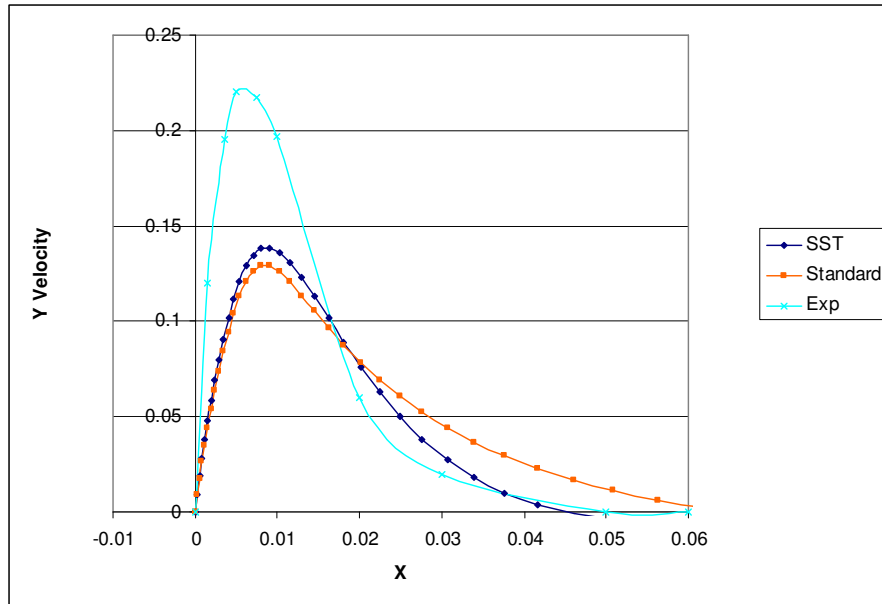


Figure 0-6 Velocity profile at mid-height in the median plane

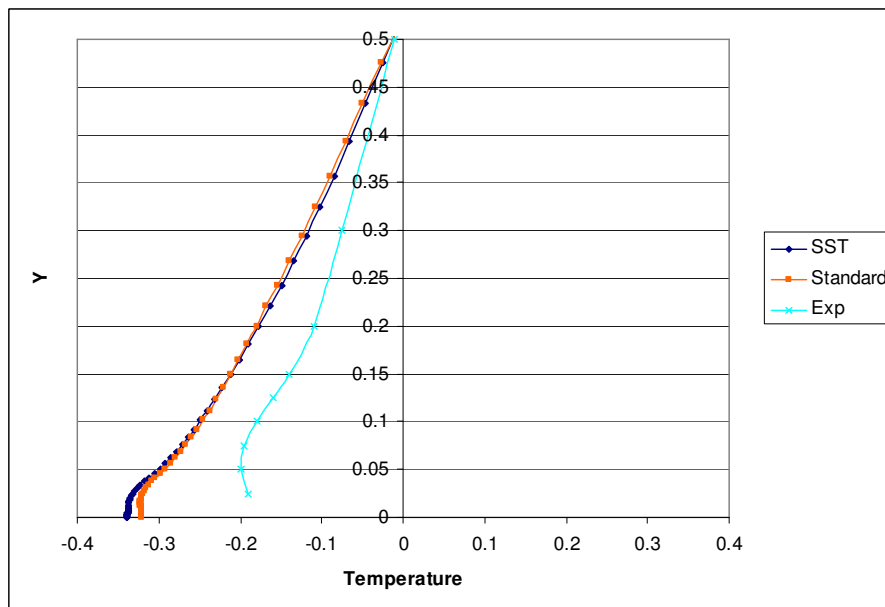


Figure 0-7 Temperature profile at mid-width in the median plane

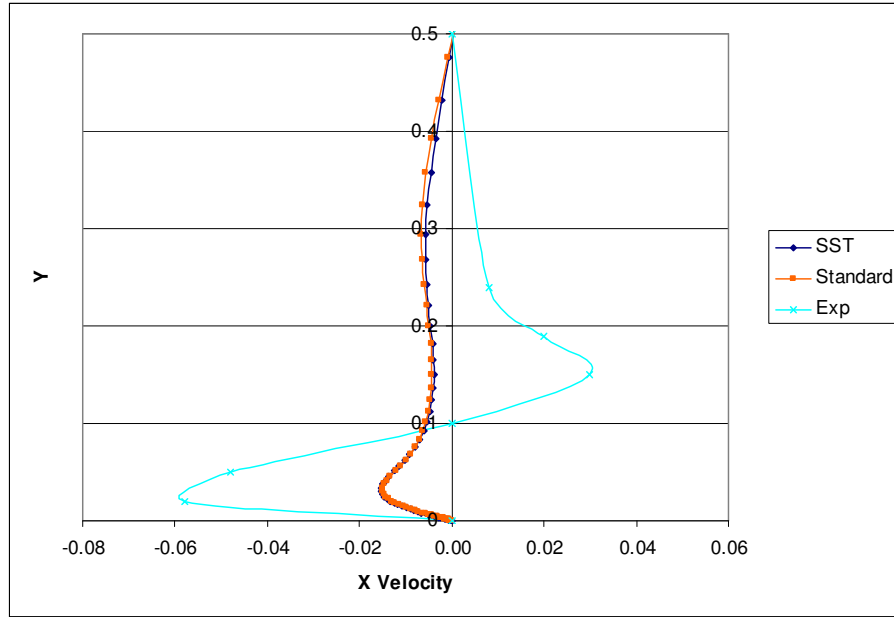


Figure 0-8 Velocity profile at mid-width in the median plane

The following graphs show the comparison of the *LES* and *DES* models.

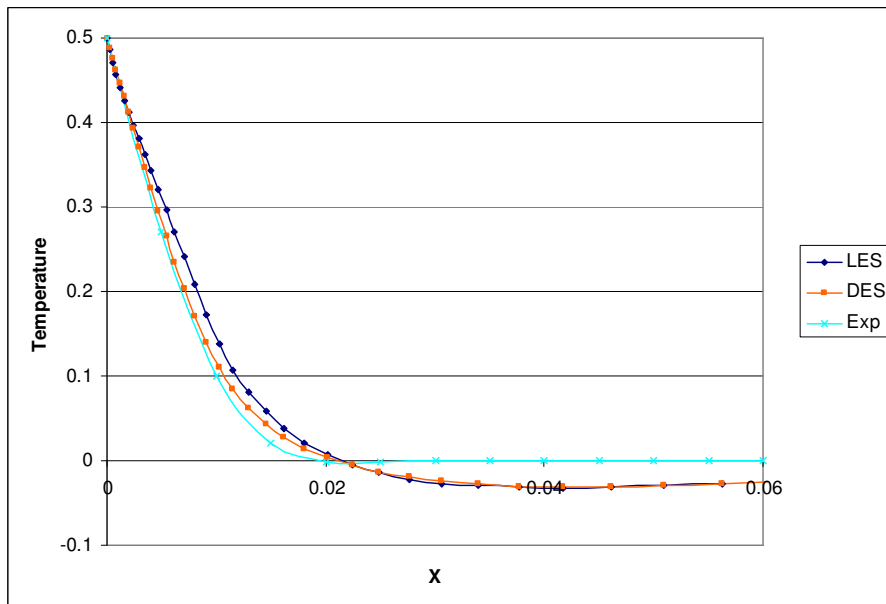


Figure 0-9 Temperature profile at mid-height in the median plane

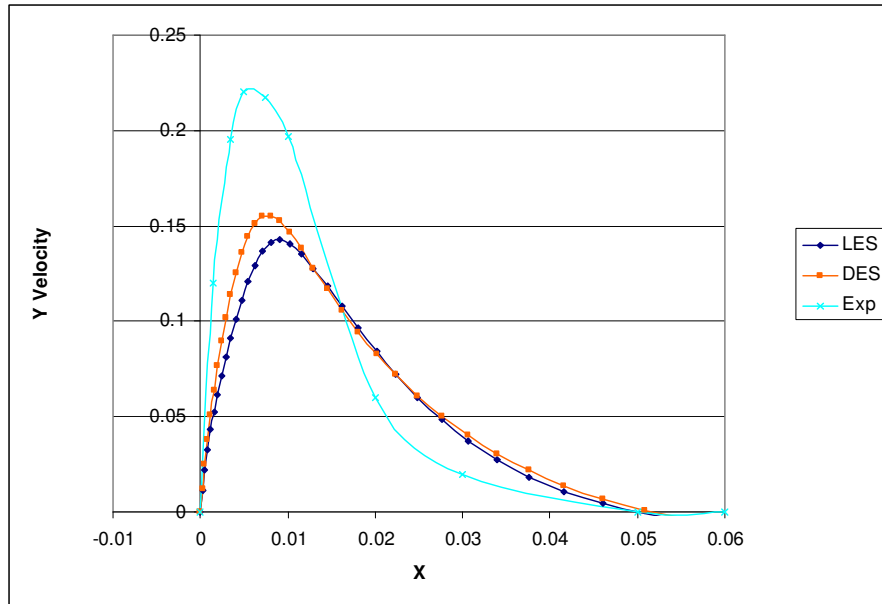


Figure 0-10 Velocity profile at mid-height in the median plane

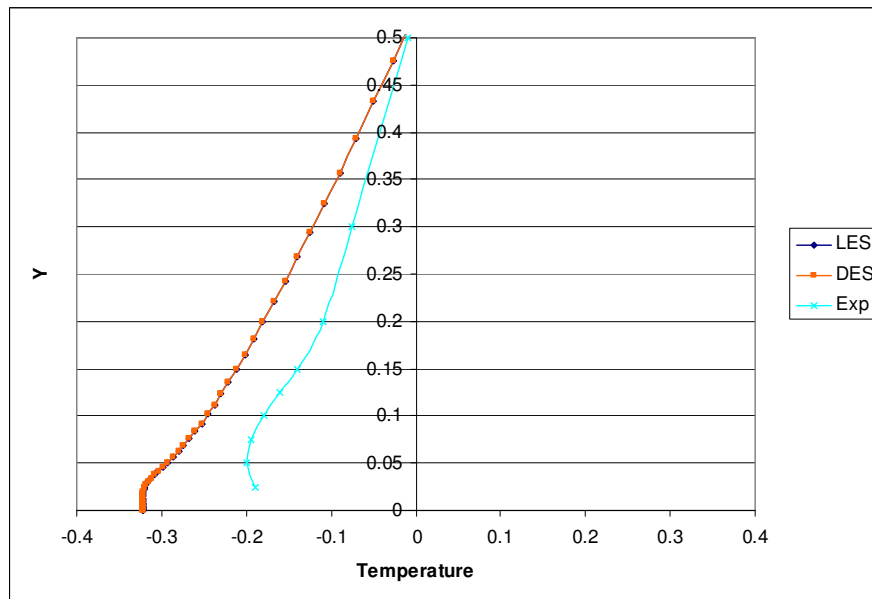


Figure 0-11 Temperature profile at mid-width in the median plane

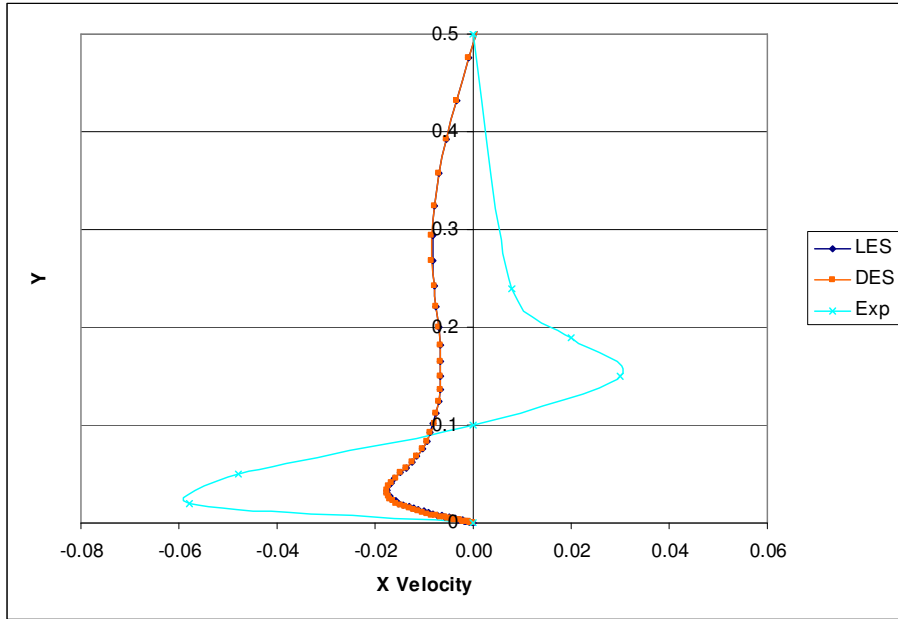


Figure 0-12 Velocity profile at mid-width in the median plane

Concordia Results

The following tables show the temperature and velocity profiles of the Concordia atrium for the purely natural convective case for four turbulent models.

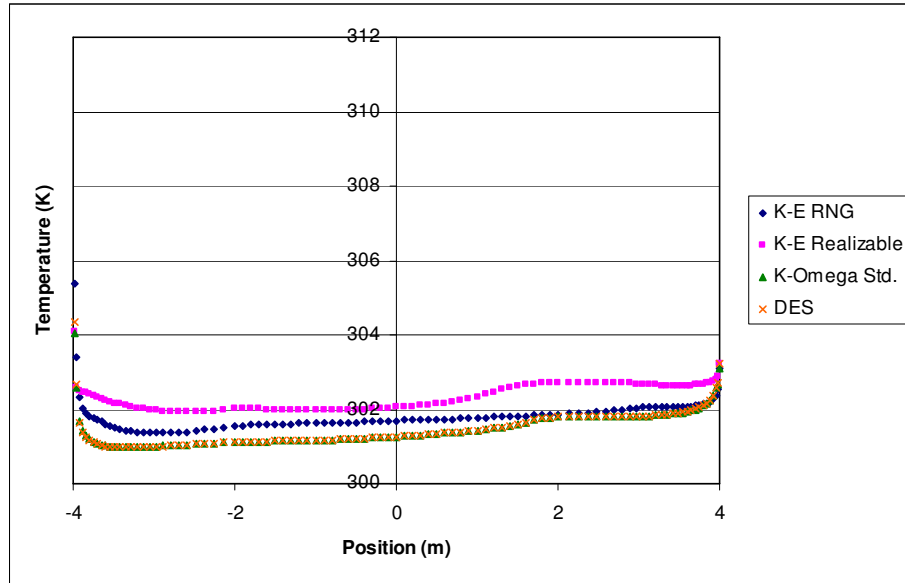


Figure 0-13 Vertical temperature profile of Concordia atrium for four turbulence models

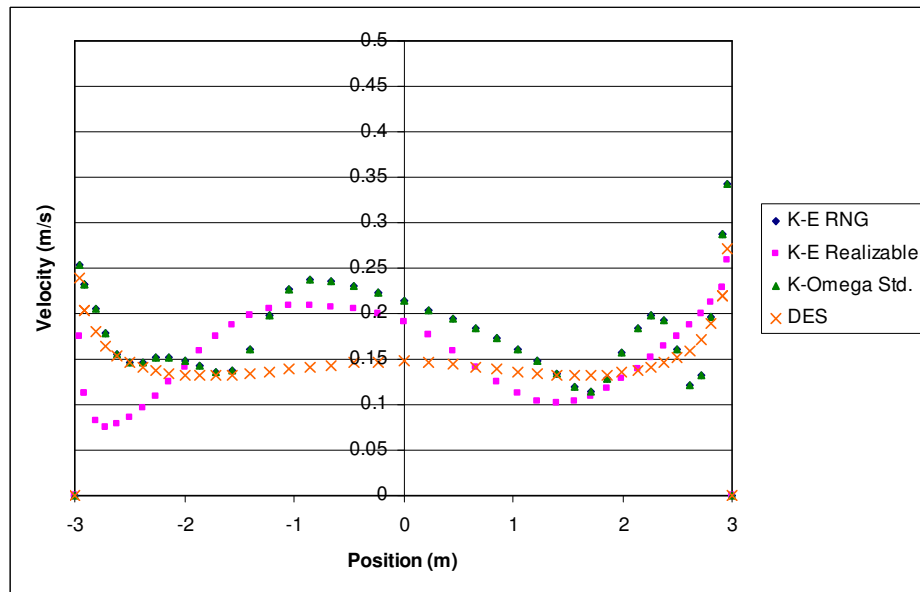


Figure 0-14 Horizontal velocity profile of Concordia atrium at height $y=1.2\text{m}$ for four turbulence models

Appendix B - Use of FLUENT in Present Study

Input values for FLUENT

This appendix contains the property values used for materials and surfaces in FLUENT. It should be noted that not all values were given in literature and therefore average values were assumed.

The flow in the domain is considered steady and the Boussinesq approximation is applied to the fluid (air) properties. The properties assigned to air listed in the table below are appropriate for air at a temperature of 25C and 1atm.

Table 0-1 Properties of Air

Density (kg/m^3)	1.18
Thermal Expansion Coefficient (K^{-1})	0.00335

Concordia Atrium

All walls except the glass wall in the Concordia-like atrium used the following values for radiation and thermal properties. Radiation properties were obtained from the following references; “Material Emissivity Properties” (www.electro-optical.com); ASHRAE Handbook Fundamentals; “Heliostat Design Concepts” (www.redrok.com).

Table 0-2 Thermal and radiative properties of walls

Density (kg/m^3)	10
Specific Heat (J/kg-K)	830
Thermal Conductivity (W/m-K)	0.1
Emissivity	0.9
Absorptivity	0.5

The glass wall on the south side of the Concordia-like atrium had the following thermal and radiation values. It was assumed to be double glazed glass.

Table 0-3 Thermal and radiative properties of glass wall

Density (kg/m ³)	2220
Specific Heat (j/kg-k)	830
Thermal Conductivity (W/m-k)	1.15
Emissivity	0.9
Absorptivity	0.5
Transmissivity	0.65

1m Cubic Cavity

Similar air properties were used for the cavity defined by Salat et al. as mentioned in the properties for the Concordia atrium. The values for the rest of the cavity can be seen in the following tables. Properties for Lexan[®] found on data sheet at “Professional Plastics” (www.professionalplastics.com) and properties for the polyurethane insulation were found at www.goodfellow.com.

Table 0-4 Thermal properties for outer glass walls

Density (kg/m ³)	2220
Specific Heat (j/kg-k)	830
Thermal Conductivity (W/m-k)	1.15

Table 0-5 Thermal properties for Lexan[®]

Density (kg/m ³)	1200
Specific Heat (j/kg-k)	1256
Thermal Conductivity (W/m-k)	0.2

Table 0-6 Thermal properties for walls (polyurethane)

Density (kg/m ³)	230
Specific Heat (j/kg-k)	1046
Thermal Conductivity (W/m-k)	0.03

Annex 26 Atrium

Air properties used for the other two models were again used for this model. The rest of the radiative and thermal property values used in this model can be seen in the following tables. Values for polystyrene were found at www.goodfellow.com.

Table 0-7 Thermal and radiative properties for glass walls

Density (kg/m ³)	2220
Specific Heat (j/kg-k)	830
Thermal Conductivity (W/m-k)	1.15
Emissivity	0.9
Absorptivity	0.5
Transmissivity	0.65

Table 0-8 Thermal and radiative properties for floor and north wall (polystyrene)

Density (kg/m ³)	1050
Specific Heat (j/kg-k)	1200
Thermal Conductivity (W/m-k)	0.1
Emissivity	0.5
Absorptivity	0.75